

Colloidal transport through inhomogeneous energy landscapes

Von der Universität Bayreuth
zur Erlangung des Grades eines
Doktors der Naturwissenschaften (Dr. rer. nat.)
genehmigte Abhandlung

von

Nico Christian Xaver Stuhlmüller

aus München

1. Gutachter: Prof. Dr. Daniel de las Heras
2. Gutachter: Prof. Dr. Enrique Velasco Caravaca, Universität Madrid

Tag der Einreichung: 27.10.2023

Tag des Kolloquiums: 19.12.2023

Colloidal transport through inhomogeneous energy landscapes

Von der Universität Bayreuth
zur Erlangung des Grades eines
Doktors der Naturwissenschaften (Dr. rer. nat.)
genehmigte Abhandlung

von

Nico Christian Xaver Stuhlmüller

aus München

1. Gutachter: Prof. Dr. Daniel de las Heras
2. Gutachter: Prof. Dr. Enrique Velasco Caravaca, Universität Madrid

Tag der Einreichung: 27.10.2023

Tag des Kolloquiums: 19.12.2023

Abstract

In this cumulative thesis we investigate with computer simulations the transport of colloidal microparticles through inhomogeneous energy landscapes. We mainly focus on magnetic colloids interacting with magnetic patterns, but we also consider transport in optical systems.

Inspired by the transport properties of electrons in twisted bilayer graphene, we study a particle-based classical system made of colloidal particles located between two-dimensional magnetic patterns that are rotated relative to each other. Flat channels in the magnetic potential develop due to the interference between the magnetic fields of both patterns. We show that there exist specific angles, the so called magic angles, at which these flat channels permeate the whole system. These percolated flat channels allow for macroscopic colloidal transport through the whole system when the colloidal particles are pushed by a drift force significantly weaker than the average magnetic force in the system. Flat channels also occur at angles different than the magic angles. However, these channels do not allow for macroscopic transport since they contain areas through which the colloidal particles can not pass when they are pushed by reasonable drift forces. We consider both square and hexagonal twisted magnetic patterns and characterize the effect of the temperature, the twist angle, and the driving strength on the colloidal transport.

Next we demonstrate that the phenomenology found in twisted magnetic patterns is robust under changes in the underlying physical system. To this end, we investigate colloidal particles in twisted arrays of optical tweezers. We show that at the same magic angles as in the magnetic system, the mobility of colloidal particles in the optical system massively increases.

Beyond drift transport, magnetic particles above single magnetic patterns can also be transported using topologically protected motion. A uniform external magnetic field drives the motion. The orientation of the field varies in time performing modulation loops. Loops that wind around specific orientations are able to transport the magnetic particles by one unit cell of the underlying magnetic pattern. We demonstrate here that topological transport is also possible in twisted magnetic patterns, and investigate the competition between drift and topological transport. The interplay between the two transport modes can both enhance and hinder the colloidal transport between the twisted patterns. Delicate commensuration effects involving the strength of the drift force and the period of the modulation loop, enable

macroscopic transport significantly faster than the pure topological transport. On the other hand, when the two transport modes oppose each other the transport of colloidal particles comes to a complete halt, even for strong drift forces.

Above periodic magnetic patterns, identical colloidal particles driven by modulation loops are always transported along the same direction. Particles that belong to different topological classes, such as e.g. paramagnetic and diamagnetic particles, can be simultaneously transported in different directions. However, all particles belonging to the same topological class perform the same motion everywhere above the periodic pattern. Here, we develop a class of inhomogeneous (non-periodic) patterns that enables a new type of topologically protected colloidal transport in which the transport direction depends on the absolute position above the pattern. We use both the local symmetry of the magnetic pattern and the modulation loop to encode the complexity of the transport. By doing so, we are able to control the transport of several identical colloidal particles simultaneously and independently. We also design an inhomogeneous pattern that features a particle trap. Several repetitions of a modulation loop move the colloidal particles toward the trap independently of their initial positions. Our computer simulation results are in excellent agreement with experiments.

Finally, we design a class of inhomogeneous magnetic patterns that possess a cloaked region. That is, a region in the pattern that is invisible to the asymptotic scattering of magnetic colloids performed with modulation loops. When particles move on a path towards the cloaked region, their trajectories are automatically deformed to move around the cloak. When the particles pass the cloaked region, their trajectories are the same as if the cloak was not there.

Kurzdarstellung

In dieser kumulativen Doktorarbeit wird der Transport von kolloidalen Teilchen durch inhomogene Energielandschaften untersucht. Der Fokus liegt auf magnetischen Kolloiden, die mit magnetischen Mustern interagieren. Zusätzlich wird auch der Transport kolloidaler Teilchen in optischen Systemen untersucht.

Inspiziert von den elektronischen Transporteigenschaften in zueinander verdrehten Graphendoppellagen, untersuchen wir die Transporteigenschaften von kolloidalen Teilchen in zueinander verdrehten magnetischen Mustern. Durch die Interferenz der Magnetfelder der zwei Muster entstehen flache Kanäle im magnetischen Potential. Wir zeigen, dass besondere, so genannte magische Winkel existieren, bei denen die flachen Kanäle das gesamte System durchziehen. Diese Kanäle erlauben makroskopischen, kolloidalen Transport durch das gesamte System, wenn die kolloidalen Teilchen mittels einer, im Vergleich zu den durchschnittlichen magnetischen Kräften, kleinen Kraft getrieben werden. Bei Winkeln, verschieden von den magischen Winkeln, existieren auch flache Kanäle. Diese erlauben jedoch keinen makroskopischen Transport, weil die Kanäle Abschnitte enthalten, die die kolloidalen Teilchen bei moderaten Driftkräften nicht passieren können. Wir untersuchen sowohl Muster mit quadratischer als auch hexagonaler Symmetrie.

Im Anschluss testen wir, ob die Phänomenologie, die in dem eben diskutierten magnetischen System auftritt, robust unter Änderung des physikalischen Systems ist. Hierzu analysieren wir den Transport von kolloidalen Teilchen in einem System von zueinander verdrehten optischen Pinzetten anstelle der verdrehten magnetischen Muster. Wir zeigen, dass auch in diesem System ein massiver Anstieg in der Mobilität der kolloidalen Teilchen zu messen ist, wenn der Drehwinkel zwischen den Pinzetten magisch ist.

Zusätzlich zu Drifttransport können kolloidale Teilchen auch mittels topologisch geschütztem Transport bewegt werden. Geschlossene Kurven (Loops) in der Orientierung eines räumlich homogenen externen Magnetfelds treiben die Bewegung. Wenn diese Loops bestimmte Orientierungen umkreisen, erzeugen sie topologisch geschützten Transport der kolloidalen Teilchen über dem zugrundeliegenden Muster. Wir zeigen, dass topologisch geschützter Transport auch zwischen verdrehten, magnetischen Mustern möglich ist. Des Weiteren untersuchen wir das Zusammenwirken des Drifttransports und des topologischen Transports. Durch das Zusammenwirken der zwei Transportmodi

kann die durchschnittliche Geschwindigkeit der Teilchen sowohl erhöht, als auch erniedrigt werden. Feine Abstimmung der Amplitude der Driftkraft und der Ausrichtung der Loops ermöglichen, dass der makroskopische Transport der kolloidalen Teilchen deutlich schneller als rein topologischer Transport wird. Andererseits können die Teilchen sogar bei starken Driftkräften zum kompletten Stopp gebracht werden, wenn die beiden Transportmodi entgegenwirken.

Über periodischen, magnetischen Mustern werden alle identischen Teilchen, die durch einen Modulationsloop getrieben werden, in die selbe Richtung bewegt. Teilchen, die unterschiedlichen topologischen Klassen angehören, beispielsweise paramagnetische und diamagnetische Teilchen, können simultan in verschiedene Richtungen transportiert werden. Alle Teilchen, die der selben topologischen Klasse angehören, werden jedoch in die selbe Richtung transportiert. Wir entwickeln eine neue Klasse von inhomogenen (nicht periodischen) Mustern, die einen neuen Typ von topologischem Transport ermöglichen, bei dem die Transportrichtung der kolloidalen Teilchen von ihrer absoluten Position über dem Muster abhängt. Wir benutzen sowohl die lokale Symmetrie der magnetischen Muster, als auch die Modulationsloops um die Komplexität des Transports zu kodieren. Diese Herangehensweise erlaubt es, eine Vielzahl von identischen Teilchen simultan und unabhängig voneinander zu kontrollieren. Außerdem konstruieren wir inhomogene Muster, die eine Teilchenfalle beinhalten. Die wiederholte Anwendung eines Modulationsloops bewegt kolloidale Teilchen in das Zentrum der Falle, unabhängig von der initialen Position der Teilchen. Unsere Computersimulationen stimmen exzellent mit Experimenten überein.

Schlussendlich entwerfen wir eine neue Klasse an inhomogenen, magnetischen Mustern mit einer Tarnregion, eine Region im Muster, die unsichtbar gegenüber asymptotischer Streuung von kolloidalen Teilchen durch topologische Loops ist. Wenn sich Teilchen auf die Tarnregion zubewegen, werden sie automatisch sanft um die Tarnregion herum geleitet, sodass ihre Trajektorien nach Passieren der Tarnregion so aussehen, als würde die Tarnregion nicht existieren.

Contents

1	Introduction	1
1.1	Colloidal transport	1
1.2	Topological transport of magnetic colloids above magnetic patterns	3
1.3	Simultaneous and independent transport of colloidal particles	9
1.4	Similarities to twisted graphene in the colloidal world	11
1.5	Cloaking	18
2	Publications	19
2.1	Overview of the publications	19
2.2	Author contributions	20
2.3	Enhanced colloidal transport in twisted magnetic patterns .	21
2.4	Colloidal transport in twisted lattices of optical tweezers . .	40
2.5	Competition between drift and topological transport of colloidal particles in twisted magnetic patterns	48
2.6	Simultaneous and independent topological control of identical microparticles in non-periodic energy landscapes	65
2.7	Summary and outlook	85
3	Topologically cloaked transport	87
3.1	Generating cloaked patterns	87
3.2	Simulation results	89
4	Methods	91
4.1	Integrating the equation of motion	91
4.2	Calculating the magnetic field from the pattern magnetization	92
	Bibliography	93

1 Introduction

1.1 Colloidal transport

Life requires the interplay between different length scales. Chemical reactions, that happen on length scales of ångströms, are required to keep a mammal, with length scale of a meter, alive [6]. These length scales need to be bridged such that the desired reactions occur at the right position in the body and at the right time [7, 8]. Proteins, which under certain circumstances behave like colloids [9], play a large role in controlling the chemistry of cells and larger living organisms [10]. Colloids are usually defined as insoluble particles in the length scale of nanometers to micrometers suspended in a solvent [11]. However, colloids can under some circumstances serve as a model for smaller systems like atoms and molecules [12–14] and also for larger ones such as granular systems [15].

As humans we have designed macroscopic machines that can control and build complex structures in the millimeter to meter range.¹ For example if you, the reader, are reading this thesis on a printed copy, the copy was produced by a printer which printed the letters with sub-millimeter accuracy on the paper. The paper itself was produced by machines. The wood required for the paper was probably harvested by machines and transported to the factory by truck or by train, which are again extremely complex machines. All of these machines make our current life possible. If I had to do all these tasks manually, I would not have had time to do the research presented in this thesis. This rather complex process was for an arguably simple paper copy. If you are reading this thesis on an electronic device, the machines allowing you to read the thesis are way more intricate. It is already in the name of the device, *electronic* device. Elemental particles, electrons in this

¹We have also developed much smaller machines like nanobots [16] and also much bigger machines like the accelerator ring of the LHC with a length of 27 km [17]. They however do not govern our everyday life.

case, are controlled on a nanometer scale in order for you to be able to read this text [18, 19]. However there are not many machines in our everyday life that control colloidal particles.

This thesis develops new ways to controlling colloidal particles by using inhomogeneous energy landscapes. This might be a starting point to build machines that operate reliably on colloidal particles. Such machines would be beneficial in e.g. curing diseases [20], reducing the amount of chemicals needed in the chemical analysis of samples [21–23], and in high precision measuring devices [24, 25].

In living organisms, colloidal particles are most often dissolved in aqueous solutions [26]. They can however also be dissolved in other fluids such as air (e.g. fog or smoke). Collisions with the constituents of the solvent generate a friction force on the colloidal particles and also cause them to undergo Brownian motion [27, 28]. As colloids play an important role in our lives, it is crucial to both understand their motion and to be able to control them precisely. In the theoretical description of colloids, the solvent is often not considered explicitly, but rather only implicitly via its effects on the colloidal particles [27]. However, when the solvent flow becomes important, e.g. when particles diffuse near an elastic membrane [29] the solvent and hydrodynamic interactions need to be considered explicitly. The equation of motion for the i -th colloidal particle in the case of an implicit solvent then reads

$$m\ddot{\mathbf{r}}_i = -\gamma\dot{\mathbf{r}}_i + \mathbf{f}_i + \boldsymbol{\eta}_i, \quad (1.1)$$

where m is the mass of the colloidal particle, \mathbf{r}_i is its position, the overdots denote temporal derivatives, γ is the friction coefficient against the implicit solvent, \mathbf{f}_i are all the deterministic forces (internal and external) acting on particle i , and $\boldsymbol{\eta}_i$ is a random force with vanishing mean and standard deviation given by the fluctuation dissipation theorem [27]. In the overdamped regime, the viscosity of the solvent is high. The inertial term can then be neglected, and equation (1.1) simplifies to

$$\gamma\dot{\mathbf{r}}_i = \mathbf{f}_i + \boldsymbol{\eta}_i. \quad (1.2)$$

The randomness of the Brownian forces can hinder the precise control of the particles. Strong forces on the other hand can limit the relative importance of Brownian motion. Individual particles, for example, can be controlled very precisely by optical tweezers [30, 31]. However this method does not scale easily to many particles, as one needs in principle one tweezer for each

particle. The collective motion of colloidal particles can be controlled for example by temperature gradients [32] and also by external fields such as a gravitational field [33, 34]. These collective effects can be used to realize an arbitrary flow of the particles with a given one body density [35, 36]. However, when doing so, then the control over the individual particles is lost. In this thesis we will use topologically protected motion and inhomogeneous energy landscapes to address these problems. This will allow us to simultaneously and independently transport identical particles in different directions using a single external field.

1.2 Topological transport of magnetic colloids above magnetic patterns

Topology, once a subject of pure math, has been found to have many applications in physics, ranging from quantum systems [37–39] over soft matter systems [40–42] to cosmological studies [43–45]. Topological protection means that some property of a system depends only on a topological invariant. Continuous deformations to the system do not change the invariant quantity and therefore the property behaves qualitatively the same as in the undisturbed system. When a change in the topological invariant is made (imagine plugging the hole of a torus) the system behaves in a significantly different manner.

As a thought experiment, we can imagine a chain. It is made of a given number of links. Topologically these are tori interlocked by Hopf links [46]. When one of the tori is deformed continuously the chain remains a chain. However, if one intermediate link of the chain is opened (a non-continuous deformation), the chain can no longer function as a chain. It is now two shorter chains.

Electrical circuits are another example where the topology is crucial for the proper functioning of a system. Imagine one of the simplest electrical circuits: an LED soldered to two wires that are connected to a power supply. When the power supply outputs the right voltage for the LED, it will light up, no matter the precise path of the wires. We can move the wires around, twist them and entangle them however we please, and the LED still lights up. But if we change the topology, by e.g. cutting a wire or connecting the LED to

the wrong poles of the power supply, it will no longer light up.

So we have seen that topology can fundamentally determine the behavior of a system. Where can topology be used in colloidal systems to precisely control their motion?

It has been recently shown that the motion of magnetic colloids above periodic magnetic patterns driven by an external magnetic field can be topologically protected [47–56]. A detailed explanation can be found in Ref. [54]. In this thesis we focus on similar systems and hence we explain in the following the general setup and terminology. The magnetic colloidal particles used in the experiments are widely used in biology, biochemistry [57–59] and also other experiments in physics such as, e.g. to study active systems, by spinning the colloidal particles [60–62].

The systems are comprised of magnetic patterns with regions of alternating magnetization normal to the plane of the pattern. The patterns are usually made of a periodic tiling of unit cells. As each of the unit cells are identical, the pattern can be described by only one unit cell and the rule on how to connect it to itself in order to recover the whole pattern. A simple yet interesting case is a checkerboard pattern [56], see figure 1.1 (a) for a sketch of the system. Opposite edges of the unit cell can be connected, which causes the topological properties of the pattern to be those of a torus. At a distance of roughly one unit cell above the patterns, paramagnetic colloidal particles are submersed in water and are forced to move in a 2D-plane, the *action space* \mathcal{A} , which can also be folded back to a torus. The colloidal particles have a magnetic susceptibility χ . An external magnetic field $\mathbf{H}_{\text{ext}}(t)$ homogeneous in space but varying in time t , with amplitude much stronger than that of the magnetic field of the pattern \mathbf{H}_{p} is used to control the motion of the particles. The possible set of all orientations of \mathbf{H}_{ext} is called *control space* \mathcal{C} . As the set of all possible orientations of a 3D-vector, in this case \mathbf{H}_{ext} , is the surface of a sphere, \mathcal{C} is also the surface of a sphere. In the following, closed loops in \mathcal{C} will be used to move particles. This can be done since there exist closed loops in \mathcal{C} such that when the orientation of \mathbf{H}_{ext} returns to its initial one, the particles have moved one unit-cell in \mathcal{A} .

The external magnetic field and the magnetic field of the pattern induce a magnetic moment \mathbf{m} parallel to the combined magnetic field, in the colloidal particles. The magnetic energy of a particle at position \mathbf{r}_i and time t is then given by minus the product of its magnetic moment times the magnetic field that it experiences, i.e. $-\mathbf{m}(\mathbf{r}_i, t) \cdot (\mathbf{H}_{\text{p}}(\mathbf{r}_i) + \mathbf{H}_{\text{ext}}(t)) \propto -(\mathbf{H}_{\text{p}}(\mathbf{r}_i) + \mathbf{H}_{\text{ext}}(t))^2$.

As only non constant terms in this expression lead to forces on the particle, we can omit the contribution proportional to $\mathbf{H}_{\text{ext}}^2$. The term proportional to \mathbf{H}_p^2 can be neglected compared to the cross-term $\mathbf{H}_p \cdot \mathbf{H}_{\text{ext}}$, since $\mathbf{H}_p^2 \ll |\mathbf{H}_p \cdot \mathbf{H}_{\text{ext}}|$, as $|\mathbf{H}_p| \ll |\mathbf{H}_{\text{ext}}|$. Hence the relevant part of the magnetic potential to understand the colloidal motion is the cross-term

$$V_{\text{ext}}(\mathbf{r}_i, t) \propto -2\mathbf{H}_p(\mathbf{r}_i) \cdot \mathbf{H}_{\text{ext}}(t). \quad (1.3)$$

When \mathbf{H}_{ext} is varied on timescales significantly slower than the relaxation time of the colloidal particles into a minimum of V_{ext} , the transport is adiabatic, in the sense that particles will follow the minima in V_{ext} (provided that a minimum exists). We will stay in this regime and therefore it is sufficient to discuss the extrema of V_{ext} to understand the transport. There are regions $\mathcal{A}^a \subset \mathcal{A}$, so called *allowed regions*, which are defined as the set of all points $\mathbf{r} \in \mathcal{A}$ for which there exists an orientation in \mathcal{C} such that $V_{\text{ext}}(\mathbf{r})$ attains a minimum [54], see figure 1.1 (b) for a visualization. There exist also regions $\mathcal{A}^f \subset \mathcal{A}$, the *forbidden regions*, which are the set of points $\mathbf{r} \in \mathcal{A}$ for which there exists no orientation in \mathcal{C} for which $V_{\text{ext}}(\mathbf{r})$ is a minimum, but a saddle point [54].² The allowed and forbidden regions are separated by the so called *fences*, see figure 1.1 (b) for a visualization. The points where two fences meet are called the *gates*. A visualization of the allowed and the forbidden regions, the fences, the gates and illustrative particle trajectories is shown in figure 1.1(a-d) for a square pattern. In a square pattern there exist two distinct regions of \mathcal{A}^a per unit cell. One in the center of the unit cell, and the other connects adjacent unit cells together. These different allowed regions are connected by four gates, see figure 1.1 (b). If driven by a modulation loop a particle crosses the same gate twice, it remains in its original unit cell. If the particle however crosses two different gates, it is transported to a different unit cell. Now the question “how can we control which gates do the particles cross?” arises. To answer it, we can try to map points in \mathcal{A} to points in \mathcal{C} by finding the points in \mathcal{C} that make the points in \mathcal{A} stationary. However, this mapping is not bijective. One can construct a manifold by building the direct product $\mathcal{A} \otimes \mathcal{C}$. When one restricts this product to all the stationary points, i.e. those where $\nabla V_{\text{ext}} = 0$, one attains the so called *stationary manifold* \mathcal{M} [56]. This manifold contains all information about the adiabatic transport of our system [54]. Points in \mathcal{M} can then be projected to

²The reader might wonder why we did only talk about minima and saddle points in V_{ext} , and have seemingly omitted the discussion of maxima. Note that via the transformation from \mathbf{H}_{ext} to $-\mathbf{H}_{\text{ext}}$ a maximum is converted to a minimum. Hence, the maxima are included in the discussion of \mathcal{A}^a .

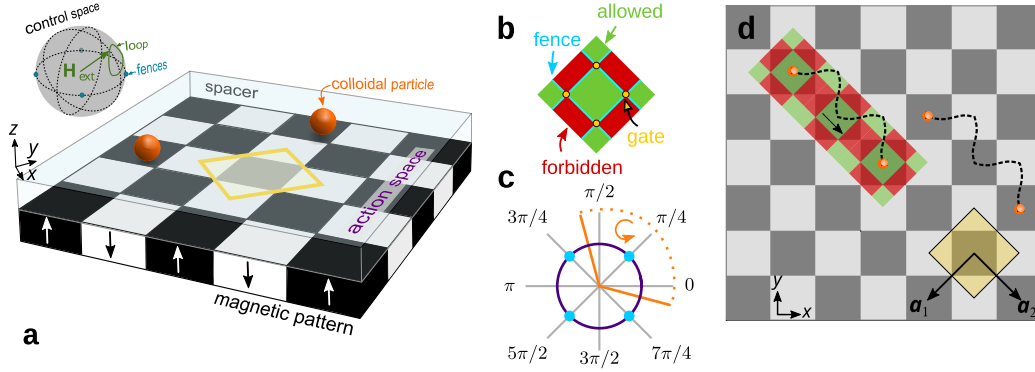


Figure 1.1: Schematic overview of the transport above periodic square patterns. (a) 3D view the setup. (b) allowed and forbidden regions. (c) stereographic projection of control space together with a modulation loop (orange) that transports particles along the trajectories shown in (d). The purple line depicts the equator of \mathcal{C} . The blue points (lines) are the fences in \mathcal{C} (\mathcal{A}), the orange arrow indicates the sense of circulation and the orange dots mean that the loop is closed on the south pole. (d) top view of (a). The dashed black lines are particle trajectories after two loops. The yellow square in (a) and (d) depicts a unit-cell. Adapted from publication 4, originally licensed under the CC BY 4 license [65].

\mathcal{A} and \mathcal{C} . This projection is shown in figure 1.2 (a-c), including all fences and gates. The fences of the square pattern are four equidistant points along the equator of \mathcal{C} , see figure 1.2 (a), which are connected by the gates. This means that we can perform a closed loop with \mathbf{H}_{ext} in \mathcal{C} that crosses two different gates. As a consequence, the loop moves particles from one unit cell to an adjacent one. As different gates in \mathcal{C} are separated by the fence points, the set of winding numbers of the path of \mathbf{H}_{ext} in \mathcal{C} around the fences (and only it) determines which direction and how many unit cells the particles travel. The exact trajectory of the particle in action space depends on the details of the path in \mathcal{C} , but not the unit cell in which the particle will reside after the loop. The set of winding numbers around the fences is a topological invariant. Therefore the transport of the colloidal particles is topologically protected. One can concatenate loops that transport particles in different directions by topologically trivial paths in \mathcal{C} , which allows the colloidal particles to be transported to any desired location above the pattern.

While explaining the topological nature of the transport of colloidal particles, we have used the symmetry of the square pattern numerously. So one is naturally curious about what happens when the square pattern is replaced by a pattern of a different symmetry class, e.g. C_6 or S_6 (Schoenflies notation [64]). Figure 1.3 (a-d) shows the effects of changing the symmetry of the underlying

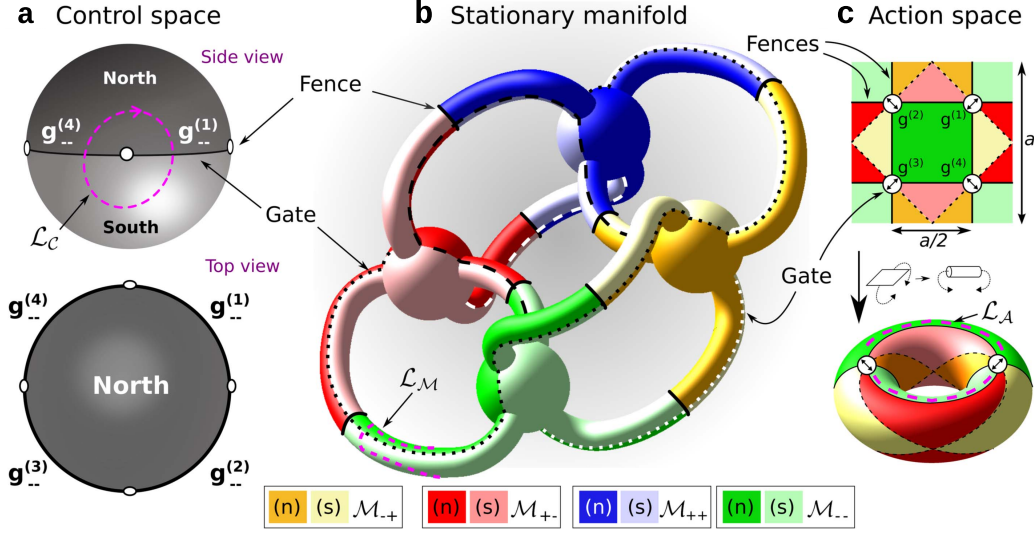


Figure 1.2: Projection of the stationary manifold \mathcal{M} (b) on to \mathcal{A} (c) and \mathcal{C} (a) for a pattern with square symmetry. A loop (\mathcal{L}) is represented by a purple dashed line in (a-c) as $\mathcal{L}_{\mathcal{C}}$ in \mathcal{C} , $\mathcal{L}_{\mathcal{M}}$ in \mathcal{M} and as $\mathcal{L}_{\mathcal{A}}$ in \mathcal{A} . Red and yellow colors represent forbidden regions, blue and green colors represent allowed regions in \mathcal{A} and \mathcal{M} . Gates are labeled by $g^{(x)}$, $x \in 1, 2, 3, 4$ and depicted as solid lines in (a), as dashed lines in (b) and as circles with arrows in (c). Fences are shown as white circles in (a) and as solid lines in (b) and (c). The labels (n), (s) indicate whether the orientation of the external magnetic field points to the north or to the south of \mathcal{C} . Adapted from [56], originally licensed under the CC BY 3 license [63].

pattern. In patterns with C_6 and S_6 symmetry the fences in \mathcal{C} are no longer points but one dimensional curves that meet in the so called *bifurcation points* [55], see figure 1.3 (a,b). In patterns with C_6 and S_6 symmetry, the set of winding numbers around the bifurcation points determines the direction of transport [54]. As the possible directions of transport are given by the symmetry of the patterns, the particles can get transported in different directions above patterns with different symmetry classes, see figure 1.3 (c,d) for illustrative trajectories. Above a pattern with C_6 or S_6 symmetry for example, the particles can get transported along any of the three symmetry directions of the pattern (in positive and negative direction), allowing for six directions separated by 60° . However, a loop in \mathcal{C} that transports particles above a pattern with C_6 symmetry in one direction does not necessarily transport particles above a pattern with S_6 symmetry in the same direction, since the fences/bifurcation points are in different locations. We will use this in the next section to achieve locally different transport directions above spatially inhomogeneous patterns.

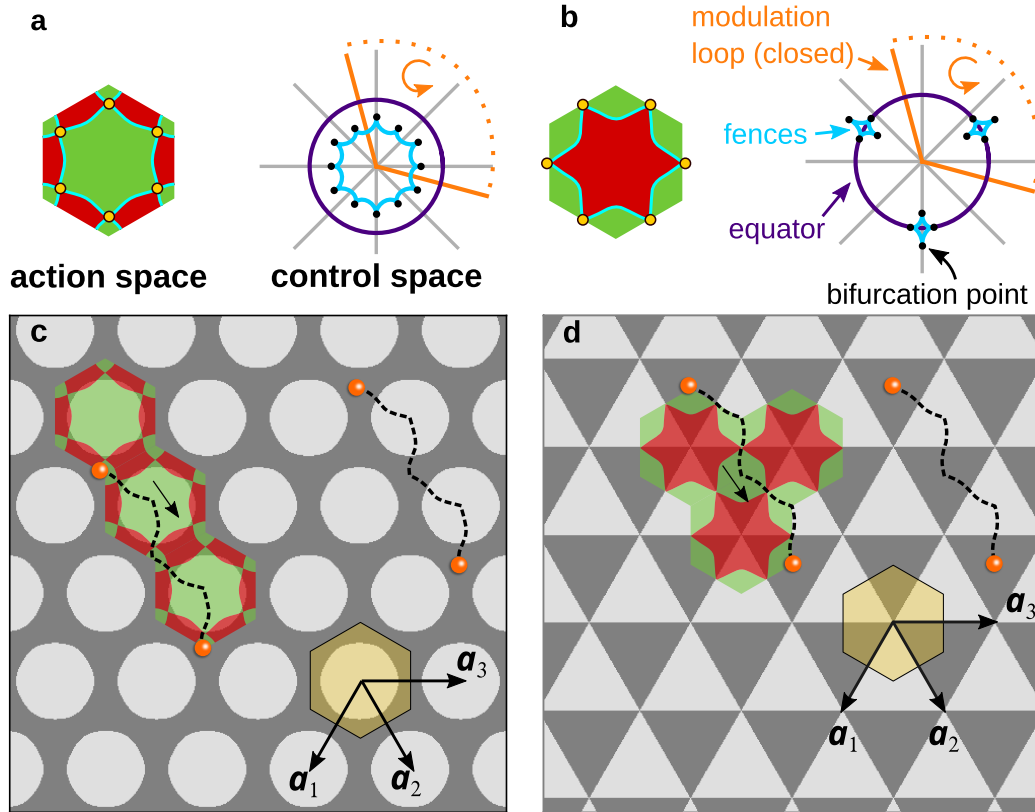


Figure 1.3: Overview of the transport above hexagonal patterns for the case of C_6 symmetry (a,c) and S_6 symmetry (b,d). (a) and (b) depict the unit cell of action space with the allowed (forbidden) regions in green (red) and the fences (gates) in blue (yellow). Control space in (a) and (b) is shown in the stereographic projection of \mathcal{C} . The purple lines depict the equator, blue lines represent the fences and black dots show the bifurcation points. The orange line shows an illustrative modulation loop of the external magnetic field. Orange dots indicate, that the loop is closed on the south pole, which can not be shown in the stereographic projection. (c) and (d) show the magnetic pattern in dark and light gray for regions of positive and negative magnetization normal to the pattern respectively. The unit cells of the patterns are highlighted in yellow. Black arrows depict the lattice vectors \mathbf{a}_i , $i \in 1, 2, 3$ of both patterns. Illustrative trajectories of colloidal particles (orange spheres), driven by the loops shown in (a) and (b) are indicated by dashed black lines. The direction of transport is indicated by a small black arrow. Adapted from publication 4, originally licensed under the CC BY 4 license [65].

1.3 Simultaneous and independent transport of colloidal particles

In the previous section we have seen that one can control particles precisely, but there are limitations. One limitation that arises above periodic patterns is that all identical particles above the pattern are transported in the same direction, independently of their absolute position above the pattern. There is no option to let the transport of particles be dependent on their absolute position above the pattern. It would be great to be able to do so in order to build colloidal machines that can parallelize workloads.

Previous works have used non-identical particles. Visualizations of these works are shown in figure 1.4 (a-c): Above hexagonal patterns, para- and diamagnets can be controlled independently of each other [55], see figure 1.4 (a). Mirzaee-Kakhki et al. [49] showed that bipeds (colloidal rods of variable length) can belong to different topological classes. Hence, they can be moved in different directions above periodic patterns subject to the influence of the same loop in control space, see figure 1.4 (c). The reason these two approaches work is that particles in different topological classes have different fences in control space. Therefore one can move one class of particles without moving the other. Which then in turn allows one to construct loops that individually control each class of particles. Another option is to use identical particles, such as octupoles comprised of two para- and two diamagnets, and place them in non-equivalent minima above a periodic pattern which allows them to be transported in different directions subjected to the influence of the same external control loop [47], see figure 1.4 (b).

Bipeds need a different length to be transported in different directions but still all bipeds of the same length perform the same trajectory above the pattern. This can be an inconvenience. It would be useful, if one could use identical particles and have them be transported in different directions depending on their absolute position above the pattern. We show in this thesis that by using inhomogeneous patterns we can make identical particles behave differently in different parts of the pattern. We summarize two fundamentally different approaches to the locally different transport in publication 4.

A simple approach is to combine pure patterns with different global rotations. As a starting point, imagine three square patterns rotated such that their respective unit cells are rotated by 0° , 15° and 30° around a reference axis

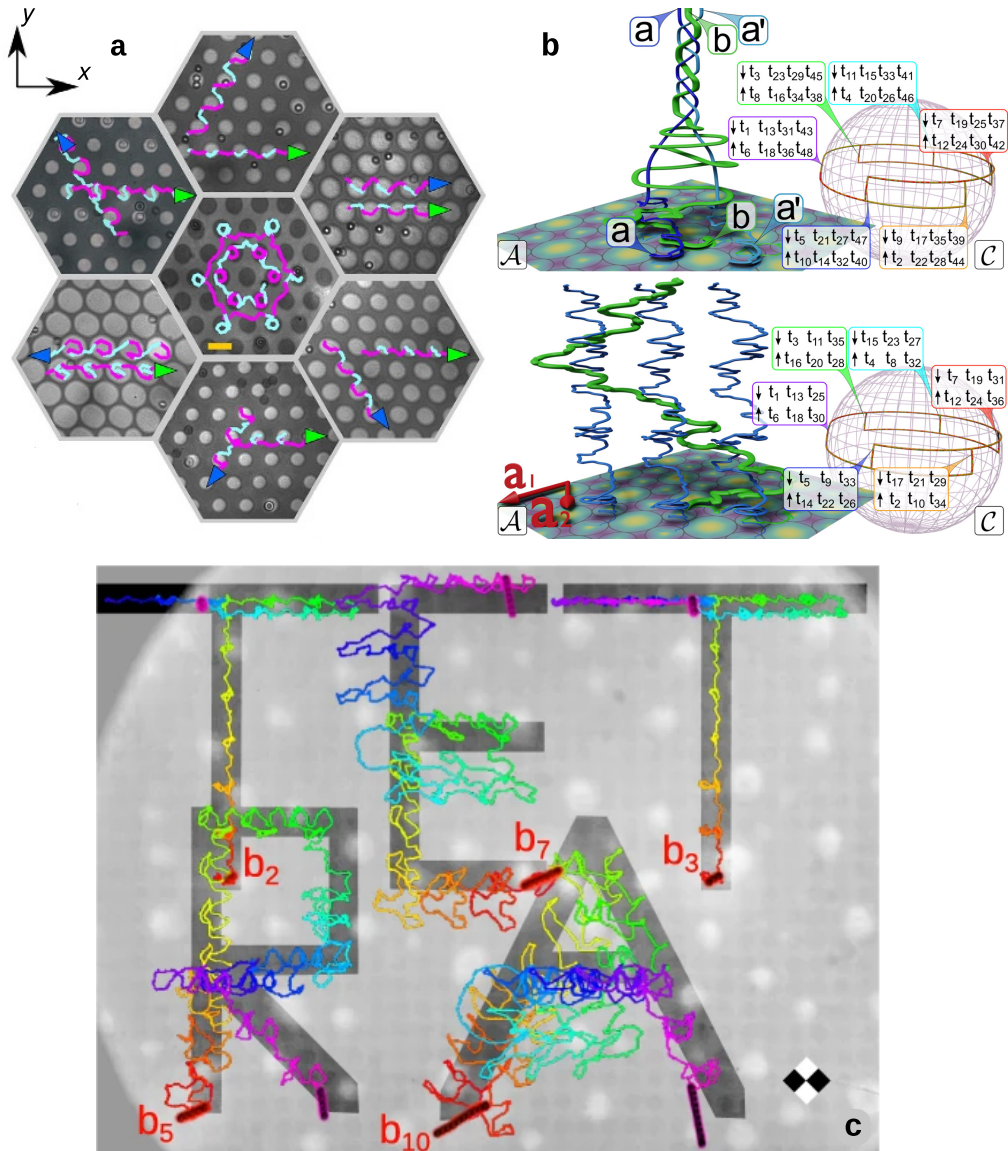


Figure 1.4: Overview of publications where particles perform different tasks when subject to the influence of the same control loop. (a) simultaneous and independent transport of para- and diamagnets (indicated by blue and green arrow respectively) above hexagonal patterns. Diamagnets always move to the right, while the transport direction of the paramagnets is chosen to be one of the six possible directions in hexagonal patterns. In the center panel the motion subject to the influence of a more intricate loop is shown. Here the two particles perform a Franconian dance. Adapted from [55]. (b) braiding (top) and weaving (bottom) with octupoles, action space on the left, control space to the right. Adapted from [47]. (c) simultaneous and independent transport of colloidal bipeds of different lengths. Bipeds of length 2 (b_2) and of length 3 (b_3) are in the same topological class, so they write the same letter “T”. Bipeds of length 5 (b_5), 7 (b_7) and of length 10 (b_{10}) are in different topology classes, therefore they are used to write different letters “R,E,A”, respectively. Adapted from [49]. The images in the panels are originally licensed under the CC BY 4 license [65].

normal to the pattern, respectively. Recall from section 1.2 that the fences of the square pattern are four equidistant points on the equator in \mathcal{C} . By rotating the patterns, the corresponding fences are also rotated, and therefore not overlapping. This allows us to e.g. wind around the fences of one pattern, but not around the fences of the other patterns. We can now combine the three patterns by placing them next to each other without overlap. The reason these modes of transportation still work on the combined patterns is that locally the combined pattern is similar to the periodic patterns. The fence points that determine the local transport are only given by the local symmetry properties of the pattern. Which allows for independent transport of the particles above the three sublattices.

A second way of achieving locally different transport is to continuously morph a pattern through the family of hexagonal patterns. Hexagonal patterns can be constructed by the interference of three waves with q -vectors that are rotated 120° relative to each other. All three of the q -vectors can carry a phase $\phi_i, i \in \{1, 2, 3\}$. The three phases can be combined into a local shift of the unit cell, and a symmetry phase ϕ . When the symmetry phase is changed continuously the aforementioned transformation of patterns through the different symmetry classes occurs. By doing this, the fences in \mathcal{C} also move continuously. One can for example deform a C_6 -pattern into a S_6 -pattern, from there into an inverted C_6 -pattern ($\overline{C_6}$), from there into an inverted S_6 -pattern ($\overline{S_6}$), and back into the original C_6 -pattern. A visualization of such a continuously deformed pattern together with the corresponding fences is shown in figure 1.5 (a,b).

Another class of inhomogeneous energy landscapes can be constructed by the interference of two periodic patterns. We see an example in the following section in which we investigate twisted patterns.

1.4 Similarities to twisted graphene in the colloidal world

Graphene is a monoatomic layer of Graphite [66]. It can be produced with a pencil and some scotch tape [67]. As a 2D material with fascinating properties that can be produced without special equipment it sparked a new area of research [68–76]. Its electronic structure has surprising attributes: Electrons

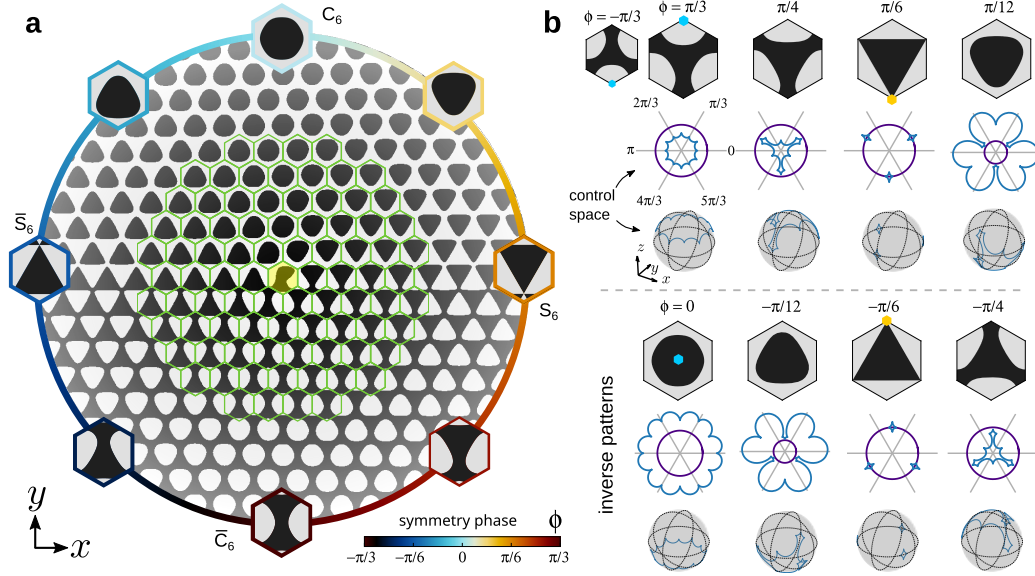


Figure 1.5: (a) magnetic pattern that continuously deforms from C_6 , to S_6 , to \bar{C}_6 , to \bar{S}_6 and back to C_6 , with changing polar angle. The local symmetry phase of the pattern is illustrated by the colored perimeter. The green hexagonal mesh shows the boundaries of units cells of a pure hexagonal pattern. At the origin a topological defect in the symmetry phase ϕ occurs (highlighted in yellow). (b) unit cells and corresponding control spaces at representative values of the symmetry phase are shown in a 3D visualization and a stereographic projection. Blue lines depict the fences, purple lines correspond to the equator. Blue (yellow) hexagons indicate C_6 (S_6) symmetry points in the unit cells. Adapted from publication 4, originally licensed under the CC BY 4 license [65].

move through graphene with vanishing rest mass and are therefore described by Dirac's equation [76]. Another interesting property of the electronic structure of graphene is that electrons in it can travel micrometers in distance without scattering even at room temperature [76]. This can be pushed even further by stacking two sheets of graphene on top of each other, and twisting them to the so called *magic angle* of $\approx 1.05^\circ$, where superconductivity can occur [68]. This sparked the idea in us to see whether we can find interesting transport properties of colloidal particles in twisted magnetic patterns. We were further motivated by other classical systems that exhibit phenomenology similar to twisted graphene such as acoustic metamaterials [77] and vortex pinning [78].

1.4.1 Twisted bilayer graphene

Twisting two hexagonal lattices with respect to each other causes a Morié pattern to appear. The Morié pattern consists of structures that are substantially bigger than the unit cells of the underlying patterns. We call these structures *supercells*. These large scale structures also develop when two stacked sheets of graphene are twisted relative to each other. In this process, the electric potentials combine and can be described by a superlattice. As the lattice becomes large in real space, the Brillouin zone in Fourier space becomes small, the so called mini Brillouin zone. The electronic bands in it become flat at the magic angle. At this angle and half filling of the bands, twisted graphene is a strongly correlated insulator [73]. When electrostatically doped to approximately two electrons per unit cell, a superconducting phase appears that cannot be explained with phonon-electron coupling [73]. This phenomenon is due to the flat bands and therefore can only occur at the magic angle.

1.4.2 Twisted magnetic patterns

In a classical system we can obviously not find any superconducting states, but we can still test whether there are magic angles at which the system changes from a colloidal insulator to a colloidal conductor. As an analogy to twisted graphene, we vertically combine and twist two identical periodic patterns. In contrast to twisted graphene we cannot stack the patterns directly on top of each other, as we need the particles to be able to travel between the patterns. Therefore we separate them by a distance Δ . We choose the magnitude of Δ to be in the order of the size of a lattice vector of the individual patterns. Here, the exact details of the underlying patterns become less important and only their symmetry properties remain [54]. Regarding the pattern symmetries we choose pure hexagonal and square patterns. We want to understand how the magnetic potential of these twisted systems changes with the twist angle. Morié patterns are in general not periodic, even when the underlying patterns are. However, there exist specific angles at which the combined lattice attains a periodicity again:

$$\alpha_{\text{per}}(q/p, n) = 2 \arctan \left(\frac{q/p \sin(\pi/n)}{1 + q/p \cos(\pi/n)} \right), \quad (1.4)$$

where q and p are co-prime integers that carry information about the period of the pattern and $n = 2$ (3) for square (hexagonal) patterns [1]. When

$q = 1$ and $p = nk + 1$, with $k \in \mathbb{N}$, the Morié pattern has a periodicity of exactly one (two) supercell(s) for underlying hexagonal (square) patterns [1]. The difference between periodic structures and supercells in square patterns is visualized in figure 1.6 (a-d). In the aforementioned cases ($q = 1$ and $p = nk + 1$) the formulae for the periodic angles simplifies to

$$\alpha_m^{\text{sq}}(k) = 2 \arcsin \left(\frac{1}{2\sqrt{k^2 + k + 1/2}} \right), \quad (1.5)$$

$$\alpha_m^{\text{hex}}(k) = \arccos \left(\frac{3(2k + 1)^2 - 1}{3(2k + 1)^2 + 1} \right), \quad (1.6)$$

for the square α_m^{sq} and the hexagonal α_m^{hex} systems respectively. For reasons that will become clear later, these angles are called *magic angles*. Notice that the magic angle of twisted graphene is contained in these magic angles, $\alpha_m^{\text{hex}}(31) \approx 1.05^\circ$. At the boundaries of the supercells some of the wave vectors that generate the magnetic potential destructively interfere, which causes *flat channels* to appear [1]. Note that the flat channels in the colloidal system are located in real space, while the flat bands in graphene are in momentum space. Performing loops in \mathcal{C} will periodically alter these channels. As the system is complex enough on its own, we start by investigating a system with fixed orientation of \mathbf{H}_{ext} . Later we will allow for loops of the orientation of the external magnetic field. Here we set \mathbf{H}_{ext} to point north all the time, i.e. normal to the pattern. This simplifies the magnetic potential to a sum of cosines [1]:

$$V_{\text{mag}}(\mathbf{r}) \propto \sum_{i=1}^n [\cos(\mathbf{q}_i \cdot (\mathbf{r} - \mathbf{a}_1/2)) + \cos(\mathbf{R}_\alpha \mathbf{q}_i \cdot \mathbf{r})], \quad (1.7)$$

where \mathbf{q}_i are the reciprocal lattice vectors (n in total, where $n = 2$ in square patterns and $n = 3$ in hexagonal patterns) of the untwisted system, \mathbf{a}_1 is the first lattice vector and \mathbf{R}_α is a rotation matrix that rotates by α around an axis going through the origin and being normal to the pattern.

In order to test whether the flat channels support the macroscopic transport of colloidal particles or not, we apply a drift force to the particles. In an electrical conductor one would apply a voltage to the sample and measure the current through the system to test its resistance/conductance. As our colloidal particles do not have an electrostatic charge, we can not simply apply a voltage. Instead, we apply a constant drift force that points along the

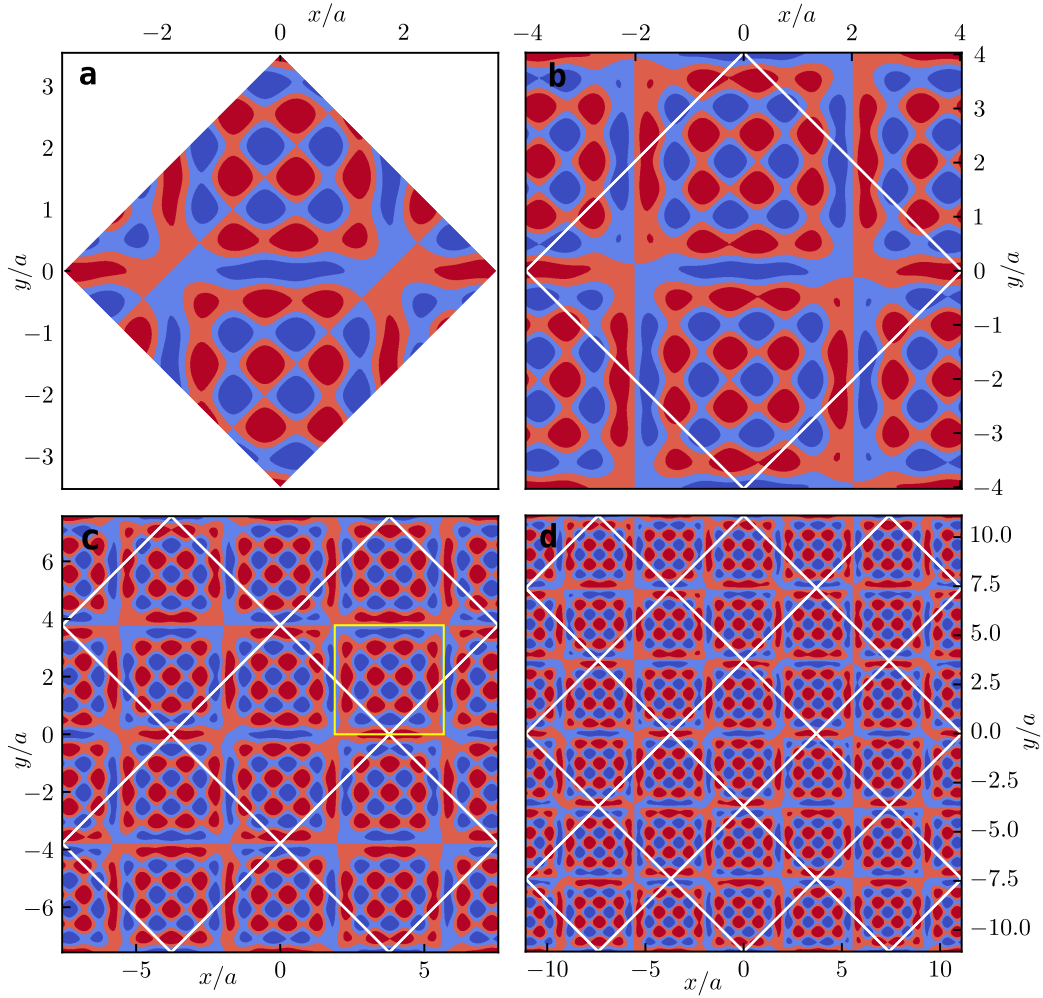


Figure 1.6: Magnetic potential generated by two twisted square patterns for twist angles at which the resulting Moré pattern is periodic. Blue (red) regions indicate negative (positive) magnetic potential. White lines in (b-d) highlight pseudo unit cells of the Moré pattern, where each region of the potential in a white square is slightly different. The colored area is the actual periodic unit cell of the Moré pattern. Yellow lines in (c) highlight a supercell. (a) magic case for $\alpha_{\text{per}}(1/7, 2) = \alpha_m^{sq}(3) \approx 16.26^\circ$. (b) $\alpha_{\text{per}}(1/7, 2) \approx 14.25^\circ$ periodic cell contains 4 supercells. (c) $\alpha_{\text{per}}(2/15, 2) \approx 15.19^\circ$ periodic cell contains 16 supercells. (d) $\alpha_{\text{per}}(3/22, 2) \approx 15.53^\circ$ periodic cell contains 64 supercells. Adapted from publication 1, originally licensed under the CC BY 4 license [65].

direction of the flat channels and then measure the mobility of the particles.³ In an experimental realization of the system the drift force might be facilitated through e.g. gravity or a pressure gradient in the solvent which would cause a solvent flow. In publication 1 we show that the system becomes a colloidal conductor for forces above a critical force at exactly these specific angles and it is a very good insulator otherwise. Therefore we call the angles at which the system allows for macroscopic colloidal transport *magic angles*.

Are these properties unique to our magnetic system, or do they hold more generally when two lattices are combined? To show that the latter is actually the case, we investigate a twisted array of optical tweezers.

1.4.3 Twisted optical tweezers

Optical tweezers are used widely in many biological, biochemical and biophysical research projects [79]. They are often used as a means to precisely manipulate particles and to measure forces in the piconewton regime [79]. An array of tweezers can be used to sort particles of different sizes [80, 81]. The force exerted on a particle by an optical tweezer depends on the diameter of the particle. Therefore one can build a machine that sorts particles of different sizes [80]. Here, we extend the idea of using an array of optical tweezers to sort particles, in order to show that a colloidal particle between two twisted arrays of tweezers inherits similar properties to that of a magnetic colloidal particle between two twisted magnetic patterns. The particles in the twisted array of optical tweezers are subject to a substantially different potential than the magnetic colloids from last section. The potential is given by [80]

$$V(\mathbf{r}) = \frac{-V_0}{1 + e^{-A[g(\mathbf{r})-1]}}, \quad (1.8)$$

where the constant A controls the steepness of the potential, V_0 controls the amplitude, and $g(r)$ is given by the same sum of cosines as in the magnetic potential in equation (1.7). The physical phenomenology of high mobility of colloidal particles in arrays twisted to a magic angle, and low mobility otherwise remains, even though the system is different. This suggests that the aforementioned phenomenology is not just a special case of magnetic colloidal particles, but can happen in a wider range of physical systems. Additionally

³We could also measure the mobility of the particles under the influence of loops of the external field. This method is used in publication 3 and explained in section 1.4.4.

by exemplifying this robustness with respect to the concrete physical system, we open the possibility of studying analogous systems to a wider community, as using optical tweezers is in principle simpler than producing magnetic microfilms.

1.4.4 Competition between topological and drift transport

We have previously hinted that when using twisted magnetic patterns one can also perform loops of the orientation of the external magnetic field. An interesting observation is that even without a drift force (i.e. the particles are solely driven by loops of the orientation of \mathbf{H}_{ext}) the particles are drawn towards the flat channels [3]. This effect can be used to increase the number of particles in the flat channels. If one only uses a drift force, i.e. no external loops, then only the particles that are initialized in the proximity of a flat channel will be mobile. All the other particles inside the supercells will remain stuck (at reasonable drift forces). With external loops however one can set the drift force to a subcritical value and still achieve macroscopic transport. At subcritical drift forces the particles can not travel through the flat channels completely, since they get stuck at the corners. Here, the topological loops can be used to transport particles around the corner and towards the flat channels. Additionally, particles in the inner regions of the supercells get transported to the flat channels by the loops in the orientation of \mathbf{H}_{ext} . Hence, after approximately L/a loops all particles are in the flat channels. Here, L is the period of the Morié pattern and a is the period of the underlying patterns. The interplay between topological loops and the drift force produces several interesting effects including

- subharmonic responses of the average velocity to the driving loop at sub- and supercritical drift forces
- average velocities of up to one supercell per loop at subcritical drift force
- vanishing mobility at sub- and even supercritical drift forces
- integer steps in the average velocity (scaled by half the size of a supercell) at supercritical drift forces

1.5 Cloaking

A very powerful measuring tool is to shoot something, the scatterer, at the object under investigation, and then measure the scattered/reflected signal. This technique is used to study objects of vastly different scales. It has been used e.g. to investigate gravitational lensing [82], where light from stars gets bend by heavy objects and then land in our telescopes, down to measuring elemental particles at CERN [83]. To show how abundant scattering experiments are, be mindful of what you, the reader, are doing at the moment. You are performing a scattering experiment to read this thesis. If you read it on a printed copy, surrounding light (the scatterer) is being scattered on the page and hits your retina (the detector). The ink of the printed text absorbs most of the visible part of the electromagnetic spectrum, while the surrounding paper reflects most of it. This difference in scattering properties of the ink and the paper, allows you to perform the scattering experiment, which we call reading a paper copy. If you read this thesis on a monitor, there are minor differences, e.g. the light is probably emitted by your monitor, and the filtering is likely done by polarizers in your screen, not the ink on the paper. But fundamentally reading this thesis is a scattering experiment done in the visible spectrum.⁴

A proper scatterer has to be chosen to probe the object under investigation. If we for example try to detect the letters on this page using scattering radio waves, we will most likely not be able to read the letters. With a measuring technique used this widely, it is of high interest how the measuring method can be circumvented. There are two main ways how an object can hide from a scattering experiment. Either the object does not interact with the scatterer — one could call this a badly designed experiment — or the object interacts in such a way, that it hides itself from the scatterer. This is called cloaking and it has been shown e.g. in acoustic and electromagnetic systems [84–86].

In this thesis we show how inhomogeneous magnetic patterns with a topologically cloaked region in their center can be designed. Results of computer simulation will be discussed in chapter 3.

⁴Reading is also a scattering experiment for visually impaired readers using a braille device. Their fingers are measuring where the dots in each cell are, by measuring at which height a resistance to force of their finger pushing down occurs.

2 Publications

2.1 Overview of the publications

During this thesis I have worked on five different subjects that are linked in various ways. Four works are either published [1, 2] or under review [3, 4]. The manuscript for the fifth work is in preparation [5]. Therefore, instead of a manuscript we present in chapter 3 the main ideas and simulation results. The overarching theme of all publications is the precise control of the transport of colloidal particles. The thesis mostly focuses on magnetic colloidal particles that move in a fixed plane above or between magnetic patterns [1, 3–5]. Additionally we also investigated the transport of colloidal particles in an array of optical tweezers in publication 2. An overview of how the different works are linked can be found in figure 2.1. The publications in this thesis are presented in chronological order of when we started working on them.

Publications 1 to 3 investigate the transport of colloidal particles in twisted patterns. The first two investigate the angle dependence of the transport of colloidal particles under the influence of twisted patterns when a drift force is applied to the system. Publication 1 gives an in-depth analysis on the dynamics of paramagnetic colloidal particles between twisted magnetic patterns in a constant external magnetic field. Publication 2 shows that the general phenomenology of publication 1 can be reproduced in the system of an array of optical tweezers. In publication 3 we extend the analysis of publication 1 by adding loops of the orientation of the external magnetic field to study the competition between drift and topological transport. Publication 4 and the work presented in chapter 3 do not consider twisted patterns. Instead, in publication 4 we demonstrate how to achieve locally different transport of identical particles subject to the same external magnetic field above a single inhomogeneous magnetic pattern. In chapter 3 we show how to add a cloaked region to magnetic patterns.

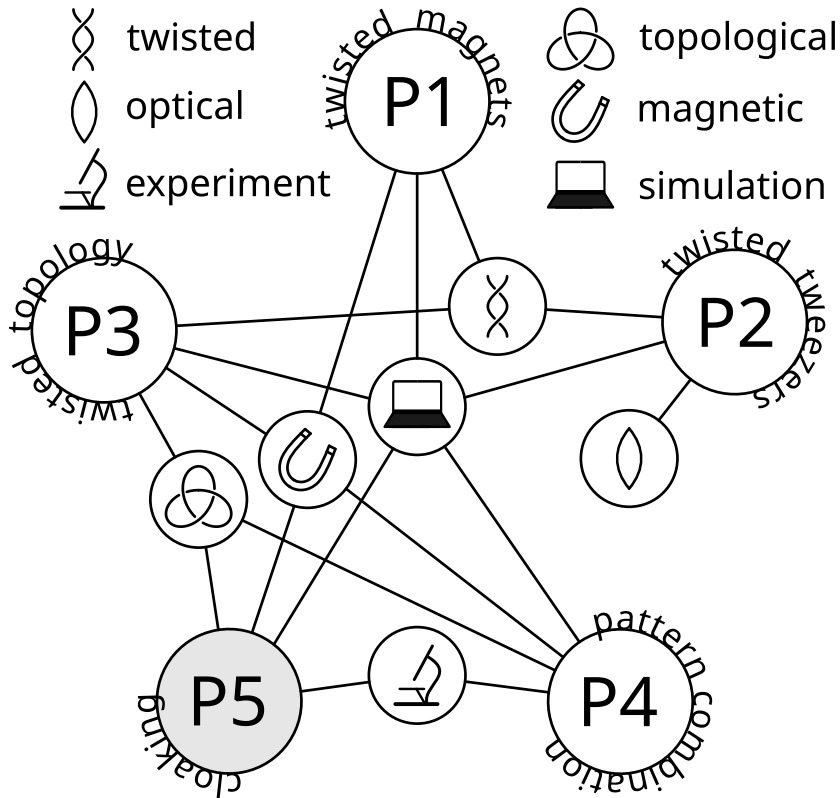


Figure 2.1: Schematic overview of the five works that are part of this thesis. Publications are depicted as large circles with Px in them, where x denotes the number of the publication. The small circles with enclosed symbols illustrate the main concepts of the publications. P5 is shaded gray, as the manuscript is currently in preparation.

2.2 Author contributions

During this cumulative thesis I have worked on four publications, which are published [1, 2] or under review [3, 4]. I am the first author in all the four publications. For all publications I developed the simulation code, ran the simulations, interpreted the data, and wrote the initial draft including the figures.

Additionally, in the first publication with the title “Enhanced colloidal transport in twisted magnetic patterns”, I had the idea of pushing particles through the twisted patterns with a drift force. In the second publication with the title “Colloidal transport in twisted lattices of optical tweezers”, I had the idea

of extending the work of publication 1 to optical tweezers. I reimplemented the simulation code to use the recent adaptive BD algorithm [87]. In the third publication with the title “Competition between drift and topological transport of colloidal particles in twisted magnetic patterns”, I had the idea of combining topological transport with the transport facilitated through a constant drift force. In the fourth publication with the title “Simultaneous and independent topological control of identical microparticles in non-periodic energy landscapes” I had the idea to deform patterns to allow for locally different transport directions. I designed the patterns and the loops to make the particles move along the desired paths.

In the publication currently in preparation, with results discussed in chapter 3, I was one of the designers of the patterns and performed simulations to guide the experimental realization.

2.3 Enhanced colloidal transport in twisted magnetic patterns

In this first work of my thesis we were inspired by the astonishing properties of bilayer graphene twisted to magic angles. We set out to see whether some analogies to the magic angles can be found in a system of magnetic colloidal particles located between twisted magnetic patterns. In order to do so we study with Brownian dynamics simulations the effect of a constant drift force acting on magnetic colloidal particles located between twisted magnetic patterns of hexagonal and square symmetry. Due to the interference of the magnetic field of both patterns, the full magnetic potential develops flat channels. At the magic angles, already discussed in section 1.4, the resulting potential is periodic. There exists an angle dependent critical drift force above which there is transport in patterns twisted to a magic angle. Below the critical force there is no macroscopic transport. There also exists an optimal orientation for the drift force, given by the average direction of the flat channels. The dependence of the critical drift force on the magic angle is different for a pair of twisted square patterns as compared to a pair of twisted hexagonal patterns. In the square patterns the critical force is monotonic as a function of the magic angle, extrapolating to vanishing critical drift force at vanishing twist angle. In twisted hexagonal patterns, however, there are two regimes. At small twist angle, $\alpha_m < 6^\circ$, the critical drift force increases

when the twist angle decreases, while the critical drift force also increases for increasing magic twist angles above 6° . Hence, there exists an optimal twist angle in twisted hexagonal patterns which is $\alpha_m^{\text{optimal}} \approx 6.01^\circ$.

As a next step we investigated the effects of temperature on the colloidal transport. We find that the particles have the highest mobility at vanishing temperature and high drift force. This is not surprising as the high mobility transport is facilitated through the flat channels, and Brownian motion scatters the particles out of the flat channels. We find the following for small temperatures. When the temperature is increased from the zero temperature limit, the mobility decreases, for the case of the drift force being above the critical drift force. In the case of subcritical drift force, Brownian motion helps the colloidal particles to overcome the potential barriers at the corners of supercells, and therefore the overall mobility increases. When the temperature is however increased substantially, the mobility no longer drops, but increases again. Here, the channels next to the flat channels begin to allow for colloidal transport, as the Brownian motion becomes strong enough to let the particles traverse them. The mobility then attains a new local maximum, as for even higher temperatures the particles get scattered out of the channels that allow for transport again.

We conclude the work by investigating the mobility of the colloidal particles for non-magic angles. We observe that there is no macroscopic transport at non-magic angles in the zero temperature limit. At finite temperatures there is macroscopic transport for all angles, but the mobility of the particles is massively increased for magic twist angles.

Publication 1

Enhanced colloidal transport in twisted magnetic patterns

Commun. Phys. **5**, 48 (2022)

Nico C. X. Stuhlmüller¹, Thomas M. Fischer² &
Daniel de las Heras¹

¹Theoretical Physics II, Department of Physics, University of Bayreuth, 95447 Bayreuth, Germany

²Experimental Physics X, Department of Physics, University of Bayreuth, 95447 Bayreuth, Germany.

Supplementary videos and their description can be found on the website of the journal.



<https://doi.org/10.1038/s42005-022-00824-3>

OPEN

Enhanced colloidal transport in twisted magnetic patterns

Nico C. X. Stuhlmüller ¹, Thomas M. Fischer ² & Daniel de las Heras ¹✉

Bilayers of two-dimensional materials twisted at specific angles can exhibit exceptional properties such as the occurrence of unconventional superconductivity in twisted graphene. We demonstrate here that novel phenomena in twisted materials emerges also in particle-based classical systems. We study the transport of magnetic colloidal particles driven by a drift force and located between two twisted periodic magnetic patterns with either hexagonal or square symmetry. The magnetic potential generated by patterns twisted at specific magic angles develops flat channels, which increase the mobility of the colloidal particles compared to that in single patterns. We characterize the effect of the temperature and that of the magnitude of the drift force on the colloidal mobility. The transport is more enhanced in square than in hexagonal twisted patterns. Our work extends twistrionics to classical soft matter systems with potential applications to lab-on-a-chip devices.

¹Theoretische Physik II, Physikalisches Institut, Universität Bayreuth, D-95440 Bayreuth, Germany. ²Experimentalphysik X, Physikalisches Institut, Universität Bayreuth, D-95440 Bayreuth, Germany. ✉email: delasheras.daniel@gmail.com

The emerging field of twistrionics¹ studies the properties of bilayers of two-dimensional materials that are rotated relative to each other by a twist angle. Twisted bilayers generically create a quasiperiodic moiré pattern. However, for specific twist angles, the pattern is periodic with a super unit cell that is a multiple of the primitive unit cell of a monolayer. New properties, not present in the individual monolayers, can emerge in the resulting moiré superlattices^{2–4}. These include superconductivity^{5,6}, ferromagnetism⁷, and correlated insulating states^{8–11} in twisted bilayer graphene. The formation of moiré patterns in twisted materials also affects the properties of both light^{12–16} and acoustic waves^{17–20}.

We extend here twistrionics to a classical, particle-based, system made of magnetic colloidal particles that are located between two periodic magnetic patterns and are driven by a weak drift force. The patterns are twisted at a small angle. For specific magic angles, a partial destructive interference between the magnetic fields of the patterns generates flat channels in the total magnetic potential which results in enhanced long-range anisotropic colloidal transport. We study with Brownian dynamics simulations the effect of the twist angle, the temperature, and the magnitude of the drift force on the mobility of the particles for both square and hexagonal twisted patterns. Our results and conclusions may apply to other twisted materials and constitute the basis for novel lab-on-a-chip applications.

Results

Setup. We study the motion of paramagnetic colloidal particles confined to the middle plane between two parallel periodic magnetic patterns that are separated by a distance Δ , see Fig. 1a. We consider both square and hexagonal periodic lattices with regions of positive and negative magnetization normal to the pattern. The patterns are twisted by an angle α and shifted by half a unit lattice vector.

A uniform external magnetic field \mathbf{H}_{ext} , much stronger than the pattern fields ($\mathbf{H}_{p,i}$ with $i = 1, 2$) points normal to the patterns. At vertical distances comparable or larger than the size of the unit

cell, i.e., $\Delta \gtrsim a$ with a the magnitude of the lattice vectors, the total magnetic potential is dominated by the coupling between external and pattern fields: $V_{\text{mag}} \propto -\sum_i \mathbf{H}_{\text{ext}} \cdot \mathbf{H}_{p,i}$. Hence, only the components of the pattern fields normal to the patterns contribute to the potential. The magnetic potential of single square and hexagonal patterns in presence of \mathbf{H}_{ext} is shown in Fig. 1b. Details about the calculation of V_{mag} are provided in Methods.

Using single patterns it is possible to transport the particles via modulation loops of the orientation of the external field^{21,22}. The loops are closed such that the orientation returns to its initial value after one loop. Loops that wind around special directions of the external field transport the particles by one unit cell after completion of the loop. The transport is topologically protected since the precise shape of the loop is irrelevant, only the winding numbers around the special directions determine the transport. Here, we explore a different type of transport. We keep the external field constant in time and apply a uniform static external drift force, \mathbf{f}_d , in the plane parallel to the patterns, see Fig. 1a. We calculate the particle trajectories using overdamped Brownian dynamics simulations. Hence, the equation of motion for a single particle reads:

$$\xi \dot{\mathbf{r}} = -\nabla V_{\text{mag}}(\mathbf{r}) + \mathbf{f}_d + \boldsymbol{\eta}, \quad (1)$$

where ξ is the friction coefficient against the (implicit) solvent, $\dot{\mathbf{r}}$ is the time derivative of the position vector, and $\boldsymbol{\eta}$ is the delta-correlated random thermal force with standard deviation and amplitude given by the fluctuation-dissipation theorem. We work in units of the magnitude of a lattice vector a , the energy parameter of the magnetic potential ε (see Methods), and the friction coefficient ξ . The intrinsic time-scale is $\tau = \xi a^2 / \varepsilon$ and absolute temperature T is measured in reduced units $k_B T / \varepsilon$ with k_B the Boltzmann constant.

The amplitude of the drift force is small compared to the magnetic forces. Hence, colloidal transport is not possible above a single pattern lacking flat channels. If the temperature is not high enough to overcome the potential barriers, the particles simply

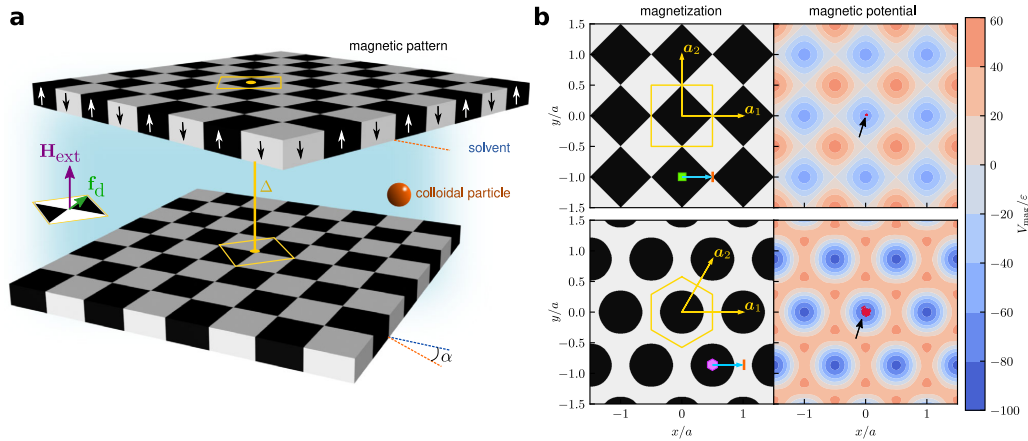


Fig. 1 Setup. **a** Paramagnetic colloidal particles immersed in a solvent are placed between two periodic and parallel magnetic patterns twisted by an angle α and shifted by half a lattice vector. The magnetization of the patterns is indicated by the white and black arrows. A uniform external magnetic field \mathbf{H}_{ext} points normal to the patterns. A drift force \mathbf{f}_d points in the plane of the patterns. **b** Magnetization and magnetic potential V_{mag} of single square and hexagonal patterns. A unit cell together with the lattice vectors \mathbf{a}_i , $i = 1, 2$ are indicated in yellow. The shift vectors applied to the twisted system, $\mathbf{a}_i/2$, are represented in blue. The shift vectors connect points with fourfold (green square) or sixfold (violet hexagon) symmetry to points with twofold symmetry (orange rectangles). The trajectories of a particle above only one of the patterns and located in the central unit cell are plotted in red and indicated by black arrows (drift force $f_d a / \varepsilon = 10$). The temperature is set to $k_B T / \varepsilon = 0.01$ (square pattern) and $k_B T / \varepsilon = 1$ (hexagonal pattern).

diffuse near the minima of the magnetic potential, see characteristic trajectories in Fig. 1b. The situation is different for the case of twisted patterns.

Enhanced transport in twisted patterns. At specific twist angles, the so-called magic angles, a periodic moiré pattern with supercells of size roughly given by $a/(2 \sin(\alpha/2))$ develops in the magnetic potential, see Fig. 2 and Supplementary Fig. 1. At a magic angle α_m^p with $p = \{\text{sq, hex}\}$ for square and hexagonal patterns, respectively, a lattice site of the twisted pattern coincides with another lattice site of the other pattern (see Methods). At the center of the supercells V_{mag} resembles that of the underlying square or hexagonal patterns. However, near the edges of a supercell, a change towards a twofold symmetry (stripes) occurs. The stripes in V_{mag} are almost flat compared to the inner regions due to a partial destructive interference of the magnetic field of both patterns. A small drift force is therefore able to push the particles along the edges of the supercells, while its effect is negligible for particles inside the supercells, see particle trajectories in Fig. 2 and Supplementary Movies 1, 2.

The patterns are shifted by half the first lattice vector such that points with different rotational symmetries (see Fig. 1b) coincide

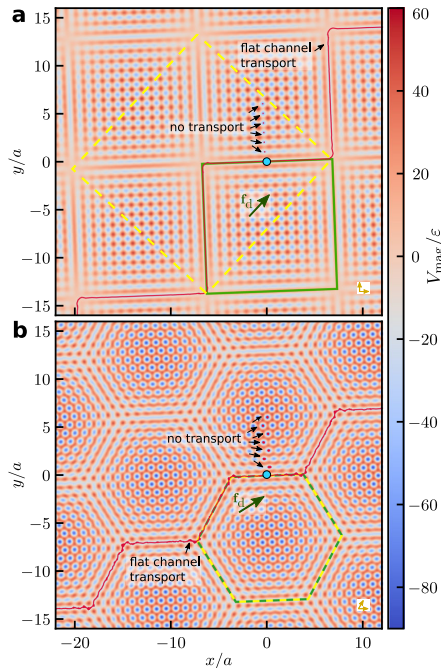


Fig. 2 Twisted patterns. Magnetic potential, V_{mag} , in square (a) and hexagonal (b) twisted patterns. The patterns are twisted at a magic angle of $\alpha_m^{\text{sq}} \approx 4.24^\circ$ in (a) and $\alpha_m^{\text{hex}} \approx 4.41^\circ$ in (b) around the axis normal to the patterns that passes through the origin (blue circle). The lattice vectors, \mathbf{a}_1 and \mathbf{a}_2 with \mathbf{a}_1 parallel to the x-axis, of the untwisted pattern are represented with yellow arrows. The untwisted pattern is shifted by $\mathbf{a}_1/2$. A supercell (green solid line) and a unit cell (dashed yellow line) of the twisted patterns is highlighted in each pattern together with trajectories followed by both, particles transported via flat channels and particles stuck inside the supercells, as indicated. The magnitude of the drift force is $f_d a/\epsilon = 10$ and its direction is indicated by a green arrow. The temperature is $k_B T/\epsilon = 0.01$ in (a) and $k_B T/\epsilon = 0.8$ in (b).

in the combined system. The shift creates a twofold symmetric point of the magnetic potential at the origin (axis of rotation). This is only possible by shifting the patterns by half a lattice vector and it maximizes the destructive interference between the fields of both patterns. Any lattice vector can be used since the resulting magnetic potentials are the same up to a global rotation. The shift generates a combined pattern which is anisotropic. The curvature of the magnetic potential at the edges of the supercell is either negative (V_{mag} is minimum) or positive (V_{mag} is maximum), see Fig. 2 and Supplementary Fig. 1. For weak drift forces, the particles are transported only along the edges for which the potential is a minimum. In analogy to the flat bands that occur in reciprocal space in twisted graphene³, we call these edges in real space flat channels. It is worth mentioning that there exists a correspondence between real space and reciprocal space, and that flat channels in real space, similar to those in Fig. 2, also occur in twisted bilayers of 2D materials²³. At magic twist angles, the flat channels of neighboring cells are connected and the particles can be transported over macroscopic distances.

The roughness of the potential increases progressively from the edges towards the center of the supercell. At multiple distances of a from an edge with a flat channel and parallel to it there exist secondary channels. Secondary channels also occur parallel to the edges for which V_{mag} is maximum. There, the first two secondary channels are located at a distance of $a/2$ from the edge. Along the secondary channels, the magnetic potential is still flat enough to support transport for either strong driving or high temperature as demonstrated below. The smaller the magic angle, the larger the supercell is and more secondary channels are sufficiently flat to transport particles. In addition, the potential along both the secondary and the flat channels gets flattened by decreasing the twist angle. For all magic angles, the flat channel (located at the edges of the supercell) is always the flattest one and requires therefore the minimal drift force to transport particles.

Critical drift force. To investigate the minimal (critical) drift force f_c required to achieve macroscopic transport, we point the drift force along the average direction between two consecutive flat channels, see Fig. 2 and Methods, and set the temperature to zero such that the diffusive motion due to thermal fluctuations does not hinder the phenomenology. Then we measure the mobility of the colloidal particles, μ , defined as the average velocity divided by the amplitude of the drift force, see details in Methods. The mobility vanishes for small drift forces, increases abruptly at a given critical value f_c , and it saturates for strong drift forces, see illustrative examples in Fig. 3a. The value and the behavior of the critical drift force depend on both the type of pattern and the magic angle α_m^p , see Fig. 3b.

At the corners of a supercell (intersection between two edges), the magnetic potential has more structure than in the center of the edges, see Fig. 2. Hence, for both hexagonal and square twisted patterns, the transport along the edges of the supercells requires weaker drift forces than the transport over the corners. The particles spend a significant amount of time crossing the corners. This effect can be observed in Supplementary Movies 1 and 2 which show the particle dynamics in square and hexagonal twisted patterns, respectively. Plots of the crossing time at the corners for different temperatures and magnitudes of the drift force are shown in Supplementary Fig. 2. In square twisted patterns the height of the magnetic potential near the corners increases with the twist angle, and also the potential at the edges becomes rougher. These two effects cause the critical force to increase monotonically with the twist angle, Fig. 3b. In the limit $\alpha_m^{\text{sq}} \rightarrow 0$ the critical force vanishes and macroscopic transport occurs for an infinitesimally small drift force. Note that in the limit of vanishing twist it is also

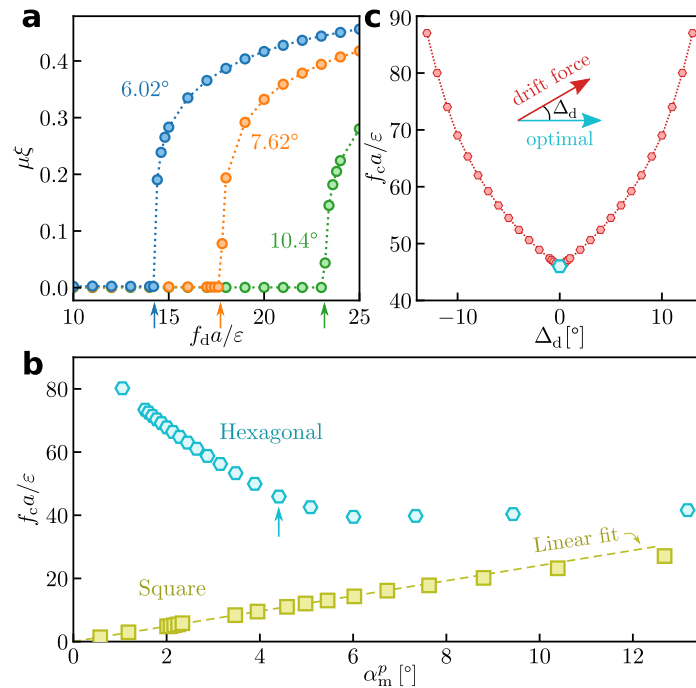


Fig. 3 Critical force. **a** Mobility μ in twisted square patterns as a function of the magnitude of the drift force f_d for three magic angles. The vertical arrows indicate the value of the critical forces for each magic angle. **b** Magnitude of the critical force f_c required to transport particles at $T = 0$ as a function of the magic angle α_m^p in twisted square (green) and hexagonal (blue) patterns. The dashed green line is a linear fit for magic angles $\alpha_m^{sq} < 4^\circ$ in twisted square patterns. The critical force extrapolates to zero in the limit $\alpha_m^{sq} \rightarrow 0$. **c** Magnitude of the critical force f_c as a function of the direction of the drift force Δ_d (measured as the angle formed by the drift force and the optimal drift force). Data at $T = 0$ for hexagonal patterns twisted at a magic angle $\alpha_m^{hex} \approx 4.41$, indicated with a vertical arrow in **(b)**. Dotted lines in panels **(a)** and **(c)** are guides for the eye.

necessary to have both patterns in order to create a destructive interference along the direction of the shift.

In twisted hexagonal patterns, the potential at the edges of the supercells also gets rougher by increasing the twist angle. However, in contrast to twisted square patterns, the potential at the corners of a supercell becomes flattened by increasing the magic angle. The balance between these opposing effects generates a non-monotonic critical force in hexagonal twisted patterns, Fig. 3b. By increasing the magic angle, the critical force first decreases, then it reaches a minimum at $\alpha_m^{hex} \approx 6.01^\circ$, and finally it increases again.

Direction of the drift force. To investigate the effect of the direction of the drift force, we fix the twist angle to a magic angle in hexagonal patterns and calculate the critical force as a function of Δ_d , which is the angle between the drift force and the average direction between two consecutive flat channels. Any deviation of the drift force from the average direction between two consecutive flat channels increases the critical force, see Fig. 3c. For deviations larger than those shown in Fig. 3c transport along the flat channels is no longer possible. Instead, a drift force ($\sim 200 \epsilon/a$) stronger than the magnetic forces of the single patterns is then required to transport the particles that no longer follow the flat channels. We also show in Supplementary Fig. 3 the critical force as a function of the magic angle for different directions of the drift force.

Finite temperature. We next characterize the effect of Brownian motion on colloidal transport. We show in Fig. 4 the dynamical

phase diagram of the colloidal mobility in the plane of temperature and magnitude of the drift force for patterns twisted at a magic angle.

The highest mobility occurs for strong forces and low temperatures. By increasing the temperature at a constant magnitude of the drift force, the mobility first decreases and then increases again. This effect is more prominent in the square case, Fig. 4a, although it also occurs in hexagonal twisted patterns, Fig. 4b. The first minimum in the mobility is caused by particles getting scattered off the central flat channel due to Brownian motion. (A conceptually related Pomeranchuk effect in twisted graphene^{24,25} in which increasing temperature induces a metal-insulator transition has been recently observed.) The secondary channel does not allow for macroscopic transport in a given range of temperatures and force amplitudes. However, a further increase in the temperature allows transport along the secondary channel (larger thermal fluctuations permit the particles to cross the potential barriers) and the mobility increases again. At even higher temperatures the mobility decreases again since particles get scattered into the next secondary channel. This oscillatory behavior in the mobility continues until the thermal energy is large enough compared to the magnetic potential energy and the transport becomes diffusive.

A similar argument explains also the negative differential mobility observed by increasing the magnitude of the drift force at finite temperature ($T > 0$). First μ increases, as expected, and then it decreases. If a particle leaves the flat channel at the corners of a supercell (due to Brownian motion), it is driven away from the corner faster for stronger f_d . This decreases the mobility since the probability that a particle returns to the flat channel decreases

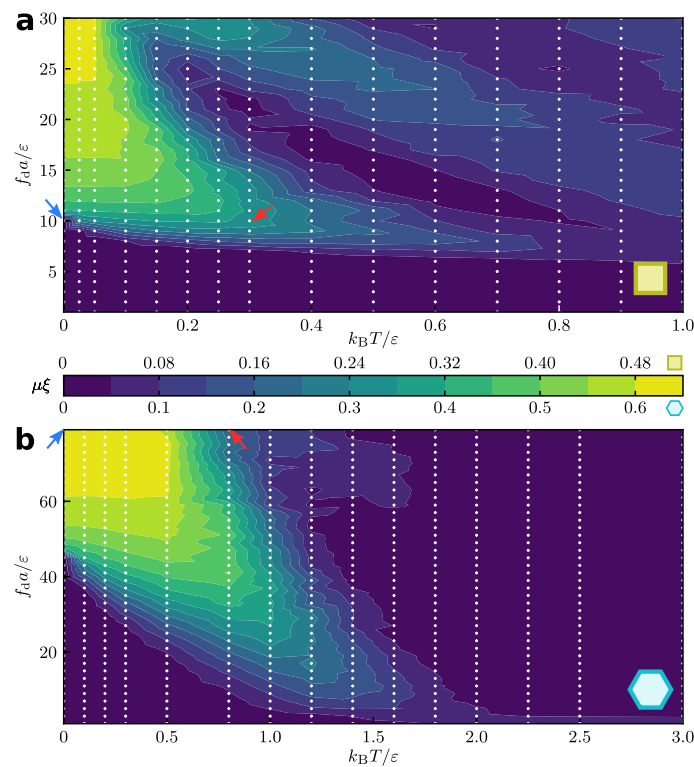


Fig. 4 Dynamical phase diagram. Colloidal mobility μ (see color bar) in the plane of magnitude of the drift force f_d and temperature T for twisted **a** square patterns at a magic angle $\alpha_m^{\text{sq}} \approx 4.24^\circ$ and **b** hexagonal patterns at a magic angle $\alpha_m^{\text{hex}} \approx 4.41^\circ$. The white dots indicate the selected temperatures and magnitudes of the drift force simulated to create the plots. The blue and red arrows indicate the position in the diagrams of selected state points.

with the distance to the corners. A further increase in the drift force enables transport along a secondary channel and hence increases the mobility again. This oscillatory behavior seems to continue until the external drift force completely dominates the magnetic forces.

In square twisted patterns, the secondary channels that are first activated for transport are those located at a distance $a/2$ from the edges for which V_{mag} is maximum (the edges without flat channels), see Supplementary Movie 3. There the potential is flatter than along the secondary channels located at a distance a from the flat channels and parallel to them. In contrast, in twisted hexagonal patterns, the active secondary channels are those parallel to the flat channels. Transport along the secondary channels located in edges where V_{mag} is maximum does not occur simply because \mathbf{f}_d is perpendicular to those channels. Supplementary Movies 4 and 5 show the motion of particles in twisted hexagonal patterns using a flat and a secondary channel, respectively. (In Supplementary Movie 4 at time $t = 11.48\tau$, a particle jumps from a secondary channel into the flat channel, where it is transported much faster.) The different type of secondary channels active for transport in square and hexagonal twisted patterns is likely the reason behind the different amplitudes of the second peak of the mobility in the dynamical phase diagrams, see Fig. 4.

Critical force and transport for non-magic angles. So far we have discussed the transport in patterns twisted at magic angles.

For non-magic angles, the magnetic potential is in general no longer periodic but quasiperiodic (there exist other non-magic angles for which the potential is also periodic but the unit cell contains several supercells different from each other and the transport is not optimal, see Methods and Supplementary Note 1). For non-magic angles, each supercell differs slightly from its neighbors and the flat channels are not as flat as those at a magic angle. As a result the drift force required to transport the particles increases as compared to the magic case.

For a nonperiodic magnetic potential, the critical force depends on both the initial location of the particle and the required traveled distance that is imposed a priori to calculate f_c . In Fig. 5 we plot f_c as a function of the twist angle (scaled with the magic angle) for square and hexagonal twisted patterns. The force is calculated by averaging over a total of 100 trajectories of particles that are at time zero-initialized on different flat channels. Three data sets corresponding to the average critical force required to transport the particles a distance equivalent to the length of 10, 100, and 1000 supercells are shown. The critical force has a sharp minimum at the magic angle which gets narrower by increasing the traveled distance used to compute f_c . The non-smooth behavior of the critical force at non-magic angles is to be expected due to the Diophantine equations that determine the periodicity of twisted patterns, see Methods and Supplementary Note 1. We show in Supplementary Note 1 that for any angle for which the potential is nonperiodic the particles encounter at some point the most unfavorable magnetic potential along the flat channel.

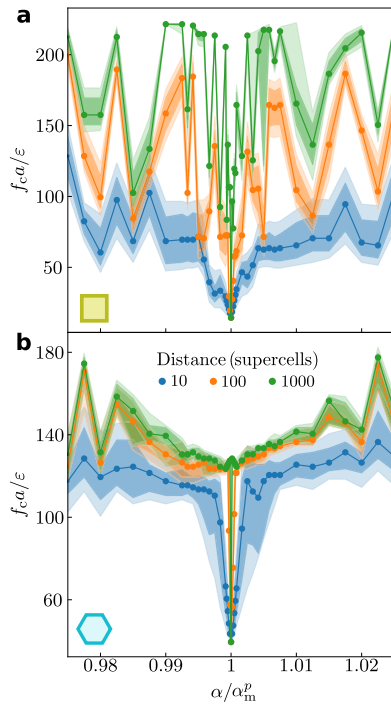


Fig. 5 Critical force at non-magic angles. Zero-temperature critical force f_c required to transport a particle as a function of the twist angle α scaled with the magic angle α_m^p in **a** square $\alpha_m^{sq} = 6.026^\circ$ and **b** hexagonal $\alpha_m^{hex} = 6.009^\circ$ patterns. The different data sets show the critical force required to transport the particle at a distance equivalent to 10 (blue), 100 (orange), and 1000 (green) lengths of a supercell. Data were obtained by averaging over the trajectories of 100 particles initialized on different flat channels. The distribution of the individual measurements is illustrated by the shadow regions, which show the minimum and the maximum values of f_c required to transport 50% (dark regions) and 80% (light regions) of the particles.

Hence, even the smallest deviation from a magic angle causes a substantial increase of the critical force required to transport the particles indefinitely (continuous flow).

In hexagonal twisted patterns, the continuous flow at non-magic angles and strong drift forces occur as in the magic case via the flat channels (at least for the deviations from the magic case shown in Fig. 5). At drift forces even higher than those in Fig. 5b the particles will eventually leave the flat channels in the hexagonal twisted patterns and follow the direction of \mathbf{f}_d . In square patterns, the particles leave the flat channels at non-magic angles and large drift forces. Hence, the continuous flow happens mostly through the entire pattern (see Supplementary Movie 6). The flat channels are deeper and narrower in hexagonal than in square twisted patterns which causes the differences in the continuous flow at non-magic angles.

We plot in Fig. 6 the average distance d_t traveled by a particle located initially at the origin (fixed point of rotation) as a function of the scaled twist angle α/α_m^p . Different magic angles α_m^p are analysed at a fixed magnitude of the drift force. We show the zero-temperature limit (Fig. 6a, b) as well as finite temperature cases (Fig. 6c, d) for both squares (Fig. 6a, c) and hexagonal (Fig. 6b, d) twisted patterns. The value of d_t is sensitive to the

initial position of the particle. Nevertheless, these curves are useful to understand the physical mechanisms behind particle transport since their global characteristics are robust. The magnitude of the drift forces is above that of the critical force of the corresponding magic angle but below the magnitude required to achieve continuous flow at non-magic angles (with the exception of the red-solid lines in Fig. 6 in which f_d is below the critical force at the magic angle). The required drift forces and therefore the traveled distances are higher in hexagonal than in square twisted patterns. (Recall that the critical force is larger in hexagonal than in square twisted patterns, see Fig. 3b.)

The zero-temperature limit reflects how the magnetic potential changes with the twist angle. In the inset of Fig. 6a we show how the traveled distance changes when the drift force acts during longer periods of time $t_3 > t_2 > t_1$ (see also Supplementary Movie 7). In patterns twisted at a magic angle, the number of supercells traveled is proportional to the time (provided that the drift force is above the critical one). At non-magic angles, the particles hit at some point a blocked corner/edge and stay there forever. The smaller the deviation from the magic angle is, the further from the origin this blocking occurs. As the twist angle approaches the magic angle, the region around the fixed point of rotation becomes increasingly similar to the magic case and therefore the particles travel longer distances but they eventually hit a dead end and the motion stops. In the limit of drift forces acting for an infinite period of time and comparable in amplitude to the critical force of the closest magic angle, the colloidal mobility at $T=0$ is only different than zero if the patterns are twisted at a magic angle.

At zero-temperature, d_t grows discontinuously by approaching the magic angle, Fig. 6a, b. The jumps in d_t between two consecutive plateaus correspond to roughly the distance traveled across one supercell. Note that the larger scale of the plot in the hexagonal case, Fig. 6b, hinders the visualization of the plateaus but they still occur as shown in the inset.

The distance that the particles travel at the magic angle increases by decreasing α_m^p in square twisted patterns and it decreases in hexagonal patterns. This different behavior is, as in the case of the critical drift force, due to how the magnetic potential changes at the corners of the supercells by varying the magic angle in each type of twisted pattern.

The effect of the critical drift force for magic angles is illustrated in the data set for square patterns at $\alpha_m^{sq} \approx 4.24^\circ$ (red line in Fig. 6a). The magnitude of the drift force, $f_d a / \epsilon = 10$, is below the zero-temperature critical drift force for this magic angle, see Fig. 3, and therefore the transport stops completely at an angle smaller than the magic angle. However, thermal fluctuations are able to reactivate the transport (red line in Fig. 6c). At finite temperatures (Fig. 6c, d) the transport does no longer stop when a particle hits a blocking region since Brownian motion allows the particle to traverse the potential barrier (the mobilities are therefore different than zero). The temperature enhances, in general, the transport at non-magic angles. In both types of patterns, the effect is more prominent for small twist angles (blue lines in Fig. 6). However, at magic angles (and provided that the drift force is large enough to transport the particles at $T=0$) the traveled distance is smaller at finite temperature than at $T=0$. At magic angles, the magnetic potential is optimal for transport and Brownian motion only reduces its efficiency.

Discussion

The patterns can be experimentally realized using e.g., exchange-bias thin magnetic films irradiated through a lithographic mask^{26,27} as well as garnet films^{28,29}. Using micrometer-sized colloidal particles at a distance comparable to the length of a lattice vector above these patterns^{21,22} results in magnetic potential energies significantly larger than the thermal energy (at room

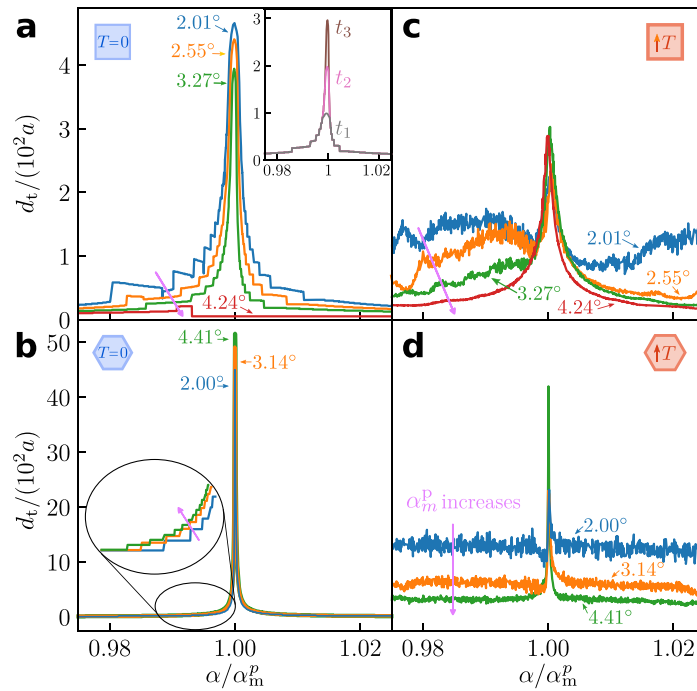


Fig. 6 Transport at magic and non-magic angles. Average distance traveled by a particle as a function of the twist angle α (scaled with the magic twist angle α_m^p) at zero-temperature (**a, b**) and finite temperature (**c, d**) in either square (**a, c**) or hexagonal (**b, d**) twisted patterns. Data sets for several magic angles are presented, as indicated. The magic angle increases in the direction of the pink arrows. The traveled distance is obtained by averaging the motion of 100 particles located initially at the origin (axis of rotation of the patterns) and driven by a drift force (acting during 100τ) of magnitude $f_d a / \epsilon = 10$ in the square (**a, b**) and $f_d a / \epsilon = 80$ in the hexagonal (**c, d**) patterns. The temperature is $T = 0$ in (**a**) and (**b**), $k_B T / \epsilon = 0.3$ in (**c**) and $k_B T / \epsilon = 0.8$ in (**d**). The drift forces and temperatures used here are indicated with colored arrows in Fig. 4. The inset in (**a**) shows data for a drift force acting during $t_1 = 25\tau$, $t_2 = 50\tau$, and $t_3 = 75\tau$ (at $T = 0$ and $\alpha_m^p = 3.27^\circ$).

temperature). Hence, the use of similar setups^{21,22} would result in experiments on twisted patterns that are effectively close to the zero-temperature limit. The observation of the finite temperature effects discussed here should be possible by either decreasing the magnetic forces (e.g., weaker patterns and larger colloid-pattern distance) or increasing the Brownian force (using e.g., magnetic nanocolloids). As in the case of single patterns^{21,22}, we expect good agreement between simulations and experiments in twisted magnetic patterns.

Regarding the drift force, colloidal particles respond to several types of external fields³⁰. Gravitational³¹ and electric³² fields, as well as pressure³³ and temperature³⁴ gradients, are possible means to experimentally achieve such drift forces. We estimate that the strength of the Earth's gravitational field is above the critical force required to transport micrometer-sized particles in solvents with a significant particle-solvent density difference. Instead of a drift force, it would be interesting to use self-propelled active particles³⁵. The twisted patterns could then be used to study and possibly tune transport properties of active Brownian particles³⁶, such as e.g., the polarization³⁷, in complex environments³⁸.

The colloidal transport using flat channels in twisted patterns is faster than the topologically protected transport in single patterns^{21,22}. There, the particles are adiabatically driven via modulation of the orientation of the external magnetic field. In twisted patterns, topologically protected transport is also available and it can be used to e.g., initially move the colloidal particles from the inside

of the supercells towards the flat channels. The availability of two types of transport mechanisms, namely flat channels and topological transport, together with the control over the flat channels offered by the twist angle are two advantages over static channels added directly to the potential in e.g., lab-on-a-chip devices.

The critical force required to transport the particles is always significantly smaller in the square than in hexagonal twisted patterns and therefore the enhanced colloidal transport is more pronounced in twisted square patterns. The effect is specially relevant approaching the limit of very small twist angles since the critical force vanishes in the case of square twisted patterns. Hence, given (i) the similarities between our colloidal system and electronic systems and (ii) the correspondence in electronic systems between flat bands in reciprocal space and flat channels in real space, it is plausible to think that twisted bilayers of two-dimensional materials with square unit cells^{39–44} are promising candidates for new electronic applications.

Methods

Magnetic potential. The total magnetic field at position \mathbf{r} is $\mathbf{H}(\mathbf{r}) = \mathbf{H}_{p,1}(\mathbf{r}) + \mathbf{H}_{p,2}(\mathbf{r}) + \mathbf{H}_{\text{ext}}$, with $\mathbf{H}_{p,i}$ the magnetic field of pattern $i = 1, 2$ and \mathbf{H}_{ext} the uniform external magnetic field, which is normal to the patterns. Hence the magnetic potential acting on a paramagnetic particle with effective volume v_{eff} is

$$V_{\text{mag}} = -v_{\text{eff}} \chi \mu_0 \mathbf{H}^2(\mathbf{r}), \quad (2)$$

with μ_0 the vacuum permeability and χ the particle susceptibility. We scale the particles down to effective point particles and increase their susceptibility such that

$v_{\text{eff}}\chi$ remains constant. If the vertical distance between the particle and the patterns is sufficiently large (comparable or larger than the size of the unit cell of the pattern) only the first Fourier-mode of each pattern contributes significantly to the magnetic field^{21,45}. Additionally, the potential is dominated by the cross-term $V_{\text{mag}} \approx -2v_{\text{eff}}\mu_0\mathbf{H}_{\text{ext}} \cdot (\mathbf{H}_{p,1} + \mathbf{H}_{p,2})$ since \mathbf{H}_{ext} is uniform and much stronger than $\mathbf{H}_{p,i}$. In this limit, the system-specific parameters like the amplitudes of all magnetic fields and the distance between the patterns can be absorbed into a single constant c . The potential is therefore given by

$$V_{\text{mag}} = -\chi e a q^p \sum_{i=1}^N \left[\cos(\mathbf{q}_i \cdot (\mathbf{r} - \frac{\mathbf{a}_i}{2})) + \cos(\mathbf{R}_\alpha \mathbf{q}_i \cdot \mathbf{r}) \right], \quad (3)$$

where $N = 4, 6$ for the square and hexagonal patterns, respectively, \mathbf{R}_α denotes a rotation matrix by the twist angle α around the direction normal to the pattern, and the vectors \mathbf{q}_i are given by

$$\mathbf{q}_i = q^p \begin{pmatrix} \sin(2\pi i/N) \\ \cos(2\pi i/N) \end{pmatrix}, \quad (4)$$

where the superscript $p = \{\text{sq}, \text{hex}\}$ and $q^{\text{sq}} = 2\pi/a$ in the square pattern and $q^{\text{hex}} = 2\pi/(a \sin(\pi/3))$ in the hexagonal pattern. The first term in the right-hand side of Eq. (3) corresponds to the pattern shifted by $\mathbf{a}_i/2$ and the second term to the pattern twisted by an angle α . Shifting the patterns by a different quantity also creates, in general, structures similar to flat channels. However, a shift by half a lattice vector minimizes the roughness of the magnetic potential at the flat channels and specially at the corners of the supercells by maximizing the destructive interference between the field of both patterns (see Supplementary Note 1). Further mathematical details about the single hexagonal and square patterns can be found in previous works^{21,45}.

Computer simulations. The particle trajectories are calculated with overdamped Brownian dynamics simulations. We discretize the equation of motion, Eq. (1), using a time step $dt/\tau = 10^{-5}$ and integrate it in time via the standard Euler algorithm.

Magic angles. The magnetic potential of patterns twisted by an angle α develop moiré interference patterns at length scales roughly given by $a/(2 \sin(\alpha/2))$. At magic twist angles the combined magnetic potential of both patterns becomes periodic at the length scale of the supercells. In the twisted square pattern, the potential has a checkerboard layout of two alternating supercells, which can be transformed into each other by a rotation of π around their centers. The unit cell of a twisted square pattern is therefore twice the size of the supercell, see Fig. 1a. For hexagonal patterns twisted at a magic angle, the unit cell and the supercells coincide, see Fig. 1b. In both hexagonal and square twisted patterns there exist other twist angles (non-magic) for which the patterns are also periodic but the periodicity is recovered only after multiple supercells (which can not be transformed into each other with similarity transformations). In those patterns, the flat channels are not connected over macroscopic distances and hence the colloidal transport is not enhanced as in the magic case, see Supplementary Note 1. The mathematical condition for a magic twist angle, in which every supercell is equivalent, can be expressed as a Diophantine problem^{46,47} with solution

$$\alpha_m^{\text{sq}} = 2 \arcsin \left(\frac{1}{2\sqrt{k^2 + k + 1/2}} \right), \quad (5)$$

$$\alpha_m^{\text{hex}} = \arccos \left(\frac{3(2k+1)^2 - 1}{3(2k+1)^2 + 1} \right), \quad (6)$$

where k is a natural number. To obtain these expressions in the hexagonal case, we adjusted the procedure by Shallcross et al.⁴⁶ to include the constraint of having identical supercells.

Drift force. In both hexagonal and square twisted patterns the flat channels develop along consecutive edges of the supercells. The drift force points along the bisector of the directions of the flat channels, as shown in Fig. 2. Hence,

$$\mathbf{f}_d = f_d \begin{pmatrix} \cos \alpha_d^p \\ \sin \alpha_d^p \end{pmatrix}, \quad (7)$$

where the angle α_d^p is given by

$$\alpha_d^{\text{sq}}(k) = \alpha_m^{\text{sq}}(k)/2 + \text{sgn}(\alpha_m^{\text{sq}}(k)) \frac{(-1)^{k+1} \pi}{4}, \quad (8)$$

$$\alpha_d^{\text{hex}}(k) = \alpha_m^{\text{hex}}(k)/2 + \text{sgn}(\alpha_m^{\text{hex}}(k)) \frac{(-1)^{k+1} \pi}{6}, \quad (9)$$

in square and hexagonal twisted patterns, and $k \in \mathbb{N}$. The factor $(-1)^{k+1}$ and the sign of the magic angle in the above expressions reflect the fact that the edges that support transport alternate from one magic angle to the next one as well as by changing the sign of the twist angle. A drift force pointing along a different

direction will also induce transport provided that the force is not orthogonal to any of the directions of the flat channels.

Critical force. To estimate the value of the critical force we assume the following form for the mobility curves (Fig. 3a) near the transition from no-transport to transport

$$\mu(f_d) = \mu_0 \left(\frac{f_d - f_c}{f_c} \right)^\gamma, \quad (10)$$

where μ_0 , the critical force f_c and γ are used as fitting parameters.

Mobility. We define the mobility μ as the average distance traveled by the particles divided by the amplitude of the drift force

$$\mu = \frac{\langle |\mathbf{r}(t_f) - \mathbf{r}(t_i)| \rangle}{(t_f - t_i) f_d}. \quad (11)$$

We calculate the average distance $\langle |\mathbf{r}(t_f) - \mathbf{r}(t_i)| \rangle$ by initializing 100 non-interacting particles at the origin (axis of rotation) and let them travel under the influence of the drift force for a total time of 100 τ . To eliminate the dependence on the initial conditions we average the distances traveled by the particles during the second half of the simulation, i.e., $t_i = 50\tau$ and $t_f = 100\tau$ in Eq. (11). However, to characterize the system at non-magic angles, we consider the full trajectories in Fig. 6 (such that all particles share the same initial position). Therefore, the mobilities calculated with the distances reported in Fig. 6 differ slightly from those shown in Fig. 4.

Data availability

All the data supporting the findings are available from the corresponding author upon reasonable request.

Received: 22 December 2021; Accepted: 4 February 2022;

Published online: 02 March 2022

References

- Carr, S., Massatt, D., Fang, S., Cazeaux, P., Luskin, M. & Kaxiras, E. Twistronics: manipulating the electronic properties of two-dimensional layered structures through their twist angle. *Phys. Rev. B* **95**, 075420 (2017).
- Lopes dos Santos, J. M. B., Peres, N. M. R. & Castro Neto, A. H. Graphene bilayer with a twist: electronic structure. *Phys. Rev. Lett.* **99**, 256802 (2007).
- Suárez Morell, E., Correa, J. D., Vargas, P., Pacheco, M. & Barticevic, Z. Flat bands in slightly twisted bilayer graphene: tight-binding calculations. *Phys. Rev. B* **82**, 121407 (2010).
- Bistritzer, R. & MacDonald, A. H. Moiré bands in twisted double-layer graphene. *Proc. Natl Acad. Sci. USA* **108**, 12233 (2011).
- Cao, Y. et al. Unconventional superconductivity in magic-angle graphene superlattices. *Nature* **556**, 43 (2018).
- Yankowitz, M. et al. Tuning superconductivity in twisted bilayer graphene. *Science* **363**, 1059 (2019).
- Sharpe, A. L. et al. Emergent ferromagnetism near three-quarters filling in twisted bilayer graphene. *Science* **365**, 605 (2019).
- Cao, Y. et al. Correlated insulator behaviour at half-filling in magic-angle graphene superlattices. *Nature* **556**, 80 (2018b).
- Shen, C. et al. Correlated states in twisted double bilayer graphene. *Nat. Phys.* **16**, 520 (2020).
- Lu, X. et al. Superconductors, orbital magnets and correlated states in magic-angle bilayer graphene. *Nature* **574**, 653 (2019).
- Nuckolls, K. P. et al. Strongly correlated Chern insulators in magic-angle twisted bilayer graphene. *Nature* **588**, 610 (2020).
- Zhao, Y., Belkin, M. & Alù, A. Twisted optical metamaterials for planarized ultrathin broadband circular polarizers. *Nat. Commun.* **3**, 870 (2012).
- Sunku, S. S. et al. Photonic crystals for nano-light in moiré graphene superlattices. *Science* **362**, 1153 (2018).
- Hu, G. et al. Topological polaritons and photonic magic angles in twisted α -MoO₃ bilayers. *Nature* **582**, 209 (2020).
- Wang, P. et al. Localization and delocalization of light in photonic moiré lattices. *Nature* **577**, 42 (2020).
- Hu, G., Qiu, C.-W. & Alù, A. Twistronics for photons: opinion. *Opt. Mater. Express* **11**, 1377 (2021).
- Deng, Y. et al. Magic-angle bilayer phononic graphene. *Phys. Rev. B* **102**, 180304 (2020).
- Rosendo López, M., Peñaranda, F., Christensen, J. & San-Jose, P. Flat bands in magic-angle vibrating plates. *Phys. Rev. Lett.* **125**, 214301 (2020).

19. Zheng, S. et al. Landau levels and van der Waals interfaces of acoustics in Moiré phononic lattices. Preprint at <https://arxiv.org/abs/2103.12265> (2021).
20. Gardezi, S. M., Pirie, H., Carr, S., Dorrell, W. & Hoffman, J. Simulating twistorics in acoustic metamaterials. *2D Mater.* **8**, 031002 (2021).
21. Loehr, J., Loenne, M., Ernst, A., de las Heras, D. & Fischer, T. M. Topological protection of multiparticle dissipative transport. *Nat. Commun.* **7**, 11745 (2016).
22. Mirzaee-Kakhki, M. et al. Simultaneous polydirectional transport of colloidal bipeds. *Nat. Commun.* **11**, 4670 (2020).
23. Carr, S., Massatt, D., Luskin, M. & Kaxiras, E. Duality between atomic configurations and Bloch states in twistrionic materials. *Phys. Rev. Res.* **2**, 033162 (2020).
24. Rozen, A. et al. Entropic evidence for a Pomeranchuk effect in magic-angle graphene. *Nature* **592**, 214 (2021).
25. Saito, Y. et al. Isospin Pomeranchuk effect in twisted bilayer graphene. *Nature* **592**, 220 (2021).
26. Chappert, C. et al. Planar patterned magnetic media obtained by ion irradiation. *Science* **280**, 1919 (1998).
27. Kuświk, P. et al. Colloidal domain lithography for regularly arranged artificial magnetic out-of-plane monodomains in Au/Co/Au layers. *Nanotechnology* **22**, 095302 (2011).
28. Hansen, P. & Krumme, J.-P. Magnetic and magneto-optical properties of garnet films. *Thin Solid Films* **114**, 69 (1984).
29. Tierno, P., Sagués, F., Johansen, T. H. & Fischer, T. M. Colloidal transport on magnetic garnet films. *Phys. Chem. Chem. Phys.* **11**, 9615 (2009).
30. Löwen, H. Colloidal dispersions in external fields: recent developments. *J. Phys. Condens. Matter* **20**, 404201 (2008).
31. Köppl, M., Henseler, P., Erbe, A., Nielaba, P. & Leiderer, P. Layer reduction in driven 2d-colloidal systems through microchannels. *Phys. Rev. Lett.* **97**, 208302 (2006).
32. Velev, O. D. & Bhatt, K. H. On-chip micromanipulation and assembly of colloidal particles by electric fields. *Soft Matter* **2**, 738 (2006).
33. Frank, M., Anderson, D., Weeks, E. R. & Morris, J. F. Particle migration in pressure-driven flow of a Brownian suspension. *J. Fluid Mech.* **493**, 363 (2003).
34. Piazza, R. 'Thermal forces': colloids in temperature gradients. *J. Phys. Condens. Matter* **16**, S4195 (2004).
35. Marchetti, M. C. et al. Hydrodynamics of soft active matter. *Rev. Mod. Phys.* **85**, 1143 (2013).
36. Romanczuk, P., Bär, M., Ebeling, W., Lindner, B. & Schimansky-Geier, L. Active Brownian particles. *Eur. Phys. J. Spec. Top.* **202**, 1 (2012).
37. Hermann, S. & Schmidt, M. Active interface polarization as a state function. *Phys. Rev. Res.* **2**, 022003 (2020).
38. Bechinger, C. et al. Active particles in complex and crowded environments. *Rev. Mod. Phys.* **88**, 045006 (2016).
39. Gan, L.-Y. & Schwingenschlögl, U. Two-dimensional square ternary Cu_2MX_4 ($M = \text{Mo}, \text{W}; X = \text{S}, \text{Se}$) monolayers and nanoribbons predicted from density functional theory. *Phys. Rev. B* **89**, 125423 (2014).
40. Ma, Y. et al. Quantum spin Hall effect and topological phase transition in two-dimensional square transition-metal dichalcogenides. *Phys. Rev. B* **92**, 085427 (2015).
41. Yang, B., Zhang, X. & Zhao, M. Dirac node lines in two-dimensional Lieb lattices. *Nanoscale* **9**, 8740 (2017).
42. Mounet, N. et al. Two-dimensional materials from high-throughput computational exfoliation of experimentally known compounds. *Nat. Nanotechnol.* **13**, 246 (2018).
43. Kariyado, T. & Vishwanath, A. Flat band in twisted bilayer Bravais lattices. *Phys. Rev. Res.* **1**, 033076 (2019a).
44. Kennes, D. M., Xian, L., Claassen, M. & Rubio, A. One-dimensional flat bands in twisted bilayer germanium selenide. *Nat. Commun.* **11**, 1124 (2020).
45. de las Heras, D., Loehr, J., Loenne, M. & Fischer, T. M. Topologically protected colloidal transport above a square magnetic lattice. *N. J. Phys.* **18**, 105009 (2016).
46. Shallcross, S., Sharma, S., Kandelaki, E. & Pankratov, O. A. Electronic structure of turbostratic graphene. *Phys. Rev. B* **81**, 165105 (2010).
47. Kariyado, T. & Vishwanath, A. Flat band in twisted bilayer Bravais lattices. *Phys. Rev. Res.* **1**, 033076 (2019).

Acknowledgements

This work is funded by the Deutsche Forschungsgemeinschaft (DFG, German Research Foundation) under project number 440764520. Open Access funding partially provided by project DEAL. We thank the referees for their helpful comments.

Author contributions

N.C.X.S. carried out the calculations. N.C.X.S., T.M.F., and D.d.l.H. conceived and designed the idea and wrote the manuscript.

Funding

Open Access funding enabled and organized by Projekt DEAL.

Competing interests

The authors declare no competing interests.

Additional information

Supplementary information The online version contains supplementary material available at <https://doi.org/10.1038/s42005-022-00824-3>.

Correspondence and requests for materials should be addressed to Daniel de las Heras.

Peer review information *Communications Physics* thanks the anonymous reviewers for their contribution to the peer review of this work.

Reprints and permission information is available at <http://www.nature.com/reprints>

Publisher's note Springer Nature remains neutral with regard to jurisdictional claims in published maps and institutional affiliations.



Open Access This article is licensed under a Creative Commons Attribution 4.0 International License, which permits use, sharing, adaptation, distribution and reproduction in any medium or format, as long as you give appropriate credit to the original author(s) and the source, provide a link to the Creative Commons license, and indicate if changes were made. The images or other third party material in this article are included in the article's Creative Commons license, unless indicated otherwise in a credit line to the material. If material is not included in the article's Creative Commons license and your intended use is not permitted by statutory regulation or exceeds the permitted use, you will need to obtain permission directly from the copyright holder. To view a copy of this license, visit <http://creativecommons.org/licenses/by/4.0/>.

© The Author(s) 2022

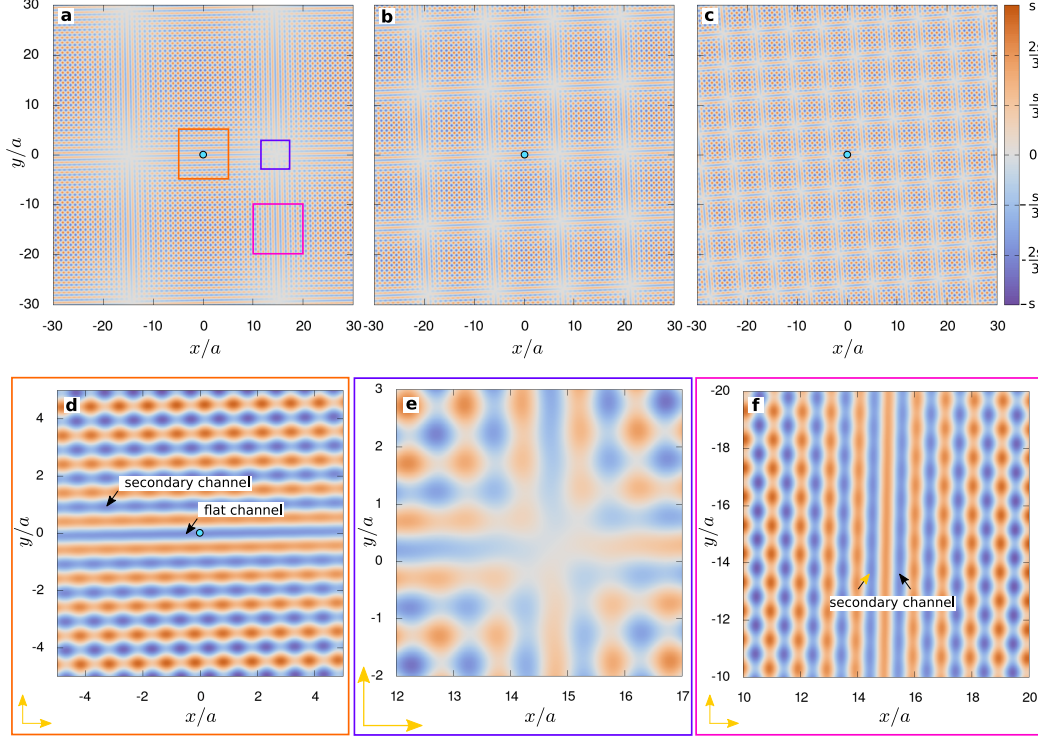
Supplementary Information: Enhanced colloidal transport in twisted magnetic patterns

Nico C. X. Stuhlmüller,¹ Thomas M. Fischer,² and Daniel de las Heras^{1,*}

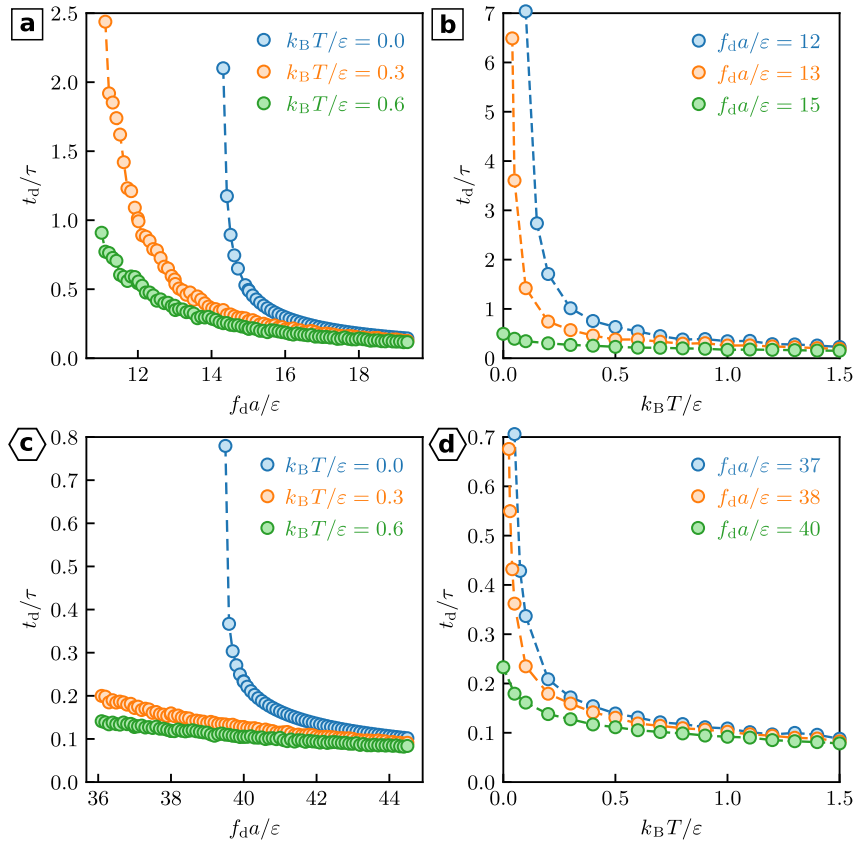
¹*Theoretische Physik II, Physikalisches Institut, Universität Bayreuth, D-95440 Bayreuth, Germany*

²*Experimentalphysik X, Physikalisches Institut, Universität Bayreuth, D-95440 Bayreuth, Germany*

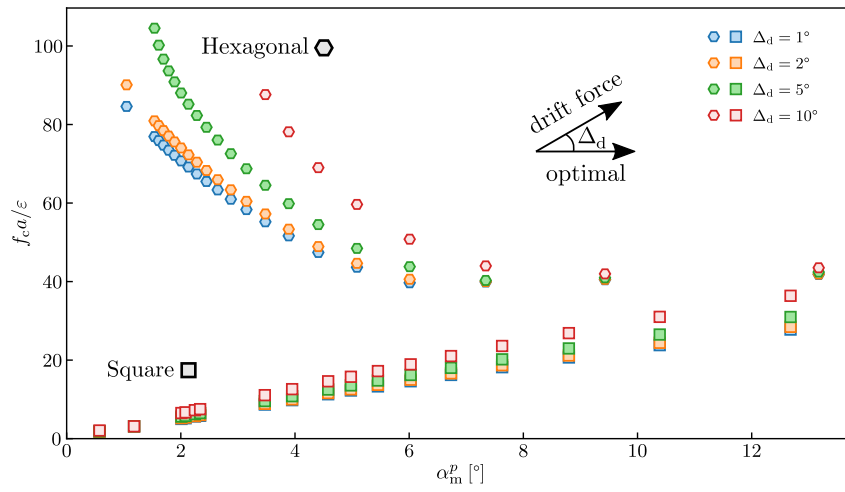
(Dated: January 20, 2022)



Supplementary Figure 1. **Twisted square patterns.** Magnetic potential, V_{mag} , (color-coded) in twisted square patterns. One pattern is twisted around the axis normal to the patterns that passes through the origin (indicated by blue circles). The magic twist angle is $\alpha_m^{\text{sq}} \approx 2.01^\circ$ in (a), $\alpha_m^{\text{sq}} \approx 4.24^\circ$ in (b), and $\alpha_m^{\text{sq}} \approx 8.80^\circ$ in (c). The untwisted pattern is shifted by $\mathbf{a}_1/2$. Panels (d), (e), and (f) are close views of selected regions for the magic angle $\alpha_m^{\text{sq}} \approx 2.01^\circ$ (panel (a)), as indicated by the color boxes. The scale factor of the potential (see colorbar) is $s/\epsilon = 60$ in (a),(b), and (c), $s/\epsilon = 40$ in (d), $s/\epsilon = 15$ in (e), and $s/\epsilon = 40$ in (f). Panel (d) is a close view of a flat channel and the adjacent secondary channels (parallel to the flat channel and at a distance a of it), as indicated. Panel (e) is a close view of a corner that joins two flat channels. Panel (f) is a close view of an edge for which the potential is maximum. Two secondary channels, parallel to the edge and at a distance $a/2$ from it, are indicated. The lattice vectors \mathbf{a}_1 and \mathbf{a}_2 of the untwisted pattern are parallel to the x - and y -axes, respectively (see yellow arrows in panels (d),(e), and (f)).



Supplementary Figure 2. **Dwelling time at the corners.** Median time that a particle needs to cross the corner of a supercell t_d as a function of the magnitude of the drift force f_d at different temperatures, as indicated, in square (a) and in hexagonal (c) patterns twisted at a magic angle. Panels (b) and (d) show the crossing time t_d as a function of the temperature for different magnitudes of the drift force f_d , as indicated, in square and hexagonal twisted patterns, respectively. The magic angle is set to $\alpha_m^{\text{sq}} \approx 6.03^\circ$ and $\alpha_m^{\text{hex}} \approx 6.01^\circ$ in square and hexagonal patterns twisted at a magic angle, respectively. The crossing time for each individual particle is calculated by initializing the particle at position $\mathbf{x}_0^{\text{sq}} \approx (3.9, 0.3)$ or $\mathbf{x}_0^{\text{hex}} \approx (2.0, 0.2)$ for the square and hexagonal twisted patterns, respectively, and then measuring the time it takes the particle to cross a circle of radius $r^{\text{sq}} = L/2$ or $r^{\text{hex}} = L/3$. Here, $L = a/(2\sin(\alpha/2))$ and the circles are centered at the origin (axis of rotation). The initial positions are those of the the last local minima in the magnetic potential before the corners of the supercell. The circles of radii r^p , $p \in \{\text{sq}, \text{hex}\}$, cut through the corner of the supercells. When a particle has crossed the aforementioned circle it accelerates away from the corner of the supercell. To estimate t_d we take the median of 1000 individual crossing times. The strongest drift forces in panels (b) and (d), represented by green circles, are above the critical drift force at zero temperature and therefore the crossing time remains finite at $T = 0$. The other two values of the magnitude of the drift forces in (b) and (d), represented by blue and orange circles, are below the critical drift force at zero temperature and hence the curves diverge at zero temperature. Dashed lines are guides for the eye.



Supplementary Figure 3. **Effect of the direction of the drift force.** Magnitude of the critical force f_c required to transport particles at $T = 0$ as a function of the magic angle α_m^p in twisted square (square symbols) and hexagonal (hexagonal symbols) patterns for different directions of the drift force Δ_d , as indicated by the color of the symbols. The direction of the drift force is given by Δ_d which is the angle (in degrees) between the applied drift force and the optimal drift force. The optimal drift force points along the average direction between two consecutive flat channels.

SUPPLEMENTARY NOTE 1

We show here that for any non-magic angle the potential along the flat channels is at some point be unfavorable for the colloidal transport. To this end, we describe the local properties of patterns twisted at an arbitrary angle using the global properties of patterns twisted at angles for which the resulting potential is periodic.

Laboratory and local reference frames. Let \mathbf{s}_1 and \mathbf{s}_2 designate the shift vectors of patterns 1 and 2, respectively, and let \mathbf{f} denote the fixed point of the rotation. That is, the patterns are rotated relative to each other a total twist angle α about an axis normal to the patterns that passes through \mathbf{f} . In the main paper, we fix a laboratory reference frame in which $\mathbf{f} = \mathbf{0}$ (origin) and the shift vectors are $\mathbf{s}_1 = \mathbf{a}_1/2$ and $\mathbf{s}_2 = \mathbf{0}$. For our purpose here, we use also a local reference frame in which the fixed point is at the desired position $\mathbf{f} = \mathbf{r}$ and the shift vectors are hence position-dependent $\mathbf{s}_1(\mathbf{r})$, $\mathbf{s}_2(\mathbf{r})$. Shifting the patterns by the shift vectors in the local reference frame and twisting around the local fixed point generates the same potential as if we shift the patterns by the laboratory shift vectors and twist around the origin. Locations \mathbf{r} and \mathbf{r}' with similar shift vectors in the local reference frame, i.e at positions \mathbf{r} and \mathbf{r}' , share a similar magnetic potential.

Periodic potentials and magic angles. The potential generated by two twisted patterns is periodic for any values of \mathbf{f} , \mathbf{s}_1 , and \mathbf{s}_2 provided that the twist angle is [1, 2]

$$\alpha_{\text{per}}^{(n)}(q/p) = 2 \arctan \left(\frac{q/p \sin(\pi/n)}{1 + q/p \cos(\pi/n)} \right), \quad (\text{S1})$$

where p and q are co-prime integers, $n = 2$ for square patterns, and $n = 3$ for hexagonal patterns. Although the resulting potential is periodic for any pair of co-primes p and q , the magic angles are only those for which $q/p = 1/(nk + 1)$ with $k \in \mathbb{N}$ (see Methods). Hence $\alpha_{\text{m}}^p = \alpha_{\text{per}}^{(n)}(1/(nk + 1))$. For these values, the unit cell of the twisted patterns is the smallest one in terms of supercells: The unit cell of patterns twisted at magic angles is twice the size of the supercells in square patterns and of the same size in hexagonal patterns (see Fig. 2 of the main paper). For any other co-primes p and q in Eq. (S1) the potential is also periodic but the unit cell of the twisted patterns contains more (slightly different) supercells and, as we see below, the potential along the flat channels is at some point unfavorable for the transport.

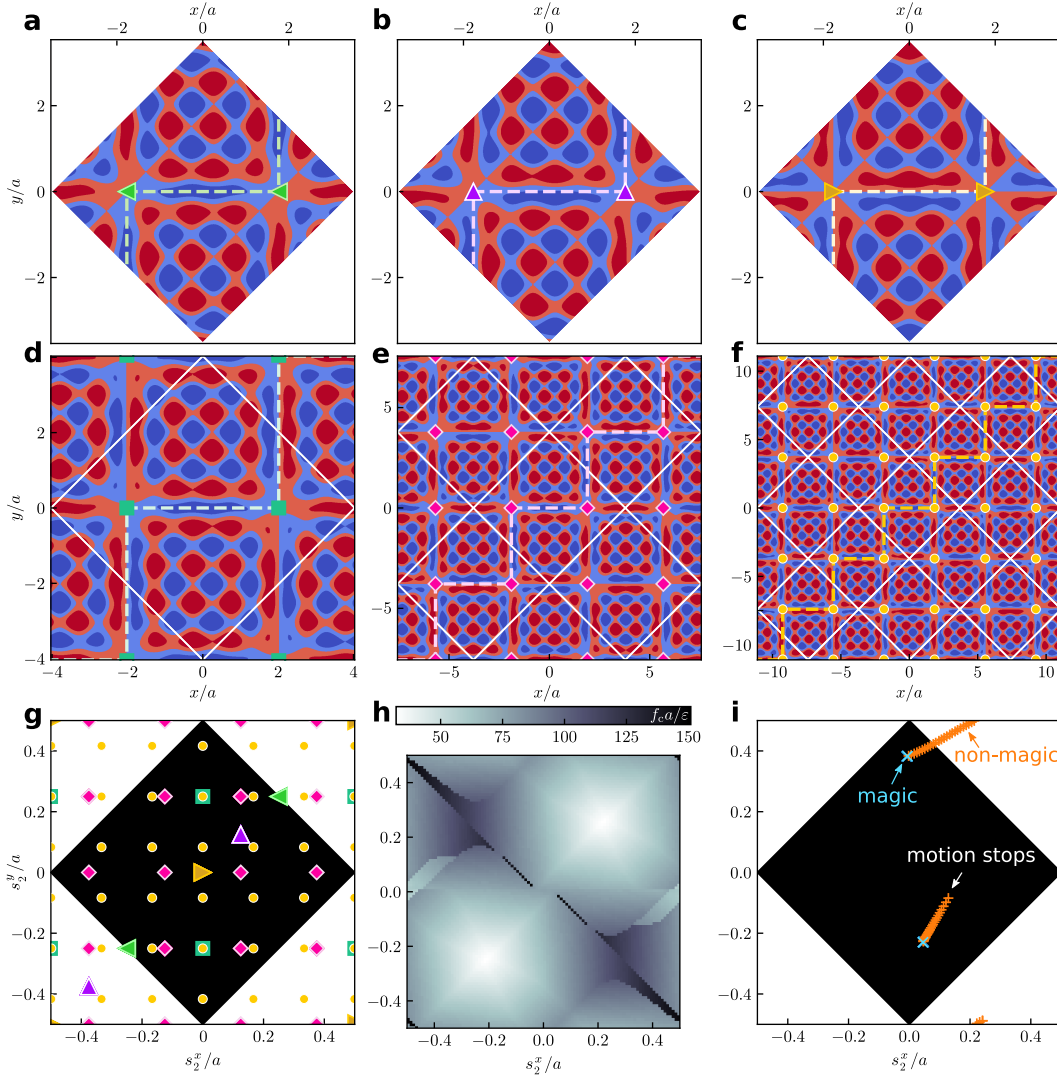
An arbitrary twist angle α can be approximated by an angle $\alpha_{\text{per}}^{(n)}(q/p)$ using sufficiently large integers p and q . Hence, understanding transport in the periodic potentials given by twist angles $\alpha_{\text{per}}^{(n)}(q/p)$ is enough to understand the transport for arbitrary twist angles.

Critical force at the corners of the supercells. In Supplementary Fig. 4 panels (a), (b), and (c) we show the magnetic potential in one unit cell of squared patterns twisted at magic angle $\alpha_{\text{m}}^{\text{sq}} = \alpha_{\text{per}}^{(2)}(1/7) \approx 16.260^\circ$ with fixed point at the origin ($\mathbf{f} = \mathbf{0}$) and for different shift vectors: $\mathbf{s}_1 = \mathbf{a}_1/2$ and $\mathbf{s}_2 = \mathbf{0}$ in panel (a), $\mathbf{s}_1 = 0.125(3\mathbf{a}_1 - \mathbf{a}_2)$ and $\mathbf{s}_2 = -0.125(\mathbf{a}_1 + \mathbf{a}_2)$ in panel (b), $\mathbf{s}_1 = 0.25(\mathbf{a}_1 - \mathbf{a}_2)$ and $\mathbf{s}_2 = -0.25(\mathbf{a}_1 + \mathbf{a}_2)$ in panel (c). We highlight with symbols (dashed lines) the position of the corners (edges) of the supercells.

Only one shift vector is enough to characterize specific locations of the pattern, such as the corners of the supercells, since there is a constraint that links both shift vectors at that specific location. For example, at the corners of the supercells $\mathbf{r} = \mathbf{r}_c$, the interference between both patterns is destructive and we get $\mathbf{s}_1(\mathbf{r}_c) - \mathbf{s}_2(\mathbf{r}_c) = \pm(\mathbf{a}_1 + \mathbf{a}_2)/n$. This equation for the position of the corners leads to a square (hexagonal) lattice that defines the supercells of the twisted pattern for any twist angle, independently of whether the angle is magic or not.

Knowing $\mathbf{s}_1(\mathbf{r}_c)$ in the local reference frame at the position of the corner fully determines $\mathbf{s}_2(\mathbf{r}_c)$ at the same position. Also, we can use the periodicity of the single patterns to fold the shift vectors into the unit cell of the single patterns. In panel (g) of Supplementary Figure 4 we indicate with the same symbols as in panels (a,b,c) the coordinates of the shift vector $\mathbf{s}_2(\mathbf{r}_c)$ at the corners of the supercells. Note that at magic angles the unit cell contains two supercells and hence only two sets of shift vectors at the corners exist [there are two triangles of each color in panel (g)]. In panel (h), we plot a color map of the critical force required to cross a supercell in the plane of the components of the shift vector $\mathbf{s}_2(\mathbf{r}_c)$ at the corners of the crossed supercell. In both panel (g) and panel (h) we have folded the shift vector $\mathbf{s}_2(\mathbf{r}_c)$ into the unit cell of a single pattern. The critical force has two global minima corresponding to the corners of patterns twisted at magic angles and shifted by half a unit vector [panel (a) and green triangles]. Again, these are the patterns discussed in the main text. For any other corner the critical force required to cross it increases.

Next, we consider patterns twisted at angles close to a magic angle and for which the potential is also periodic. We show in Supplementary Figure 4(d,e,f) the magnetic potential in one unit cell for three of such patterns. The twist



Supplementary Figure 4. **Transport at non-magic angles.** Magnetic potential in one unit cell of square patterns twisted at the magic angle $\alpha_m^{\text{sq}} = \alpha_{\text{per}}^{(2)}(1/7)$ around $\mathbf{f} = \mathbf{0}$ and with shift vectors $\mathbf{s}_1 = \mathbf{a}_1/2$ and $\mathbf{s}_2 = \mathbf{0}$ in panel (a), $\mathbf{s}_1 = 0.125(3\mathbf{a}_1 - \mathbf{a}_2)$ and $\mathbf{s}_2 = -0.125(\mathbf{a}_1 + \mathbf{a}_2)$ in panel (b), $\mathbf{s}_1 = 0.25(\mathbf{a}_1 - \mathbf{a}_2)$ and $\mathbf{s}_2 = -0.25(\mathbf{a}_1 + \mathbf{a}_2)$ in panel (c). Panel (a) is the same type of twisted patterns as those discussed in the main text. The color map has been saturated to better visualize the regions of positive (red) and negative (blue) magnetic potential. The colored triangles indicate the position of the corners of the supercells. Panels (d), (e), and (f) show the magnetic potential in one unit cell of square patterns twisted around $\mathbf{f} = \mathbf{0}$ with shift vectors $\mathbf{s}_1 = \mathbf{a}_1/2$ and $\mathbf{s}_2 = \mathbf{0}$ [like in panel (a)]. The twist angles generate a non-magic but periodic potential: $\alpha_{\text{per}}^{(n)}(q/p)$ with $q/p = 1/8$ in (d), $q/p = 2/15$ in (e), and $q/p = 3/22$ in (f). One unit cell contains 4 (d), 8 (e), and 32 (f) slightly different supercells (for visualization purposes, we draw with white lines pseudo unit cells, each containing 2 supercells). The symbols indicate the position of the corners of the supercells. The dashed lines illustrate the flat channel that would transport a particle located at the origin. (g) Components of the shift vector \mathbf{s}_2 at the corners of the supercells for the patterns shown in panels (a) to (f). Triangles correspond to patterns twisted at a magic angle (a,b,c) and other symbols represent patterns twisted at non-magic angles (d,e,f). The shift vector has been folded into the unit cell of a single square pattern. (h) Diagram of the critical force (color map) required to pass a supercell in the plane of the components of the shift vector \mathbf{s}_2 . Data calculated with computer simulations in squared patterns twisted at $\alpha_m^{\text{sq}} = \alpha_{\text{per}}^{(2)}(1/7)$. (i) Shift vectors (in the plane of the components of \mathbf{s}_2) of the trajectory points closest to the corners of supercells in square patterns twisted at magic angle $\alpha_m^{\text{sq}} = \alpha_{\text{per}}^{(2)}(1/19) \approx 6.026^\circ$ (blue crosses) and at non-magic angle $\alpha_{\text{per}}^{(2)}(131457/2500000) \approx 6.020^\circ$ (orange crosses). In the non-magic case the motion stops after 55 corners have been crossed. Data obtained for $T = 0$ and $f_{\text{DA}}/\epsilon = 25$.

angles are given by Eq. (S1) with $q/p = 1/8 = 0.125$ in (d), $q/p = 2/15 \approx 0.133$ in (e), and $q/p = 3/22 \approx 0.136$ in (f). That is, in the three cases the angle is close to the magic twist angle $q/p = 1/7$ discussed above. The supercells are therefore of approximately the same size as in the magic case, e.g. panel (a), but since the angle is non-magic the unit cell contains several supercells (note the different scales used in the panels of Supplementary Figure 4). There are four (d), sixteen (e), and thirty two (f) supercells per each unit cell. The supercells slightly differ from each other, and therefore their corresponding shift vectors at the corners, shown in (h), are also different. Clearly, the shift vectors at the corners spread along the whole space instead of being concentrated around the region of small critical force (even though in the three cases $\mathbf{f} = \mathbf{0}$ and the shift vectors are $\mathbf{s}_1 = \mathbf{a}_1/2$ and $\mathbf{s}_2 = \mathbf{0}$, i.e. the shift vectors and the fixed point are like in the twisted patterns discussed in the main text). The higher the number of supercells per unit cell [i.e. the larger value of q in Eq. (S1)] the more spread the shift vectors are. This illustrates that transport in patterns twisted at magic angles is much more favorable than transport in periodic patterns twisted at angles that are non-magic.

Finally, to approximate a generic, non-periodic, twist angle [i.e. $\alpha \neq \alpha_{\text{per}}^{(n)}(q/p)$] with arbitrary precision we need large values of p and q in Eq. (S1). However, increasing the value of q/p also increases the spread of the shift vectors at the corners of the supercells, which means that larger drift forces are required to pass all the supercells of a unit cell. To illustrate this phenomenon, we simulate the trajectories of particles moving in twisted patterns for which $q/p = 131457/2500000 \approx 0.05258$ and hence $\alpha_{\text{per}}^{(2)}(131457/2500000) \approx 6.020^\circ$. This value of q/p is very close to the magic case $q/p = 1/19 \approx 0.05263$, which we also simulate. For the magic case, $\alpha_{\text{m}}^{\text{sq}} = \alpha_{\text{per}}^{(2)}(1/19) \approx 6.026^\circ$. In the simulations, the particle trajectories never pass exactly through the corners of the supercells but close to them. For this reason, we plot in panel (i) of Supplementary Figure 4 the components of the shift vector $\mathbf{s}_2(\mathbf{r})$ corresponding to the trajectory points that are closest to the corners of the supercells for both the magic case (blue crosses) and the non-magic case (orange crosses). For the magic case we found only two points that correspond to the position of the minimal critical force (note again that the used shift vectors are not those at the corners but the closest ones along the trajectories). In contrast, in the non-magic case the shift vectors deviate more and more from the initial position until the particle gets stuck and the motion stops. Note that the motion stops when the shift vectors approach the diagonal along which the critical force to cross the supercells is large, see panel (h). If we want to sustain transport indefinitely, we would need to use a drift force that is able to cross the most unfavorable supercell. Similar phenomena (not shown) occurs for hexagonal twisted patterns.

SUPPLEMENTARY REFERENCES

* delasheras.daniel@gmail.com; www.danieldelasheras.com

- [1] S. Shallcross, S. Sharma, E. Kandelaki, and O. A. Pankratov, Electronic structure of turbostratic graphene, *Phys. Rev. B* **81**, 165105 (2010).
- [2] T. Kariyado and A. Vishwanath, Flat band in twisted bilayer Bravais lattices, *Phys. Rev. Res.* **1**, 033076 (2019).

2.4 Colloidal transport in twisted lattices of optical tweezers

In this publication we investigate whether enhanced colloidal transport [1] is also possible in a significantly different system, comprised of twisted arrays of optical tweezers. Twisted arrays of optical tweezers are experimentally doable. For example as arrays of optical tweezers have been used to sort particles according to their size [80, 81]. Optical tweezers are widely used, as alluded to in section 1.4.3, so this publication is meant to present to a large community the phenomenology of high mobility in patterns twisted to magic angles. It also makes the phenomenology occurring in the magnetic system [1] more widely accessible, as it is easier to produce an array of optical tweezers as compared to the twisted magnetic patterns.

We start by discussing the differences between the optical potential in which the particles move and the magnetic potential [1]. The optical potential has an additional parameter A , which controls the steepness of the tweezers. We then determine the critical force for several values of A in hexagonal and square patterns for a wide range of magic angles. In the square systems, the critical force follows the same trend as in the magnetic system: Decreasing the magic angle also decreases the drift force required for transport, extrapolating to vanishing drift force for vanishing magic angle. This is true for all values of A investigated. However, at $A = 5$ plateaus and steps start to form in the drift force required for macroscopic transport. Here the critical drift force roughly stays the same for some magic angles and then rapidly decreases when the magic angle is decreased.

In the hexagonal systems we also mostly recover the behavior of the critical drift force [1]. However, at $A = 5$ the critical drift force, does no longer increase for increasing magic angle above $\alpha_m > 6^\circ$, instead it decreases. In the limit of $A \rightarrow 0$ the optical potential converges to the magnetic potential, so we expect strong similarities between the optical and the magnetic system for small A .

Finally we investigate how far particles travel in the optical lattice as a function of the twist angle, including non-magic angles. We here find very sharp peaks in the traveled distance, at magic angles. At non magic angles the total distance that the particles travel is extremely small as compared to the magic cases.

Publication 2

Colloidal transport in twisted lattices of optical tweezers

Phys. Rev. E **106**, 034601 (2022)

Nico C. X. Stuhlmüller¹, Thomas M. Fischer² &
Daniel de las Heras¹

¹Theoretical Physics II, Department of Physics, University of Bayreuth, 95447 Bayreuth, Germany


²Experimental Physics X, Department of Physics, University of Bayreuth, 95447 Bayreuth, Germany.

Colloidal transport in twisted lattices of optical tweezers

Nico C. X. Stuhlmüller¹, Thomas M. Fischer², and Daniel de las Heras^{1,*}

¹*Theoretische Physik II, Physikalisches Institut, Universität Bayreuth, D-95440 Bayreuth, Germany*

²*Experimentalphysik X, Physikalisches Institut, Universität Bayreuth, D-95440 Bayreuth, Germany*

 (Received 23 May 2022; accepted 9 August 2022; published 1 September 2022)

We simulate the transport of colloidal particles driven by a static and homogeneous drift force, and subject to the optical potential created by two lattices of optical tweezers. The lattices of optical tweezers are parallel to each other, shifted, and rotated by a twist angle. Due to a negative interference between the potential of the two lattices, flat channels appear in the total optical potential. At specific twist angles, known as magic angles, the flat channels percolate the entire system and the colloidal particles can then be transported using a weak external drift force. We characterize the transport in both square and hexagonal lattices of twisted optical tweezers.

DOI: [10.1103/PhysRevE.106.034601](https://doi.org/10.1103/PhysRevE.106.034601)

I. INTRODUCTION

Optical tweezers [1] use optical gradient forces to manipulate micrometer-sized colloidal particles. Lattices of optical tweezers arranged in arbitrary patterns can be created, e.g., using diffractive optical elements [2], combining beam splitters and refractive optics [3], by means of computer-generated holograms [4], and even rapidly moving a single beam among different locations such that the desired pattern emerges as a result of a time-averaged optical potential [5–7].

Periodic lattices of optical tweezers in combination with a driving force are widely used to sort particles [8–11]. Using a three-dimensional periodic optical lattice, MacDonald *et al.* [8] were able to sort particles exploiting the differences in the interactions between the particles and the optical lattice. Also, as shown by Lacasta *et al.* [10], particles moving in a periodic optical potential can behave differently according to their size or particle index of refraction.

Motivated by the emerging field of twistrionics [12], we adapt here the setup of Lacasta *et al.* [10] to model two sets of periodic lattices of optical tweezers that are parallel to each other and are also twisted by a given twist angle. Using computer simulations we study the transport of colloidal particles subject to the combined potential of both lattices and driven by a uniform and time-independent drift force. At specific twist angles, known as magic angles, the transport is more efficient due to the formation of flat channels in the combined optical potential of both lattices. Emergent phenomena in twisted bilayers, such as the occurrence of superconductivity in twisted graphene [13], has been observed in fundamentally different physical systems, including the appearance of quasi-one-dimensional channels along which Abrikosov vortices can freely flow in twisted pinning lattices [14], the formation of flat bands in twisted acoustic metamaterials [15], and enhanced colloidal transport in twisted magnetic patterns [16]. In contrast to single magnetic patterns, the magnetic potential of two twisted patterns develops flat channels along which it is possible to transport a magnetic colloidal particle applying

a weak drift force [16]. The flat channels percolate the entire system only for specific values of the twist angle. We show here with computer simulations that similar phenomena arise also in a fundamentally different system made of twisted lattices of optical tweezers.

II. MODEL AND RESULTS

A schematic of the model is shown in Fig. 1. The colloidal particles, which are driven by a drift force, are restricted to move in the middle plane between two parallel lattices of optical tweezers. We consider two periodic lattices of optical tweezers with square and hexagonal symmetries. The lattices are twisted by an angle α and shifted by half a unit lattice vector. A destructive interference between the optical potential generated by both lattices results in the formation of channels along which the potential is almost flat. Using a weak drift force it is then possible to transport the colloidal particles along the flat channels. At specific twist angles, known as magic angles, the flat channels percolate the entire system allowing transport over arbitrarily long distances.

A. Optical potential

Following Lacasta *et al.* [10], we approximate the optical potential at position \mathbf{r} by

$$V(\mathbf{r}) = -\frac{V_0}{1 + e^{-A[g(\mathbf{r})-1]}}, \quad (1)$$

with positive constants A and V_0 that control the steepness and the depth of the optical potential, respectively. The spatial modulation and the interference between the two arrays of optical tweezers is controlled by the function

$$g(\mathbf{r}) = \sum_{i=1}^N \left\{ \cos \left[\mathbf{q}_i \cdot \left(\mathbf{R}_{-\alpha/2} \cdot \mathbf{r} - \frac{\mathbf{a}_1}{2} \right) \right] + \cos(\mathbf{q}_i \cdot \mathbf{R}_{\alpha/2} \cdot \mathbf{r}) \right\}, \quad (2)$$

where each of the two terms in the summation represents one of the lattices of optical tweezers.

*www.danieldelasher.com; delasher.daniel@gmail.com

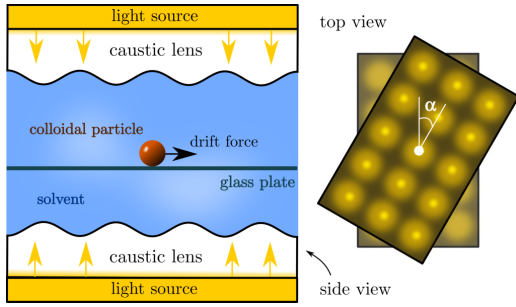


FIG. 1. Schematic of the model: side (left) and top (right) views. A colloidal particle immersed in a solvent is located above a glass plate in the middle plane between two lattices of optical tweezers. The lattices are identical but are rotated by an angle α around an axis normal to them. The interference between the optical potential of both lattices creates an anisotropic potential landscape for the colloidal particles.

The lattices are shifted relative to each other by half of the first lattice vector of the single lattice prior to being rotated, $\mathbf{a}_1/2$, which we set along the x axis, i.e., $\mathbf{a}_1 = a\hat{\mathbf{e}}_x$, with a the magnitude of all the lattice vectors. The relative shift by half of a lattice vector maximizes the destructive interference between the two lattices at the flat channels. The matrix \mathbf{R}_θ is a rotation matrix by an angle θ around the axis normal to the lattice that passes through the origin. In Eq. (2) we rotate each lattice by an angle $\alpha/2$ in opposite directions such that

the total rotation between the lattices is the twist angle α . The reciprocal lattice vectors \mathbf{q}_i are given by

$$\mathbf{q}_i = q \begin{pmatrix} \sin(\pi i/N) \\ \cos(\pi i/N) \end{pmatrix}, \quad (3)$$

where in the square lattice $N = 2$ and $q = 2\pi/a$, and in the hexagonal lattice $N = 3$ and $q = 2\pi/[a \sin(\pi/3)]$.

B. Magic angles

The total optical potential that results from the interference between both lattices is a moiré pattern. For specific twist angles the resulting potential is periodic. Among those angles for which the potential is periodic, we find the so-known magic angles, with particularly small lattice constants, given by [16]

$$\alpha_m(k, N) = 2 \arctan \left(\frac{\frac{1}{Nk+1} \sin(\frac{\pi}{N})}{1 + \frac{1}{Nk+1} \cos(\frac{\pi}{N})} \right), \quad (4)$$

where k is a natural number and again $N = 2$ for the square lattices and $N = 3$ for the hexagonal lattices.

The optical potential of lattices twisted at magic angles [see Figs. 2(a) and 2(b)] develops super unit cells of length given by approximately $a/[2 \sin(\alpha_m/2)]$. That is, the super unit cells grow by decreasing the magic angle. The super unit cells contain regions where the interference between the lattices is positive and hence the potential resembles that created by a single lattice, shown also as insets in Figs. 2(a) and 2(b). In addition, the super unit cells also contain regions at which the interference is mostly destructive. There, the potential develops flat channels along which transport is possible using

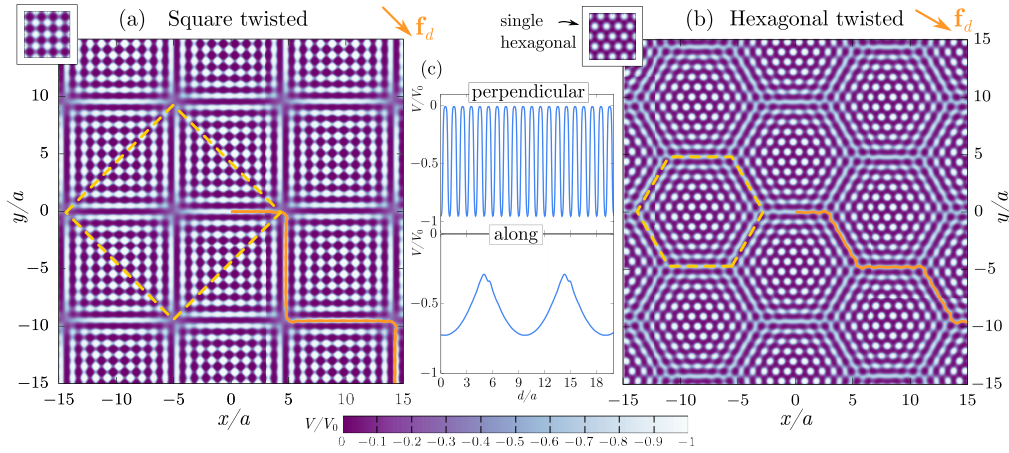


FIG. 2. Optical potential ($A = 1$) generated by two square (a) and two hexagonal (b) twisted lattices of optical tweezers twisted at magic angles: $\alpha_m \approx 6.026^\circ$ in (a) and $\alpha_m \approx 6.009^\circ$ in (b). A super unit cell of the moiré pattern is highlighted (yellow dashed line). A drift force \mathbf{f}_d points in the direction of two consecutive flat channels (orange arrows) and drives the motion of the particles. Characteristic particle trajectories are depicted in orange. The amplitude of the external force is set to $f_d = 0.4V_0/a$ (a) and to $f_d = 0.8V_0/a$ (b). The optical potential of single square and hexagonal lattices is shown in the top left-hand corner of the panels. Cuts of the potential (square lattices) perpendicular and along the flat channel that passes through the origin are depicted in (c) as a function of the distance traveled by a particle initially at the origin. The force required to travel along the channel (negative gradient of the potential) is significantly smaller than the force required to travel perpendicular to the channel.

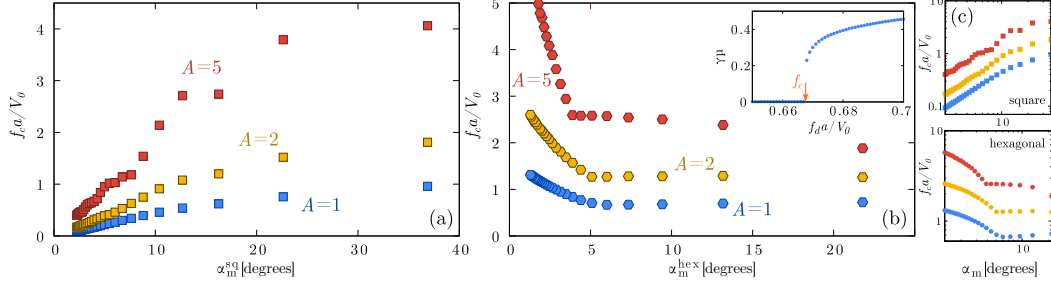


FIG. 3. Critical force in twisted square (a) and hexagonal (b) lattices as a function of the magic angle for different values of A . (c) shows the corresponding log-log plots for both types of lattices, as indicated. A linear fit on the log-log data for small magic angles returns a slope $s \approx 1$ in square lattices. In hexagonal lattices, $s \approx 1/3$ for both $A = 1$ and $A = 2$, and $s \approx 1/2$ for $A = 5$. The inset in (b) depicts the mobility μ vs the magnitude of the drift force f_d for the optical potential depicted in Fig. 2(a). The orange arrow indicates the value of the critical force f_c .

a weak drift force. The flat channels cross the super unit cell in square twisted lattices [Fig. 2(a)] and are located at the edges of the super unit cells in hexagonal twisted lattices [Fig. 2(b)]. We show in Fig. 2(c) a cut of the optical potential in the directions perpendicular to a flat channel and also along the flat channel, as indicated. The force required to travel along the flat channel (given by the negative gradient of the optical potential) is significantly weaker than that required to travel perpendicular to the flat channel. Increasing the parameter A makes the potential flatter along the central region of a flat channel. However, it also makes the potential steeper near the intersections between two flat channels. At the magic angles the flat channels percolate the entire system.

C. Computer simulations

We neglect inertial effects and therefore use overdamped dynamics to simulate the motion of a single colloidal particle. At high laser intensity the Brownian forces can be neglected as compared to the optical forces, we therefore set the temperature to zero such that Brownian motion does not hinder the phenomenology. The equation of motion for a single particle reads

$$\gamma \dot{\mathbf{r}} = -\nabla V(\mathbf{r}) + \mathbf{f}_d, \quad (5)$$

where γ is the friction coefficient against the implicit solvent, $\dot{\mathbf{r}}$ indicates the time derivative of the position vector, and \mathbf{f}_d is a homogeneous external drift force. The magnitude of a lattice vector a , the energy parameter of the optical potential V_0 , and the friction coefficient γ define our system of units. The intrinsic timescale is therefore $\tau = \gamma a^2 / V_0$. We integrate the equation of motion using an adaptive Heun-Euler scheme [17], setting the relative allowed error per time step to 10^{-2} and the absolute allowed error in the positions to $10^{-4}a$.

D. Drift force

To drive the colloidal motion we use a drift force \mathbf{f}_d pointing along the bisector of the directions of two flat channels

[see Figs. 2(a) and 2(b)]. Hence,

$$\mathbf{f}_d = f_d \begin{pmatrix} \cos \alpha_d \\ \sin \alpha_d \end{pmatrix}, \quad (6)$$

where the angle is $\alpha_d(k) = (-1)^k \pi/4$ in square lattices and $\alpha_d(k) = (-1)^k \pi/6$ in hexagonal lattices, and the index $k \in \mathbb{N}$ is the same as for the magic angles in Eq. (4). The prefactor $(-1)^k$ alternates the direction of the drift force between the first and the fourth quadrants, reflecting the fact that the flat channels that support transport alternate from one magic angle to the next one.

Figures 3(a) and 3(b) show the magnitude of the critical drift force f_c required to transport colloidal particles along the flat channels; log-log plots are shown in Fig. 3(c). To calculate f_c we measure in the simulations the colloidal mobility μ under the influence of the drift force,

$$\mu = \frac{|\Delta \mathbf{r}(t_f)|}{t_f f_d}, \quad (7)$$

where $\Delta \mathbf{r}(t_f)$ is the distance traveled by a particle during a total time $t_f = 3000\tau$ in twisted square lattices, and $t_f = 1000\tau$ in twisted hexagonal lattices. The colloidal mobility vanishes for weak drift forces, increases rapidly at the critical drift force f_c , and it saturates for strong drift forces [see an example in the inset of Fig. 3(b)].

In square lattices, the critical force at which transport along the channels is activated decreases monotonically by decreasing the magic angle [see Fig. 3(a)]. For small magic angles, the critical force scales linearly with the magic angle [see Fig. 3(c)]. In hexagonal lattices [Fig. 3(b)], the critical force presents two distinct regimes. First, for small magic angles, there is a rapid decrease of f_c by increasing the magic angle. In the second regime, depending on the steepness of the potential, the critical force either slightly increases [e.g., $A = 1$ in Fig. 3(b)] or it slightly decreases [e.g., $A = 5$ in Fig. 3(b)]. For both square and hexagonal lattices, increasing the steepness of the potential A also increases the magnitude of the critical drift force. Increasing A makes the potential flatter along the channels, but it also increases the steepness of the potential at the intersection between two flat channels

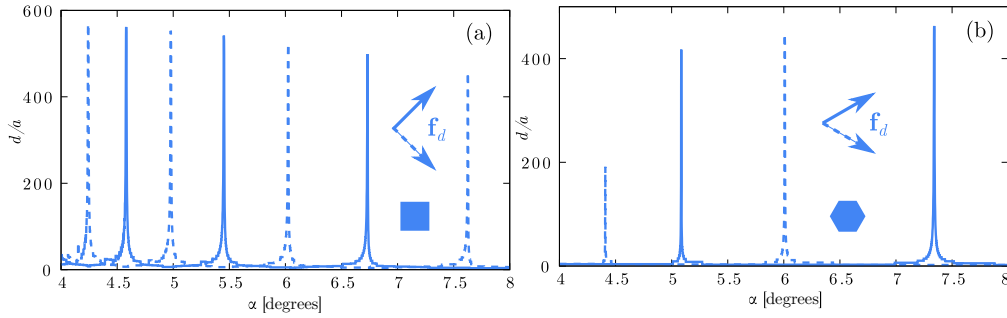


FIG. 4. Distance traveled by a particle originally at the origin in twisted square (a) and hexagonal (b) lattices ($A = 1$) as a function of the angle. In (a), the drift force $f_d = 0.4V_0/a$ acts for a total time $t = 3000$. The arrows indicate the direction of the drift force, rotated 45° (solid line) or -45° (dashed line) with respect to the direction of the first lattice vector. In (b), $f_d = 0.8V_0/a$, $t = 1000\tau$, and the drift force is rotated 30° (solid line) or -30° (dashed line) with respect to the direction of the first lattice vector.

which results in higher values of the magnitude of the critical force.

In Figs. 4(a) and 4(b) we represent the distance traveled by a particle, d , as a function of the twist angle for both square and hexagonal lattices, respectively. The particle is at time zero located at the axis of rotation of both lattices (i.e., in the middle of a flat channel). The motion is driven by a drift force acting for a total time 3000τ (1000τ) in square (hexagonal) lattices, and whose magnitude is larger than the critical force required to move particles at any of the magic angles that occur in the represented range of twist angles. For each lattice, we plot two curves, corresponding to drift forces that according to Eq. (6) point either in the first or in the fourth quadrant. The curves clearly show that the edges that support transport alternate from one magic angle to the next one. The distance traveled by the particles presents sharp peaks at the magic angles and hence even a small deviation from the magic angle has a marked effect on the transport. In square lattices the value of d at the magic angles decreases by increasing the magic angle since the critical force increases with the magic angle [see Fig. 3(a)], and we keep the magnitude of the drift force constant. The opposite behavior is observed in hexagonal lattices for the range of angles shown in Fig. 4(b). That is, d at the magic angles increases by increasing the magic angle. For the range of angles shown in Fig. 4(b), the critical drift force in hexagonal lattices decreases by increasing the magic angle, which explains the observed traveled distance at the magic angles.

III. CONCLUSIONS

Despite being substantially different systems, the colloidal transport in twisted optical lattices is quite similar to the transport in twisted magnetic patterns [16]. There, magnetic colloidal particles are located in the middle plane between two periodic magnetic patterns that are parallel to each other and are twisted by a given angle. A uniform external magnetic field \mathbf{H}_{ext} normal to the patterns couples to the field created by both patterns \mathbf{H}_p . The total magnetic potential is then dominated by the cross term $V_{\text{mag}} \propto \mathbf{H}_{\text{ext}} \cdot \mathbf{H}_p$. Both the total magnetic potential in twisted patterns and the optical poten-

tial in twisted lattices of optical tweezers [Eq. (1)] coincide only in the limit $A \rightarrow 0$. Even though we have stayed away from that limit here, the transport in both systems shares similar characteristics, demonstrating the robustness of the phenomena.

The setup described here with optical lattices offers additional flexibility with respect to that in magnetic patterns. First, the steepness of the potential of single optical lattices, controlled here by the parameter A , can be adjusted experimentally by varying the width of the tweezers. Moreover, in contrast to magnetic patterns, optical tweezers are a standard experimental technique which is widely available and it can be used with nonmagnetic colloidal particles.

We have modeled the individual optical traps by isotropic potentials. Experimentally, it is possible to control the shape of the optical trap [18], and a certain degree of anisotropy is almost unavoidable. Above a certain threshold, the anisotropy of the optical trap can have an effect on, e.g., microrheology measurements [18], and might also alter the structure of the flat channels shown here. Controlling the anisotropy of the traps (e.g., the length-to-width aspect ratio and the direction of an elliptical trap) offers another degree of freedom to modify the colloidal transport.

Several types of external forces are available experimentally to drive the motion [19]. These include, among others, electric and magnetic fields, pressure gradients, and the gravitational field of Earth in the case of micron-sized colloidal particles with a substantial contrast between the bare and the solvent mass densities.

There exist other twist angles for which the combined potential of the two lattices is also periodic [16]. However, for those angles, the direction along which transport is possible along the flat channels changes inside the super unit cell. Hence, stronger drift forces are required to cause macroscopic transport.

We have focused here on the dilute regime where interparticle interactions do not play any role. Interesting collective effects appear in many-body particle systems driven on periodic landscapes, including structural transitions and directional locking [20–22]. It would be also interesting to study collective effects in the dynamics of many-body particles in

twisted lattices such as the superadiabatic forces [23,24] and the occurrence of solitons [25].

Another interesting extension of the present work is the characterization of the transport in twisted three-dimensional optical lattices. Moreover, using periodic two-dimensional magnetic patterns together with a homogeneous magnetic field, one can topologically transport magnetic colloidal particles placed above the patterns [26–28]. There exist special modulation loops of the orientation of the external field such that once the loop returns to its initial position the particle has been transported by one unit cell above the pattern. The

colloidal motion is topologically protected and takes place in a plane due to the two-dimensional nature of the magnetic patterns. Optical potentials could be used to extend the study of topologically protected colloidal transport to three-dimensional systems.

ACKNOWLEDGMENTS

This work is funded by the Deutsche Forschungsgemeinschaft (DFG, German Research Foundation) under Project No. 440764520.

-
- [1] A. Ashkin, J. M. Dziedzic, J. E. Bjorkholm, and S. Chu, Observation of a single-beam gradient force optical trap for dielectric particles, *Opt. Lett.* **11**, 288 (1986).
- [2] E. R. Dufresne and D. G. Grier, Optical tweezer arrays and optical substrates created with diffractive optics, *Rev. Sci. Instrum.* **69**, 1974 (1998).
- [3] E. Fällman and O. Axner, Design for fully steerable dual-trap optical tweezers, *Appl. Opt.* **36**, 2107 (1997).
- [4] J. Liesener, M. Reicherter, T. Haist, and H. Tiziani, Multifunctional optical tweezers using computer-generated holograms, *Opt. Commun.* **185**, 77 (2000).
- [5] K. Sasaki, M. Koshioka, H. Misawa, N. Kitamura, and H. Masuhara, Pattern formation and flow control of fine particles by laser-scanning micromanipulation, *Opt. Lett.* **16**, 1463 (1991).
- [6] K. Visscher, S. Gross, and S. Block, Construction of multiple-beam optical traps with nanometer-resolution position sensing, *IEEE J. Sel. Top. Quantum Electron.* **2**, 1066 (1996).
- [7] D. G. Grier, A revolution in optical manipulation, *Nature (London)* **424**, 810 (2003).
- [8] M. P. MacDonald, G. C. Spalding, and K. Dholakia, Microfluidic sorting in an optical lattice, *Nature (London)* **426**, 421 (2003).
- [9] P. T. Korda, M. B. Taylor, and D. G. Grier, Kinetically Locked-In Colloidal Transport in an Array of Optical Tweezers, *Phys. Rev. Lett.* **89**, 128301 (2002).
- [10] A. M. Lacasta, J. M. Sancho, A. H. Romero, and K. Lindenberg, Sorting on Periodic Surfaces, *Phys. Rev. Lett.* **94**, 160601 (2005).
- [11] A. Jonáš and P. Zemánek, Light at work: The use of optical forces for particle manipulation, sorting, and analysis, *Electrophoresis* **29**, 4813 (2008).
- [12] S. Carr, D. Massatt, S. Fang, P. Cazeaux, M. Luskin, and E. Kaxiras, Twistronics: Manipulating the electronic properties of two-dimensional layered structures through their twist angle, *Phys. Rev. B* **95**, 075420 (2017).
- [13] Y. Cao, V. Fatemi, S. Fang, K. Watanabe, T. Taniguchi, E. Kaxiras, and P. Jarillo-Herrero, Unconventional superconductivity in magic-angle graphene superlattices, *Nature (London)* **556**, 43 (2018).
- [14] W. Li, C. J. O. Reichhardt, B. Jankó, and C. Reichhardt, Vortex dynamics, pinning, and angle-dependent motion on moiré patterns, *Phys. Rev. B* **104**, 024504 (2021).
- [15] S. M. Gardezi, H. Pirie, S. Carr, W. Dorrell, and J. Hoffman, Simulating twistronics in acoustic metamaterials, *2D Mater.* **8**, 031002 (2021).
- [16] N. C. X. Stuhlmüller, T. M. Fischer, and D. de las Heras, Enhanced colloidal transport in twisted magnetic patterns, *Commun. Phys.* **5**, 48 (2022).
- [17] F. Sammüller and M. Schmidt, Adaptive Brownian dynamics, *J. Chem. Phys.* **155**, 134107 (2021).
- [18] A. B. Matheson, T. Mendonca, G. M. Gibson, P. A. Dalgarno, A. J. Wright, L. Paterson, and M. Tassieri, Microrheology with an anisotropic optical trap, *Front. Phys.* **9**, 621512 (2021).
- [19] H. Löwen, Colloidal dispersions in external fields: recent developments, *J. Phys.: Condens. Matter* **20**, 404201 (2008).
- [20] C. Reichhardt and C. J. Olson Reichhardt, Dynamical Ordering and Directional Locking for Particles Moving Over Quasicrystalline Substrates, *Phys. Rev. Lett.* **106**, 060603 (2011).
- [21] C. Reichhardt and C. J. O. Reichhardt, Depinning and nonequilibrium dynamic phases of particle assemblies driven over random and ordered substrates: a review, *Rep. Prog. Phys.* **80**, 026501 (2017).
- [22] C. Reichhardt and C. J. O. Reichhardt, Structural transitions and dynamical regimes for directional locking of vortices and colloids driven over periodic substrates, *J. Phys.: Condens. Matter* **24**, 225702 (2012).
- [23] D. de las Heras and M. Schmidt, Flow and Structure in Nonequilibrium Brownian Many-Body Systems, *Phys. Rev. Lett.* **125**, 018001 (2020).
- [24] M. Schmidt, Power functional theory for many-body dynamics, *Rev. Mod. Phys.* **94**, 015007 (2022).
- [25] A. P. Antonov, A. Ryabov, and P. Maass, Solitons in overdamped Brownian dynamics, *Phys. Rev. Lett.* **129**, 080601 (2022).
- [26] J. Loehr, M. Loenne, A. Ernst, D. de las Heras, and T. M. Fischer, Topological protection of multiparticle dissipative transport, *Nat. Commun.* **7**, 11745 (2016).
- [27] D. de las Heras, J. Loehr, M. Loenne, and T. M. Fischer, Topologically protected colloidal transport above a square magnetic lattice, *New J. Phys.* **18**, 105009 (2016).
- [28] J. Loehr, D. de las Heras, M. Loenne, J. Bugase, A. Jarosz, M. Urbaniak, F. Stobiecki, A. Tomita, R. Huhnstock, I. Koch, A. Ehresmann, D. Holzinger, and T. M. Fischer, Lattice symmetries and the topologically protected transport of colloidal particles, *Soft Matter* **13**, 5044 (2017).

2.5 Competition between drift and topological transport of colloidal particles in twisted magnetic patterns

In this work we go back to the a system of twisted magnetic patterns [1]. However, in contrast to the previous work, we perform loops of the orientation of the external magnetic field in addition to a constant drift force acting on the particles. Rich phenomenology emerges due to the interplay of the two transport modes (topological transport and drift transport). We investigate hexagonal patterns twisted to the optimal twist angle, as described in section 2.3.

First, we investigate pure topological transport in twisted magnetic patterns. We observe that the transport of colloidal particles locks into one of sixteen directions when the orientation of the loops of the external magnetic field is changed. This is more than the $2 \times 6 = 12$ directions that one would naively expect from the combination of two hexagonal patterns. A remarkable similarity to publication 1 is that the average velocity of particles along the flat channels using only topological transport is larger than in other directions. This is due to the interference of the two patterns causing larger “unit”-cells along the flat channels, here the particles travel a larger distance in one loop, and hence their average velocity is higher.

When in addition to the topological transport a constant drift force is acting on the particles new transport modes arise. To study them in depth we calculated a dynamical phase diagram of the average velocity as a function of the direction of the loops and the amplitude of the drift force. There are two clearly distinguishable regions in the dynamical phase diagram separated by the critical drift force f_c . In both regions there are several different transport modes. One particularly interesting mode at subcritical drift force, is the occurrence of macroscopic transport significantly faster than pure topological transport. Here, the drift force pushes the particles along the flat channel, but the amplitude of the drift force is too small to overcome the potential barriers at the corners of the supercells. Hence the particles get stuck at the corner. However, the topological transport can move the particles over these potential barriers, provided that the direction is the appropriate one. This transport mode leads to average velocities of the particles of the order of one supercell per loop. There also exist transport modes with a subharmonic response, i.e. it takes two loops for particles to cross the corners of supercells.

At supercritical drift force, these subharmonic modes still remain, yet with much higher average velocity. When the topological transport and the drift force oppose each other, we find regions in the phase diagram with vanishing average velocity where the colloidal particles are indefinitely stuck inside a region of approximately one unit-cell.

We have also investigated the effect of finite temperature in the dynamical phase diagram. We conclude that the overall structure of the phase diagram remains unchanged at reasonable temperatures, while details get lost due to the occurrence of Brownian motion.

Publication 3

Competition between drift and topological transport of colloidal particles in twisted magnetic patterns

Under review in New J. Phys., (2023)

Submitted 24.10.2023

Nico C. X. Stuhlmüller¹, Thomas M. Fischer² & Daniel de las Heras¹

¹Theoretical Physics II, Department of Physics, University of Bayreuth, 95447 Bayreuth, Germany

²Experimental Physics X, Department of Physics, University of Bayreuth, 95447 Bayreuth, Germany.

Competition between drift and topological transport of colloidal particles in twisted magnetic patterns

Nico C. X. Stuhlmüller,¹ Thomas M. Fischer,² and Daniel de las Heras^{1,*}

¹*Theoretische Physik II, Physikalisches Institut, Universität Bayreuth, D-95440 Bayreuth, Germany*

²*Experimentalphysik X, Physikalisches Institut, Universität Bayreuth, D-95440 Bayreuth, Germany*

We simulate the motion of paramagnetic particles between two magnetic patterns with hexagonal symmetry that are twisted at a magic angle. The resulting Morié pattern develops flat channels in the magnetic potential along which colloidal particles can be transported via a drift force of magnitude larger than a critical value. Colloidal transport is also possible via modulation loops of a uniform external field with time varying orientation, in which case the transport is topologically protected. Drift and topological transport compete and cooperate giving rise to several transport modes. Cooperation makes it possible to move particles at drift forces weaker than the critical force. At supercritical drift forces the competition between the transport modes results e.g. in an increase of the average speed of the particles in integer steps and in the occurrence of subharmonic responses. We characterize the system with a dynamical phase diagram of the average particle speed as a function of the direction of the topological transport and the magnitude of the drift force.

I. INTRODUCTION

Interesting phenomenology often emerges as a result of a competition between two physical effects. Equilibrium phase transitions are a primary example. The liquid-vapor transition in simple liquids is the result of a balance between internal energy and entropy. A competition between different entropic terms drives multitude of phase transitions in hard body models [1], including the freezing transition in a system of hard spheres. In non-equilibrium, the interplay between internal interactions and external forces determines the steady states in the asymmetric simple exclusion process [2].

We study here the competition between two different transport types (topological and drift) in an out-of-equilibrium colloidal system inspired in twisted graphene [3–12]. Bilayers of graphene twisted to a magic angle show new emergent phenomena including superconductivity, ferromagnetism, antiferromagnetism and correlated insulator properties [4, 9, 13–16]. Topology plays a major role in these states [12, 17].

In our colloidal system [18], the particle transport shares some similarities with electronic transport in twisted graphene. Paramagnetic colloidal particles are placed between twisted hexagonal magnetic patterns. Due to the negative interference between the magnetic fields of both patterns, flat channels develop in the total magnetic potential acting on the particles. The flat channels percolate the entire system for patterns twisted at magic angles, in which case a weak drift force is able to sustain macroscopic transport.

We have also extensively studied (with computer simulations and experimentally) the topologically protected transport of paramagnetic colloids above single periodic magnetic patterns [19–23]. There, the transport is driven by a uniform external magnetic field of varying orientation. The orientation changes in time performing loops and there exist special loops that induce particle transport. That is, once the orientation returns to the initial one (after one loop) the particle has been transported by at least one unit cell of the magnetic pattern.

In this work, we use computer simulations to first study the topological transport in hexagonal magnetic patterns twisted at a magic angle. Next, we add a drift force acting on the particles along the direction of the flat channels and investigate the competition between drift and topological transport. We present a dynamical phase diagram of the system in the plane of direction of the topological transport and strength of the drift transport. Several transport modes arise. Some of them result from commensuration effects that involve the length of the flat channels, the period of the modulation loop, and the strength of the drift force. We also discuss briefly how the transport is affected by the occurrence of Brownian motion (finite temperature effects).

II. SETUP

Paramagnetic colloids are placed between parallel magnetic bi-layers of hexagonal patterns that are shifted by half a unit-vector and twisted at a magic angle [18]. A sketch of the system is shown in Fig. 1(a). The colloidal particles

* delasheras.daniel@gmail.com; www.danieldelasheras.com

(suspended in an inert solvent) are free to move in the middle plane located between the patterns which we refer to as action space. Experimentally, restricting the motion to a plane is possible using e.g. a polymer coating that acts as a spacer above which the particles sediment [21].

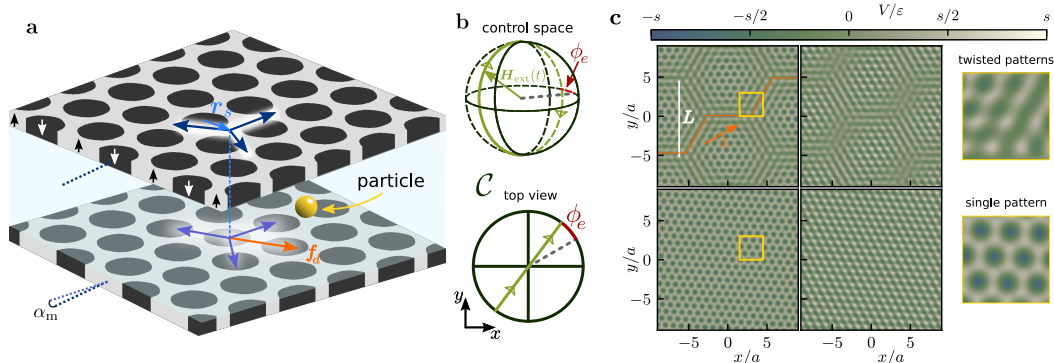


FIG. 1. **Setup and magnetic potential.** (a) Schematic overview. A paramagnetic particle (yellow) is located in the middle plane between two parallel layers of thin magnetic hexagonal patterns shifted by an in plane vector \mathbf{r}_s and afterwards rotated relative to each other by an angle α_m . Black and white regions are magnetized normal to the patterns but in opposite directions, as indicated by the white and black arrows in the upper pattern. Violet (dark blue) arrows are three rotated lattice vectors of the bottom (top) pattern, i.e. $\mathbf{R}^{\pm\alpha_m/2}\mathbf{a}_i$. A drift force (orange arrow) pushes the particle in the direction of the zig-zag like flat channels. (b) Control space \mathcal{C} depicted by a wireframe sphere. Solid lines are reader facing while dashed lines indicate that they are on the back side of the sphere. The green circle is a modulation loop performed by $\mathbf{H}_{\text{ext}}(t)$, which is itself depicted at a particular orientation using a green arrow. The direction of the loop is characterized by the angle ϕ_e , shown in red. (c) Magnetic potential V (colorbar) for different orientations of the external magnetic field (left column: north, i.e. along the z -axis, center column: along the x -axis). The first row shows the potential in presence of both patterns. A zig-zag flat channel is highlighted in orange. The drift force points in the direction of the orange arrow. The second row is the potential when only the bottom pattern is present. The third column is a close view of selected regions (yellow squares). The scale bar is $s = 45$ (top row), and $s = 25$ (bottom row).

Single hexagonal patterns can be generated by the superposition of three waves with wave vectors \mathbf{q}_i , $i = 1, 2, 3$ given by

$$\mathbf{q}_i(\alpha) = \frac{4\pi}{\sqrt{3}a} \mathbf{R}^{-\alpha} \begin{pmatrix} -\sin(2\pi i/3) \\ \cos(2\pi i/3) \end{pmatrix}, \quad (1)$$

where a is the amplitude of a lattice vector and \mathbf{R}^α is a two dimensional rotation matrix by an angle α around the axis normal to the pattern. At elevation z larger than the magnitude of a lattice vector ($z > a$), the magnetic field of a single pattern is well approximated by [18, 21, 23]

$$\mathbf{H}_p(\mathbf{r}; \alpha, \mathbf{r}_s) = H_0 a \sum_{i=1}^3 \begin{pmatrix} \mathbf{q}_i(\alpha) \sin(\mathbf{q}_i(\alpha) \cdot \mathbf{r} - \mathbf{R}^\alpha \mathbf{r}_s) \\ q \cos(\mathbf{q}_i(\alpha) \cdot \mathbf{r} - \mathbf{R}^\alpha \mathbf{r}_s) \end{pmatrix}, \quad (2)$$

where H_0 is the magnitude of the field of the pattern (controlled by the saturation magnetization of the pattern domains and the elevation z), \mathbf{r} denotes the position in action space (i.e. a plane at constant elevation above the pattern), and \mathbf{r}_s is a shift vector (parallel to the pattern). The magnetic pattern that generates such magnetic field contains regions of positive and negative magnetization normal to the pattern, see Fig. 1(a), given by

$$\mathbf{M}(\mathbf{r}; \alpha, \mathbf{r}_s) = M_0 \text{sign} \left(\sum_{i=1}^3 \cos(\mathbf{q}_i(\alpha) \cdot \mathbf{r} - \mathbf{R}^\alpha \mathbf{r}_s) + 1/2 \right), \quad (3)$$

with $\mathbf{M}_0 = M_0 \hat{\mathbf{e}}_z$ the saturation magnetization of the domains and $\hat{\mathbf{e}}_z$ the unit vector normal to the patterns. An external homogeneous magnetic field \mathbf{H}_{ext} , much stronger in amplitude than \mathbf{H}_p , drives the topological transport. The amplitude of the external field is constant in space and time, but its orientation varies with time performing

loops. That is, after a loop is completed, the orientation returns to its initial value. The set of all possible orientations of \mathbf{H}_{ext} is the surface of a sphere which we refer to as control space \mathcal{C} , see Fig. 1(b).

The total magnetic potential, V , created by the twisted patterns and the external field is proportional to the scalar product of the total magnetic field with itself

$$V \propto -(\mathbf{H}_{\text{p1}} + \mathbf{H}_{\text{p2}} + \mathbf{H}_{\text{ext}})^2. \quad (4)$$

Here \mathbf{H}_{p1} and \mathbf{H}_{p2} are the magnetic fields of each of the twisted patterns. In the limit $|\mathbf{H}_{\text{ext}}| \gg |\mathbf{H}_{\text{p}}|$, the cross-term dominates the magnetic potential which simplifies them to [18]

$$V(\mathbf{r}, t) = -2\chi\mu_0 v_{\text{eff}} (\mathbf{H}_{\text{p1}}(\mathbf{r}) + \mathbf{H}_{\text{p2}}(\mathbf{r})) \cdot \mathbf{H}_{\text{ext}}(t). \quad (5)$$

Here t is the time variable, χ denotes the magnetic susceptibility of the particles, v_{eff} their effective volume, and μ_0 is the vacuum permeability.

The patterns are parallel to each other and shifted by half a unit-vector to maximize the negative interference of the magnetic fields along the flat channels. Then, we rotate the patterns by angles $\pm\alpha_m/2$ around an axis normal to them, Fig. 1(a). We use here $\alpha_m/2 = \arctan(\sqrt{3}/33) \approx 3.00^\circ$ such that the total twist is α_m , which corresponds to the magic angle with the smallest drift force required to achieve macroscopic transport (when the external magnetic field is static and points normal to the patterns [18]).

Hence, using Eq. (2), the magnetic field of both patterns are then given by $\mathbf{H}_{\text{p1}}(\mathbf{r}) = \mathbf{H}_{\text{p}}(\mathbf{r}; -\alpha_m/2, \mathbf{a}_3/2)$ and $\mathbf{H}_{\text{p2}}(\mathbf{r}) = \mathbf{H}_{\text{p}}(\mathbf{r}; \alpha_m/2, \mathbf{0})$. The lattice vectors of the unrotated pattern are defined such that $\mathbf{a}_i \cdot \mathbf{q}_j(0) = \delta_{ij}$ for $i, j = 1, 2$ and $\mathbf{a}_3 \cdot \mathbf{q}_3(0) = 0$. (the vector \mathbf{a}_3 is a linear combination of \mathbf{a}_1 and \mathbf{a}_2). The magnetic potential, Eq. (5), that results after insertion of the expressions for \mathbf{H}_{p1} and \mathbf{H}_{p2} using Eq. (2) is valid only at the middle plane between the patterns where the colloidal particles move.

Due to the interference between the fields of both patterns a Moiré pattern develops. We call the large periodic structures of the Moiré pattern supercells. These supercells have a supercell lattice constant of $L/a = 1/(2\sin(\alpha_m/2)) \approx 9.5$ [18], with a being the magnitude of a lattice vector of one single pattern. Near the edges of the supercells there exist flat channels along which the magnetic potential is rather flat, see Fig. 1(c). These flat channels are the result of the negative interference of two wave vectors of the patterns, one from each pattern. Along the flat channels it is possible to transport colloidal particles using a weak external drift force. What makes magic angles special is that the resulting Moiré pattern is periodic with a period of one supercell (smallest possible period).

Simulations. Experiments in closely related systems are in the overdamped regime [21]. We therefore use Brownian dynamics simulations to simulate the particle motion. Three different types of transport are involved: Brownian motion induced by the implicit solvent, drift transport originated by an external force constant in space and time, and topological transport facilitated through loops of the orientation of the external magnetic field. The equation of motion of a single particle is then

$$\gamma \dot{\mathbf{r}}_p = -\nabla V(\mathbf{r}_p, t) + \mathbf{f}_d + \boldsymbol{\eta}, \quad (6)$$

where \mathbf{r}_p is the position of the particle, the overdot indicates time derivative, ∇ indicates the derivative with respect to \mathbf{r}_p , $\boldsymbol{\eta}$ is a delta correlated random force due to the implicit solvent, \mathbf{f}_d is the drift force, and γ is the friction coefficient against the implicit solvent.

We use adaptive Brownian dynamics [24] to integrate the equation of motion (the maximum relative tolerance is set to 10^{-3} and the maximum absolute tolerance to 10^{-4}). We work in units of the lattice constant of the single patterns a , the friction coefficient γ , and the energy scale of the magnetic potential, defined as $\epsilon = \chi\mu_0 v_{\text{eff}} H_0 H_{\text{ext}}$ which contains the relevant natural constants and particle characteristics together with the magnitudes of the magnetic fields, see Eq. (5). Note that the magnetic potential varies approximately $10^2\epsilon$ from minima to maxima in twisted patterns, see Fig. 1(c). Our time scale is given by $\tau = \gamma a^2 / \epsilon$.

Most simulations are done at zero temperature (i.e. no Brownian motion) because in the experimental setups the Brownian motion is usually negligible as compared to the magnetic forces [22]. Nevertheless, we briefly analyze the effect of finite temperature on the transport at the end of the Results section.

III. RESULTS

A. Pure topological transport

We first focus on the pure topological transport in twisted patterns. That is, the transport induced by modulation loops of the external magnetic field in absence of drift forces.

Topological transport in single patterns. The topological transport facilitated via magnetic forces above single periodic patterns [21–23] as well as inhomogeneous patterns [19, 20, 25] is well understood. Here, we briefly recap the fundamentals of the topological transport above periodic magnetic patterns.

The combination of the two magnetic fields (pattern and external) creates a complex energy landscape not constant in space. See the bottom panels of Fig. 1(c) for two plots of the potential in hexagonal patterns corresponding to two orientations of the external field. To understand the transport of the colloidal particles we need to focus on the stationary points of the potential. The particles are adiabatically transported via a minimum of the potential (and travel to a minimum nearby via a ratchet in case that the transporting minimum disappears during the modulation loop). Note that a maximum can be always transformed into a minimum by simply inverting the orientation of the external magnetic field, see Eq. (5). The potential also contains saddle points but the particles can only rest in the minima of the potential since a saddle point is not a local equilibrium position. There exist regions above the pattern in which V can never be a minimum for any orientation of \mathbf{H}_{ext} . Those regions are called the forbidden regions [22] and they can contain only saddle points. The regions for which there exist an orientation in \mathbf{H}_{ext} such that V is minimum are called the allowed regions. In the allowed regions it is always possible to find a minimum (or a maximum) of V but never a saddle-point. The complete action space splits into forbidden and allowed regions, the shape of which varies with the symmetry of the pattern [21].

The boundaries between allowed and forbidden regions in action space are the fences. The intersection of fences in action space are the gates as they allow particles to move from one allowed region to the adjacent one. Both fences and gates also exist in control space. To transport a particle in action space, the modulation loop in control space need to wind around special orientations of the external field (determined by the position of the fences in \mathcal{C}). The set of winding numbers of the modulation loop around the special orientations in \mathcal{C} is the topological invariant that protects the motion and determines the transport direction. The exact path follow by the loop in \mathcal{C} is irrelevant in the sense that any two loops with the same topological invariant will transport a particle between the same type of allowed regions. In hexagonal patterns, it is possible to transport particles along six directions given by $\pm\mathbf{a}_i$ with $i = 1, 2, 3$.

Topological transport in twisted patterns. We investigate next the topological transport in hexagonal magnetic patterns twisted at a magic angle. To transport the particles, we impose an external magnetic field that orbits control space following great circles. The modulation loop crosses both poles of \mathcal{C} and the equator at latitudes ϕ_e and $\phi_e + \pi$. We measure ϕ_e relative to the average direction between two consecutive flat channels (counterclockwise rotation by thirty degrees of the x -axis [18]). An illustration of a modulation loop together with \mathcal{C} can be seen in Fig. 1(b). The period of one loop is set to $\tau_0/\tau = 5$. The total magnetic potential varies along the modulation loop. Figure 1(c) depicts the magnetic potential for two different orientations of the external magnetic field in both twisted and single patterns.

When continuously varying ϕ_e along the equator, the direction of transport locks into one of sixteen discrete directions, see particle trajectories in Fig. 2(a). Six of these directions point along the flat channels that develop near the edges of the supercells. Six other directions point along the lattice vectors of the hexagonal Moiré grid. The last four directions point roughly orthogonal to the conducting flat channel. The topological transport between twisted pattern is possible along more directions than one would naively expect from the combination of two single patterns (i.e., $2 \times 6 = 12$ directions). Analogous to single patterns, the transport direction is not a continuous function of the orientation of the loop in control space, but it rather shows discrete topological transitions.

In order measure the efficiency of the topological transport, we calculate the average speed of the particles during the modulation loop. We average over one hundred different realizations. The particles are initialized randomly in a square region with side length $10a$ around the origin that covers a complete supercell. To eliminate the dependence on the initial conditions, we let the system reach a steady state by applying fifty modulation loops before measuring the average speed μ during another fifty loops, i.e.

$$\mu = \frac{1}{50\tau_0} \langle |\mathbf{r}_p(100\tau_0) - \mathbf{r}_p(50\tau_0)| \rangle, \quad (7)$$

where $\langle \cdot \rangle$ denotes the average over the different realizations.

The average speed as a function of the angle ϕ_e is depicted in Fig. 2(b) for two values of the temperature $k_B T/\epsilon = 0$ and 0.1 , with k_B the Boltzmann constant. The transport along any of the flat channels is faster than that along the six directions of the underlying hexagonal patterns. In most cases, the particles that move along the flat channels do so with an average speed of approx. $1.4a/\tau_0$ and reach a peak speed of $1.6a/\tau_0$ in some specific cases. In contrast, the average speed along the symmetry directions of the inner cells of the combined patterns is $1a/\tau_0$, which is the same as in single hexagonal patterns (one unit cell per loop). The increased speed along the flat channels arises from the Moiré pattern. Units cells with parallelogram symmetry and larger than the hexagonal cells form along the flat channels due to the negative interference between two pattern waves. Therefore, the particles travel a larger distance per loop along the flat channels than along the hexagonal lattice vectors (even though in both cases one modulation

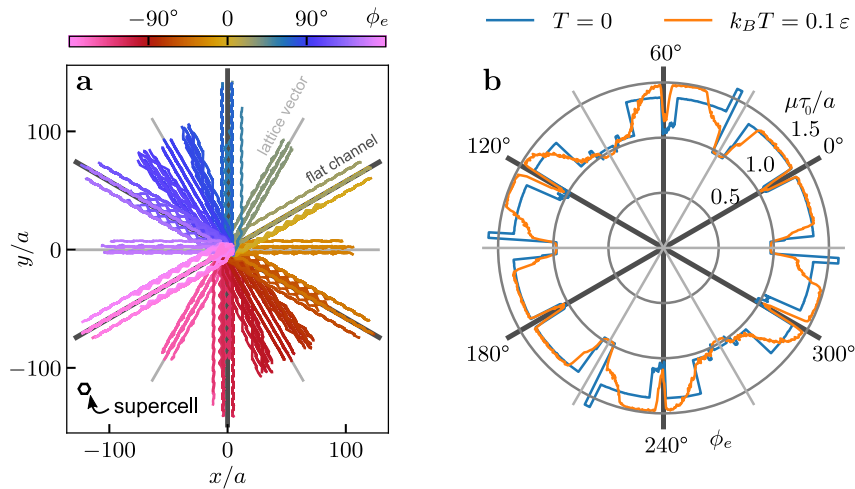


FIG. 2. **Pure topological transport.** (a) Trajectories of particles located between patterns twisted at a magic angle. The small hexagon in the bottom left of (a) depicts the size of a supercell. The particles are randomly initialized around the origin and driven by 100 modulation loops of different orientation ϕ_e . The trajectories are colored according to the direction of the modulation loop ϕ_e (see color bar). (b) Average speed of the particles μ for different values of the orientation of the modulation loops ϕ_e and two values of the temperature: $T = 0$ (blue line) and $k_B T/\epsilon = 0.1$ (orange line). Thick-dark gray lines point in the average direction of flat channels. Thin-light gray lines point in the direction of the unit vectors of the supercells.

loop transports the particles one unit cell). The Brownian motion smooths, as expected, the zero temperature results but the main characteristics of the transport remain unchanged, cf. the blue and orange curves in Fig. 2(b).

Concentrating particles into the flat channels. As discussed, there exist loops that transport the particles in the directions of the flat channels and hence it is possible to concentrate all particles in there. This is helpful for the transport in twisted patterns using drift forces [18] since the particles that are stuck inside the supercells could be moved towards the flat channels and become therefore mobile.

B. Pure drift transport

Before we discuss the interplay between drift and topological transport, we briefly summarize the transport due to only drift forces. A complete description of the pure drift transport is given in Ref. [18]. There, the external magnetic field is static and points normal to the pattern. A uniform drift force of magnitude f_d drives the motion. The optimal direction of the drift force is along the average direction of two consecutive flat channels, see Fig. 1(c). For patterns twisted at magic angles, the magnetic potential is periodic with a periodicity of one supercell. The particles can get pushed easily through the flat channels located near the edges of supercells provided that the magnitude of the drift force is above a critical value f_c . For the system investigated here the critical force is $f_c = 39.5\epsilon/a$ [18]. For weaker drift forces the particles located in a flat channel get stuck at the corners of the supercells, i.e. the place where two flat channels meet. The particles that are located outside of the flat channels are forever trapped even for magnitudes of the drift force much larger than the critical one.

C. Combined drift and topological transport

In Fig. 3 we show the trajectories of particles subject to both a drift force and a modulation loop of the external magnetic field. The trajectories are colored according to the orientation of the modulation loop ϕ_e . We depict trajectories for a drift force much weaker, weaker, and stronger than the critical drift force in Figs. 3(a), 3(b) and 3(c), respectively. Even at subcritical drift forces the speed in the direction of the drift force is increased. For weak drift forces, $f_d \ll f_c$, the particles are pushed along the flat channels until they hit a corner and get stuck. Therefore the

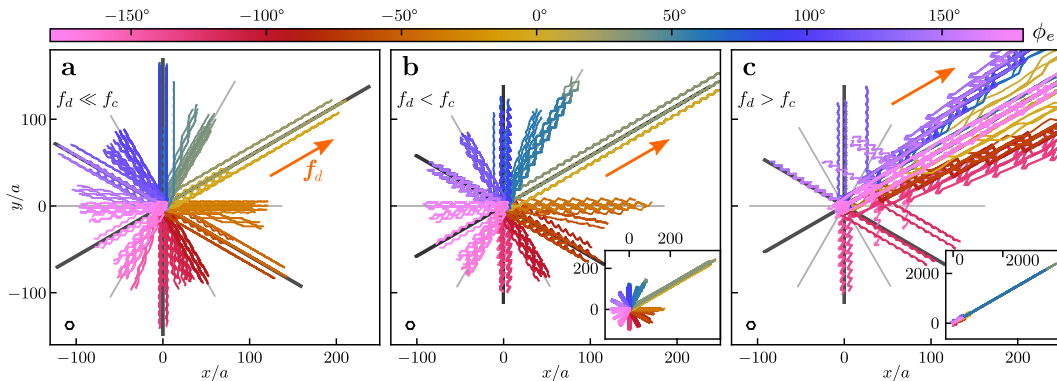


FIG. 3. **Topological and drift transport.** Trajectories of particles located between patterns twisted at a magic angle and driven by both a drift force of magnitude f_d and 100 modulation loops of orientation ϕ_e . The particles are randomly initialized around the origin. The trajectories are colored according to the direction of the modulation loop ϕ_e (see color bar). The magnitude of the drift force is $f_d a/\epsilon = 5$ (a), 25 (b), and 45 (c). That is, below (a,b) and above (c) the critical drift force $f_c a/\epsilon = 39.5$. The insets in panels (b) and (c) show the complete trajectories of the particles after 100 loops. The orange arrows indicate the direction of the drift force.

particles can travel up to L per loop even if $f_d \ll f_c$.

At supercritical drift forces, $f_d > f_c$, the particles can overcome the potential barriers at the corners of the supercells and the transport is then dominated by the drift force. At first glance, the topological transport hinders the transport along the flat channels as compared to a system without topological loops. There, \mathbf{H}_{ext} always points normal to the patterns which is optimal to increase the colloidal mobility. However, to achieve macroscopic transport the topological loops are important. Without the modulation loops, only the particles that are initialized close enough to a flat channels can move. Particles inside the supercells would remain there. The topological loops are able to move the particles towards the flat channels and therefore to enable macroscopic transport.

A general effect of the drift force is that the direction of transport migrates towards the average direction between two consecutive flat channels. This is expected since whenever a particle enters a flat channel, it gets transported along the channel.

D. Dynamical phase diagram

To rationalize the complex interplay between drift and topological transport, we plot in Fig. 4(a) a dynamical phase diagram in which we represent the average speed μ (color coded), see Eq. (7), as a function of the direction of the topological loop (ϕ_e) and the magnitude of the drift force (f_d). The competition between the drift force and the topological transport generates a rich phenomenology. Two main regions corresponding to sub- and super-critical drift forces are clearly visible, see Figs. 4(b) and 4(c), respectively. We have identified several transport modes for which we show illustrative trajectories in Fig. 4 panels (d) to (l) and in the Supplementary Movies.

E. Sub-critical drift forces

We discuss first the region where the amplitude of the drift force is below the critical value that would allow particles to move freely through the flat channels [18], i.e. $f_d < f_c$.

Enhanced transport. Even for very weak drift forces, the particles can traverse the flat channels near the edges of supercells when the external magnetic field points normal to the pattern. However, they can not overcome the potential barrier that exists in the corners of the flat channels as long as the amplitude of the drift force is subcritical. Topological transport induced by a nontrivial loop is needed in order to move the particles around the corner and hence achieve macroscopic transport. There are two corners that need to be crossed per supercell. Hence, the highest average speed that we would naively expect is $\mu \approx L/(2\tau_0) \approx 4.77 a/\tau_0$. This value corresponds to particles crossing one corner per modulation loop.

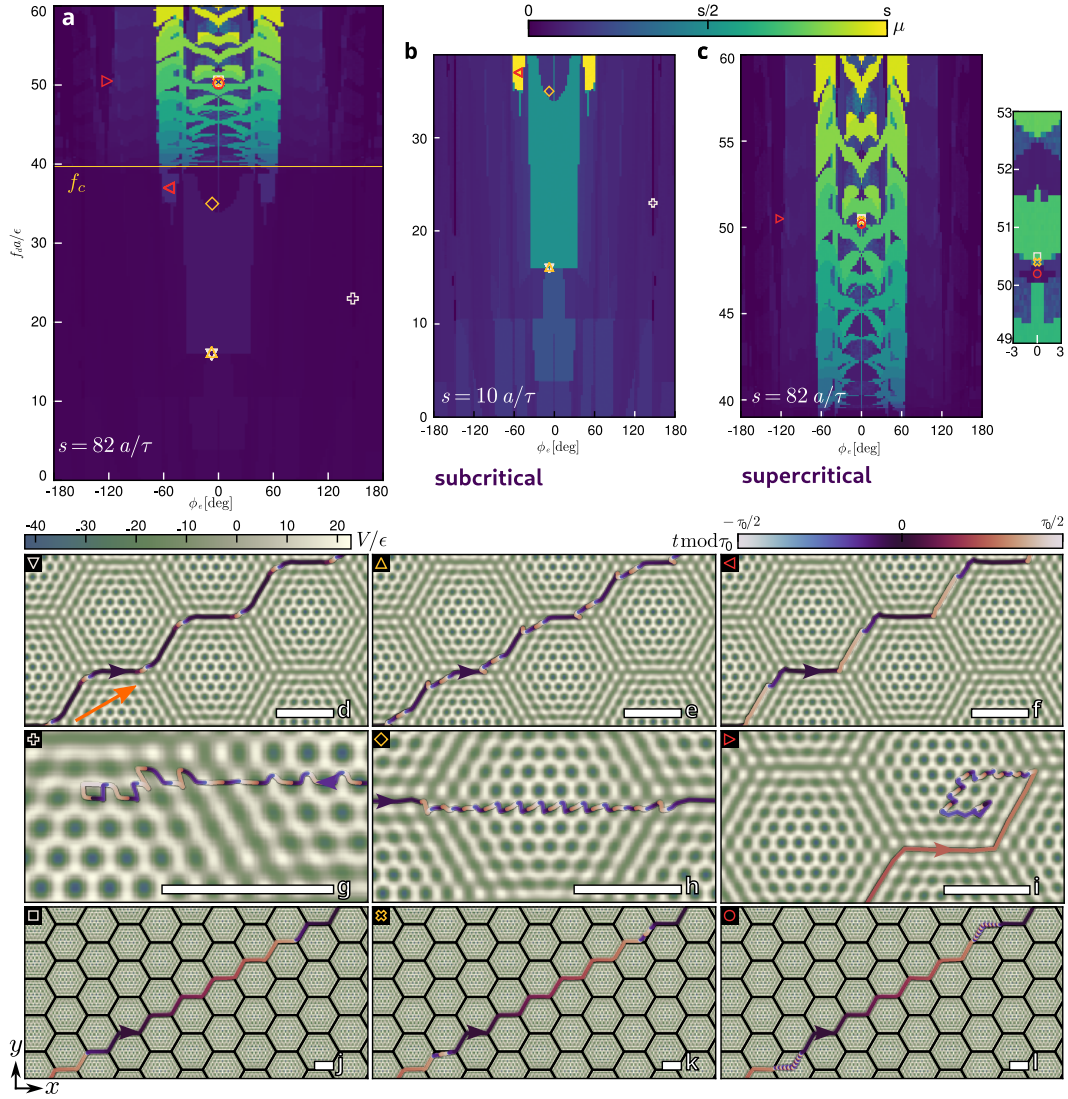


FIG. 4. **Dynamical phase diagram.** Average speed of the particles (μ colorbar) as a function of the direction of the modulation loops ϕ_e and the amplitude of the drift force f_d . Panel (a) shows the complete dynamical phase diagram, whereas panels (b) and (c) are enlarged views of the subcritical $f_d < f_c$ and supercritical regions $f_d > f_c$. The yellow line in (a) indicates the critical drift force. The resolution in panels (a), (b), and (c) is $0.1 a/\epsilon$ and 3° for the main panels and 0.3° for the close view in (c). Illustrative trajectories at specific state points (indicated by symbols) are shown in panels (d) to (l). The background depicts the magnetic potential (V colorbar) when the external magnetic field points along the z -axis (north of control space). The orange arrow in (d) indicates the direction of the drift force. The particle trajectories are colored according to the temporal evolution of the external loops that drives them ($t \bmod \tau_0$ colorbar). The loop points towards the north (south) of control space if $t \bmod \tau_0$ is in an interval of width $\tau_0/4$ around 0 ($\tau_0/2$). In panels (j) to (l) the supercells are surrounded by a black outline to increase their visibility. The scale bars have a length of $5a$. The amplitudes of the drift forces are $f_d a/\epsilon = 16.1$ (d), 16.0 (e), 37.0 (f), 23.0 (g), 35.0 (h), 50.5 (i), 50.5 (j), 50.4 (k), 50.2 (l) and the orientation of the modulation loop $\phi_e = -7.5^\circ$ (d), -7.5° (e), -52.5° (f), 147.0° (g), -7.5° (h), -172.5° (i), 0.0° (j), 0.0° (k), 0.0° (l).

Depending on the value of ϕ_e , the modulation loop can transport the particles into a conducting flat channel, into a nonconducting channel, or into the inner regions of supercells. To achieve high speed transport at subcritical drift forces, we need to transport particles from one conducting channel to the next one using the least possible amount of loops. This can be done with only a single loop provided that ϕ_e is within the approximate interval $[-40^\circ, 40^\circ]$ and that $f_d > 16\epsilon/a$. In this case, an average speed of $\mu \approx L/(2\tau_0) \approx 4.77 a/\tau_0$ can be reached, see Figs. 4(a) and 4(b). Illustrative trajectories showing this transport mode are shown in Fig. 4(d) and Supplementary Movie 1.

A transport mode with half the average speed of the previous mode is shown in Fig. 4(e) and Supplementary Movie 2. This mode happens for smaller drift forces, i.e. $f_d < 16\epsilon/a$, but within roughly the same interval of orientations of the external loop, see Fig. 4(b). Here the drift force is not strong enough to push the particles into the corner of the flat channels. Instead, the particles stop approximately one unit cell away from the corner. Therefore, two modulation loops are required for the particles to cross each corner. One loop is needed to transport the particle into the corner and another loop to transport the particle over the corner. This results in an average speed of half a flat channel per loop, i.e. $\mu \approx L/(4\tau_0) \approx 2.38$.

If the particles get scattered into non-conducting channels or into a supercell, the average speed becomes close to $\mu \sim a/\tau_0$, as it takes of the order of L/a loops to traverse the supercell and hence get back to a conducting channel. This transport mode is also present at supercritical drift forces. An illustrative trajectory is shown in Fig. 4(h) and Supplementary Movie 3.

Unexpectedly, an average speed corresponding to traverse one entire supercell per loop is also possible even for subcritical drift forces. This transport mode is due to the occurrence of secondary transient flat channels parallel to the main flat channel and separated by a distance of half the magnitude of a lattice vector [18]. These flat channels become the local minimum when the external magnetic field points towards the south pole of \mathcal{C} . For a range of drift forces and orientations of the modulation loop, there exist a commensuration effect between the drift and the topological transport. The external field switches from north to south and back to north at the right times when the particles are sufficiently close to the corners of the supercells. This allows the particles to pass the corner by moving to the active flat channels at all times during the loop. As a result the particles are never stuck in the corners and travel always in a flat channel with average speed of $\mu \approx L/\tau_0 \approx 9.57 a/\tau_0$. A trajectory is shown in Fig. 4(f) and Supplementary Movie 4. Note how the loop moves the particles from one channel to the next one at positions close to the corners of the supercells.

Reduced transport. The interplay between topological and drift transport can also reduce the average speed below that of the pure topological transport $\mu \approx a/\tau_0$. For external loops with directions ϕ_e within the intervals $[-180^\circ, -90^\circ]$ and $[90^\circ, 180^\circ]$ an average speed of less than one unit cell per loop is prevalent. In this region, the modulation loops transport the particles in a direction with a component opposite to the drift force. When the particles enter a flat channel they move along the channel, i.e., opposite to the direction facilitated by the modulation loops. As a result the average speed decreases substantially. In extreme cases, the average speed vanishes as the particles get trapped in a closed trajectory where the modulation loop and the drift force cause particles to never leave an area of one unit cell. An illustrative particle trajectory is shown in Fig. 4(g) and Supplementary Movie 5.

F. Supercritical drift forces

At drift forces larger than the critical drift force, i.e. $f_d > f_c$, the dynamical phase diagram shows a complex structure for modulation loops pointing roughly in the interval $\phi_e \in [-60^\circ, 60^\circ]$, see Figs. 4(a) and 4(c). Here, regions of high and low average speed alternate quickly when increasing the magnitude of the drift force. Fast transport is achieved when the particles stay in the flat channels, see an example in Fig. 4(j) and Supplementary movie 6. In these cases the particles can get trapped at the corners of the supercells when the loop blocks the corner. The loop then continues in such a way that the particles are transported through the corner into the flat channel. Recall that the critical drift force corresponds to the optimal orientation of the external field (pointing towards the north of control space). Hence, even though we explore now the region $f_d > f_c$ the particles can get stuck at the corners for other orientations of the external field.

In the slow regions, the particles are forced to move inside the supercells by the topological transport. There they need $\mathcal{O}(L/a)$ loops to traverse the supercell and reach a flat channel again. Once they are in a flat channel they can traverse it during one loop, after which they are forced back into the interior region of a supercell. Averaging over many loops causes the average speed of the particles to be $\mathcal{O}(a/\tau_0)$ since the low speed in the supercells dominates over the high speed in the flat channel. An illustrative trajectory is shown in Fig. 4(l) and Supplementary Movie 7.

When going from one region of high speed to the next one by increasing the drift force, see Fig. 4(c), the average speed increases by the length of one edge of a supercell per loop, i.e. $L/(2\tau_0)$. Due to the stronger drift force, the particles can travel along the flat channels at higher speed which allows them to traverse one more edge during the loop as compared to the previous high speed region.

The shape of the fast regions in the dynamical phase diagram resembles the Hofstadter's butterfly [26], known from the commensuration effects in the quantum Hall effect and in twisted bilayer graphene [27, 28]. Here, commensuration effects between the topological and the drift transport occur. The time required to traverse one edge of a supercell is roughly $t_e \approx (L/2)/\mu_e$ with μ_e the speed along the flat channel. At zero temperature, μ_e is mostly determined by the drift force $\mu_e \approx f_d/\gamma$, and hence $t_e \approx \gamma(L/2)/f_d$. When the period of the modulation loop commensurates with this time there is fast region in the supercritical dynamical phase diagram. Since in our system $L/a \approx 9.5$ and $\tau_0 = 5\tau$ we expect fast regions to occur at intervals $\Delta f_d \approx 1$ which is consistent with the simulation results, Fig. 4(c). If t_e and τ_0 do not commensurate, the particles get transported in the interior regions of the supercells and their average speed is reduced considerably.

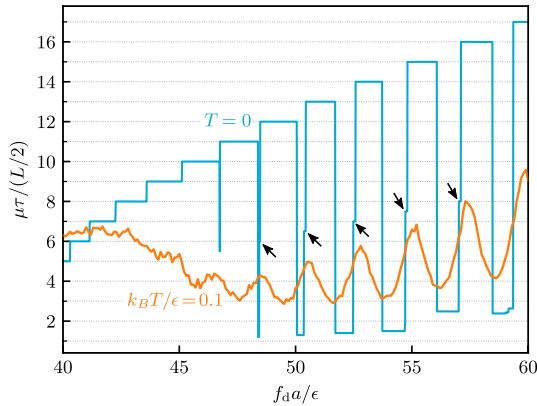


FIG. 5. **Scaled average speed.** Average speed μ (scaled with the speed corresponding to travel half a supercell per loop) as a function of the magnitude of the drift force f_d in the supercritical region ($f_d > f_c$). The direction of the modulation loop is $\phi_e = 0$. The arrows indicate the regions in which the average speed jumps to half the value of the next high average speed region. The horizontal dotted-lines indicate the integer values of the scaled average speed. Results for zero temperature (blue) and finite temperature (orange) are shown.

If one rescales the average speed of the particles by the length of flat channels, i.e. measure the average speed in units of $L/(2\tau_0)$, the rescaled average speed increases in integer steps, similar to the quantum Hall effect, see Fig. 5. The figure corresponds to a vertical cut of the dynamical phase diagram for supercritical drift forces and $\phi_e = 0^\circ$. A close inspection to the data shown in the figure reveals that there exists an intermediate step between fast and slow regions in which the response is subharmonic. There, the particles never leave the flat channels but they require two loops to continue their path along the flat channel. This phenomenon can be seen in Fig. 4(k) and Supplementary Movie 8. The system responds with only half the frequency of the external modulation.

Complete stop. Even for supercritical drift forces, there are large regions of the phase diagram with very low average speed. There, the direction of the topological transport opposes the direction of the drift force. In some cases the particles can be brought to a complete halt. See an illustrative trajectory in Fig. 4(i) and Supplementary Movie 9. This happens for supercritical forces and loop orientations ϕ_e within the intervals $[-180^\circ, -155^\circ]$ and $[155^\circ, 180^\circ]$ approximately.

G. Finite temperature

The general structure of the phase diagram is robust against Brownian motion. We show in Fig. 6 the dynamical phase diagram at temperature $k_B T/\epsilon = 0.1$. The alternation between fast and slow regions for supercritical forces resembles those found in the limit of vanishing temperature, Fig. 4(a). The discrete steps in the average speed get broadened by the effect of the temperature and the plateaus do not reach the same heights. This broadening is wider than the size in which the subharmonic response occurs, which therefore disappears at this temperature (compare the zero and finite temperature curves in Fig. 5).

Also, the main features of the dynamical phase diagram at subcritical forces remain the same in presence of Brownian motion. Particles reach an average speed of more than one supercell per loop even for drift forces smaller than the

critical force. This was expected as thermal fluctuations allow the particles to cross the corners of flat channels even if the drift force is not strong enough.

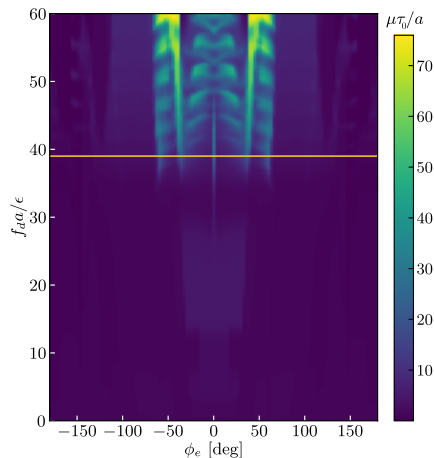


FIG. 6. **Finite temperature.** Dynamical phase diagram at finite temperature ($k_B T / \epsilon = 0.1$) of the average speed of the colloidal particles μ (colorbar) in the plane of direction of the topological loop ϕ_e and magnitude of the drift force f_d . The horizontal yellow line indicates the magnitude of the critical drift force in the limit of zero temperature.

IV. CONCLUSIONS

We have shown that topologically nontrivial loops of the orientation of a uniform external magnetic field can transport paramagnetic particles located between twisted magnetic patterns. Topological transport is possible along several directions including the flat channels of the twisted Moiré pattern and the lattice vectors of the hexagonal pattern that emerges inside the supercells.

The competition between topological and drift transport gives rise to a plethora of interesting transport modes. These include integer steps in the average speed of the particles, a subharmonic response, and a complete transport stop.

Based on previous works [19–22], we expect a good agreement between simulations and experiments. It should however be noted that small imperfections on the magnetization domains can have a large effect on the transport along flat channels using only drift forces [29]. Hence, very precise magnetic patterns might be required to observe the complete phenomenology reported here. Performing experiments on twisted patterns is not as simple as using single patterns. Simply tracking the motion of particles sandwiched between two opaque patterns is already not simple since optical microscopy is no longer possible. As an alternative, one could create single magnetic patterns designed to mimic the pattern field of two patterns twisted at magic angles. A gradient pressure and the gravitational field are examples of possible drift forces that could be used in e.g. a magnetophoretic device [30–32].

We have only considered the limit of very dilute suspensions with no interparticle interactions. It would be interesting to study the effects that the many-body interparticle interactions have on the transport. Many-body non-equilibrium superadiabatic forces [33, 34] might alter the dynamical phase diagram and new states such as the occurrence of solitons [35, 36] might appear. Interparticle repulsion might scatter particles away from the flat channels, while interparticle attraction could drag particles together through flat channels resulting in an increased mobility. Hydrodynamic effects, which have not been considered here, might also alter the phenomenology.

V. DATA AVAILABILITY

All the data supporting the findings are available from the corresponding author upon reasonable request.

VI. ACKNOWLEDGMENTS

We acknowledge funding by the Deutsche Forschungsgemeinschaft (DFG, German Research Foundation) under project numbers 440764520 and 531559581.

-
- [1] D. Frenkel, Order through entropy, *Nat. Mater.* **14**, 9 (2014).
- [2] B. Derrida, An exactly soluble non-equilibrium system: The asymmetric simple exclusion process, *Phys. Rep.* **301**, 65 (1998).
- [3] Y. Saito, F. Yang, J. Ge, X. Liu, T. Taniguchi, K. Watanabe, J. Li, E. Berg, and A. F. Young, Isospin Pomeranchuk effect in twisted bilayer graphene, *Nature* **592**, 220 (2021).
- [4] K. P. Nuckolls, M. Oh, D. Wong, B. Lian, K. Watanabe, T. Taniguchi, B. A. Bernevig, and A. Yazdani, Strongly correlated Chern insulators in magic-angle twisted bilayer graphene, *Nature* **588**, 610 (2020).
- [5] C. Shen, Y. Chu, Q. Wu, N. Li, S. Wang, Y. Zhao, J. Tang, J. Liu, J. Tian, K. Watanabe, *et al.*, Correlated states in twisted double bilayer graphene, *Nat. Phys.* **16**, 520 (2020).
- [6] T. Kariyado and A. Vishwanath, Flat band in twisted bilayer Bravais lattices, *Phys. Rev. Res.* **1**, 033076 (2019).
- [7] G. Hu, Q. Ou, G. Si, Y. Wu, J. Wu, Z. Dai, A. Krasnok, Y. Mazor, Q. Zhang, Q. Bao, *et al.*, Topological polaritons and photonic magic angles in twisted α -MoO₃ bilayers, *Nature* **582**, 209 (2020).
- [8] T. Kariyado and A. Vishwanath, Flat band in twisted bilayer Bravais lattices, *Phys. Rev. Res.* **1**, 033076 (2019).
- [9] M. Yankowitz, S. Chen, H. Polshyn, Y. Zhang, K. Watanabe, T. Taniguchi, D. Graf, A. F. Young, and C. R. Dean, Tuning superconductivity in twisted bilayer graphene, *Science* **363**, 1059 (2019).
- [10] R. Bistritzer and A. H. MacDonald, Moiré bands in twisted double-layer graphene, *Proc. Natl. Acad. Sci.* **108**, 12233 (2011).
- [11] E. Suárez Morell, J. D. Correa, P. Vargas, M. Pacheco, and Z. Barticevic, Flat bands in slightly twisted bilayer graphene: Tight-binding calculations, *Phys. Rev. B* **82**, 121407 (2010).
- [12] Z. Song, Z. Wang, W. Shi, G. Li, C. Fang, and B. A. Bernevig, All magic angles in twisted bilayer graphene are topological, *Phys. Rev. Lett.* **123**, 036401 (2019).
- [13] A. L. Sharpe, E. J. Fox, A. W. Barnard, J. Finney, K. Watanabe, T. Taniguchi, M. A. Kastner, and D. Goldhaber-Gordon, Emergent ferromagnetism near three-quarters filling in twisted bilayer graphene, *Science* **365**, 605 (2019).
- [14] X. Lu, P. Stepanov, W. Yang, M. Xie, M. A. Aamir, I. Das, C. Urgell, K. Watanabe, T. Taniguchi, G. Zhang, *et al.*, Superconductors, orbital magnets and correlated states in magic-angle bilayer graphene, *Nature* **574**, 653 (2019).
- [15] Y. Cao, V. Fatemi, S. Fang, K. Watanabe, T. Taniguchi, E. Kaxiras, and P. Jarillo-Herrero, Unconventional superconductivity in magic-angle graphene superlattices, *Nature* **556**, 43 (2018).
- [16] Y. Cao, V. Fatemi, A. Demir, S. Fang, S. L. Tomarken, J. Y. Luo, J. D. Sanchez-Yamagishi, K. Watanabe, T. Taniguchi, E. Kaxiras, *et al.*, Correlated insulator behaviour at half-filling in magic-angle graphene superlattices, *Nature* **556**, 80 (2018).
- [17] H. C. Po, L. Zou, T. Senthil, and A. Vishwanath, Faithful tight-binding models and fragile topology of magic-angle bilayer graphene, *Phys. Rev. B* **99**, 195455 (2019).
- [18] N. C. X. Stuhlmüller, T. M. Fischer, and D. de las Heras, Enhanced colloidal transport in twisted magnetic patterns, *Commun. Phys.* **5**, 48 (2022).
- [19] H. Massana-Cid, A. Ernst, D. de las Heras, A. Jarosz, M. Urbaniak, F. Stobiecki, A. Tomita, R. Huhnstock, I. Koch, A. Ehresmann, D. Holzinger, and T. M. Fischer, Edge transport at the boundary between topologically equivalent lattices, *Soft Matter* **15**, 1539 (2019).
- [20] J. Loehr, D. de las Heras, A. Jarosz, M. Urbaniak, F. Stobiecki, A. Tomita, R. Huhnstock, I. Koch, A. Ehresmann, D. Holzinger, and T. M. Fischer, Colloidal topological insulators, *Commun. Phys.* **1**, 4 (2018).
- [21] J. Loehr, D. de las Heras, M. Loenne, J. Bugase, A. Jarosz, M. Urbaniak, F. Stobiecki, A. Tomita, R. Huhnstock, I. Koch, A. Ehresmann, D. Holzinger, and T. M. Fischer, Lattice symmetries and the topologically protected transport of colloidal particles, *Soft Matter* **13**, 5044 (2017).
- [22] J. Loehr, M. Loenne, A. Ernst, D. de las Heras, and T. M. Fischer, Topological protection of multiparticle dissipative transport, *Nat. Commun.* **7**, 11745 (2016).
- [23] D. de las Heras, J. Loehr, M. Loenne, and T. M. Fischer, Topologically protected colloidal transport above a square magnetic lattice, *New J. Phys.* **18**, 105009 (2016).
- [24] F. Sammler and M. Schmidt, Adaptive brownian dynamics, *J. Chem. Phys.* **155**, 134107 (2021).
- [25] N. C. X. Stuhlmüller, F. Farrokhzad, P. Kuświk, F. Stobiecki, M. Urbaniak, S. Akhundzada, A. Ehresmann, T. M. Fischer, and D. de las Heras, Simultaneous and independent topological control of identical microparticles in non-periodic energy landscapes, Under review (2023).
- [26] D. R. Hofstadter, Energy levels and wave functions of bloch electrons in rational and irrational magnetic fields, *Phys. Rev. B* **14**, 2239 (1976).
- [27] J. A. Crosse, N. Nakatsuji, M. Koshino, and P. Moon, Hofstadter butterfly and the quantum hall effect in twisted double bilayer graphene, *Phys. Rev. B* **102**, 035421 (2020).

- [28] C. R. Dean, L. Wang, P. Maher, C. Forsythe, F. Ghahari, Y. Gao, J. Katoch, M. Ishigami, P. Moon, M. Koshino, T. Taniguchi, K. Watanabe, K. L. Shepard, J. Hone, and P. Kim, Hofstadter's butterfly and the fractal quantum hall effect in moiré superlattices, *Nature* **497**, 598 (2013).
- [29] A. M. E. B. Rossi, A. Ernst, M. Dörfler, and T. M. Fischer, Disorder scattering in classical flat channel transport of particles between twisted magnetic square patterns, In preparation (2023).
- [30] B. Lim, V. Reddy, X. Hu, K. Kim, M. Jadhav, R. Abedini-Nassab, Y.-W. Noh, Y. T. Lim, B. B. Yellen, and C. Kim, Magnetophoretic circuits for digital control of single particles and cells, *Nat. Commun.* **5**, 3846 (2014).
- [31] W. H. Chong, S. S. Leong, and J. Lim, Design and operation of magnetophoretic systems at microscale: Device and particle approaches, *Electrophor.* **42**, 2303 (2021).
- [32] R. Abedini-Nassab, N. Sadeghidelouei, and C. W. Shields IV, Magnetophoretic circuits: A review of device designs and implementation for precise single-cell manipulation, *Anal. Chim. Acta* **1272**, 341425 (2023).
- [33] D. de las Heras and M. Schmidt, Flow and structure in nonequilibrium brownian many-body systems, *Phys. Rev. Lett.* **125**, 018001 (2020).
- [34] D. de las Heras, T. Zimmermann, F. Sammüller, S. Hermann, and M. Schmidt, Perspective: How to overcome dynamical density functional theory, *J. Phys.: Condens. Matter* **35**, 271501 (2023).
- [35] A. P. Antonov, A. Ryabov, and P. Maass, Solitons in overdamped brownian dynamics, *Phys. Rev. Lett.* **129**, 080601 (2022).
- [36] P. Tierno, E. Cereceda-López, A. Antonov, A. Ryabov, and P. Maass, Overcrowding induces fast colloidal solitons in a slowly rotating potential landscape 10.21203/rs.3.rs-2704291/v1 (2023).

2.6 Simultaneous and independent topological control of identical microparticles in non-periodic energy landscapes

After having studied the motion of colloidal particles in twisted patterns, we investigate the transport of magnetic colloidal particles above single inhomogeneous patterns. Here, we find multiple ways to make identical particles move in different directions when subject to the influence of a single loop of the orientation of the external magnetic field. As mentioned in section 1.3, multidirectional transport of magnetic colloidal particles above magnetic patterns was previously only possible by using different types of particles, or complex magnetic octupoles. Here, we use inhomogeneous patterns to make the direction of transport dependent on the absolute position of simple paramagnetic particles above the pattern. Brownian dynamics simulations and experiments coincide up to experimental and numerical uncertainties. The particles are moved solely by topological transport facilitated through loops of the orientation of the external magnetic field.

We first vary the symmetry phase of hexagonal patterns, discussed in section 1.3, to construct complex patterns above which the transport of colloidal particles can be controlled with simple loops of \mathbf{H}_{ext} . By changing the symmetry phase of the pattern locally, we can change the direction in which the particles travel at that position above the pattern. By doing so we create a complex pattern, above which the particles can be controlled with relatively simple loops. Later we do the opposite; we design simple patterns, but complex loops. As a first proof of concept of the first approach we design a particle trap by changing the symmetry phase linearly with the polar angle around the center of the pattern. This creates a topological defect in the symmetry phase at the center of the pattern, which can act as an attractor for particles, given the appropriate loop. This trap is not only for academic purposes, it also solves the problem of needing to manually initialize particles to specific locations above the patterns in experimental realizations. The trap allows randomly initialized particles to get concentrated in the center of the trap. After several repetitions of the loop there will be a particle in the center of the trap. The particle can then be moved to an arbitrary position by applying the corresponding loops.

We then locally change the symmetry phase of the pattern to a more complex structure in order for the particles to follow an arbitrarily complex trajectory;

the letter “B” in our case. This illustrates that we have precise control over the particles and can let them do arbitrary tasks.

Next we focus on a different approach: using simple patterns but intricate loops. The simple patterns are composed of subpatterns of the same symmetry class that are rotated relative to each other. As these subpatterns have their fences in different locations in \mathcal{C} , we can transport particles above the different subpatterns independently. We demonstrate that we have complete control of the particles by writing the letters “A” through “D” in differently rotated subpatterns with simulations and experiments. We then show using simulations that when experimental constraints are overcome, there is the possibility to do more intricate tasks, such as writing the letters “A” through “R” simultaneously.

Finally, we combine the two approaches. In order to overcome the initialization hurdles, we add our trap patterns to the patterns of different rotations. This allows us to randomly initialize particles above the trap patterns, repeat the attractor loop several times until we can be sure that the particles are in the trap. Afterwards we move the particles to a desired position above the rotated patterns, and let them draw the shape of a square, a triangle and a cross simultaneously and independently.

Publication 4

Simultaneous and independent topological control of identical microparticles in non-periodic energy landscapes

Nat. Commun. **14**, 7517 (2023)

Nico C. X. Stuhlmüller¹, Farzaneh Farrokhzad², Piotr Kuświk³,
Feliks Stobiecki³, Maciej Urbaniak³, Sapida Akhundzada⁴,
Arno Ehresmann⁴, Thomas M. Fischer² & Daniel de las Heras¹

¹Theoretical Physics II, Department of Physics, University of Bayreuth, 95447 Bayreuth, Germany,

²Experimental Physics X, Department of Physics, University of Bayreuth, 95447 Bayreuth, Germany,

³Institute of Molecular Physics, Polish Academy of Sciences, 60-179 Poznań Poland,

⁴Institute of Physics and Center for Interdisciplinary Nanostructure Science and Technology (CINSaT), University of Kassel, 34132 Kassel, Germany

The code used to produce the numerical results for this paper is archived at zenodo [88]

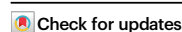


Simultaneous and independent topological control of identical microparticles in non-periodic energy landscapes

Received: 20 June 2023

Accepted: 7 November 2023

Published online: 18 November 2023



Nico C. X. Stuhlmüller¹, Farzaneh Farrokhzad², Piotr Kuświk³, Feliks Stobiecki³, Maciej Urbaniak³, Sapida Akhundzada⁴, Arno Ehresmann⁴, Thomas M. Fischer² & Daniel de las Heras¹ ✉

Topological protection ensures stability of information and particle transport against perturbations. We explore experimentally and computationally the topologically protected transport of magnetic colloids above spatially inhomogeneous magnetic patterns, revealing that transport complexity can be encoded in both the driving loop and the pattern. Complex patterns support intricate transport modes when the microparticles are subjected to simple time-periodic loops of a uniform magnetic field. We design a pattern featuring a topological defect that functions as an attractor or a repeller of microparticles, as well as a pattern that directs microparticles along a prescribed complex trajectory. Using simple patterns and complex loops, we simultaneously and independently control the motion of several identical microparticles differing only in their positions above the pattern. Combining complex patterns and complex loops we transport microparticles from unknown locations to predefined positions and then force them to follow arbitrarily complex trajectories concurrently. Our findings pave the way for new avenues in transport control and dynamic self-assembly in colloidal science.

The transport of microscopic colloidal particles suspended in fluids is relevant for a wide range of physical and biological phenomena including sedimentation¹, drug delivery^{2–4}, self-assembly^{5–7}, microfluidic devices^{8–13}, and active systems^{14–16}. External fields are often used to control the motion of colloidal particles^{17–19}. These include spatially uniform fields such as gravitational²⁰, electric²¹, and magnetic^{22–24} fields, as well as spatially inhomogeneous fields such as the manipulation of colloidal particles with optical tweezers²⁵. Directed colloidal transport can be achieved via Brownian motors^{26–28} that combine non-equilibrium fluctuations with spatially inhomogeneous energy landscapes^{29–31}.

Usually, the colloidal particles are transported along the same direction but the simultaneous transport of different particles across

different directions is useful and even a requisite in systems of various length scales. For example, the transport of cargo on traffic networks requires organizing various subtasks simultaneously³². Sorting of microparticles driven on periodic lattices is possible because the particles travel along different directions depending on, e.g. their size^{33–36}. In biology, the metabolism and structural diversity of the cell demand the regulation of a vast array of molecular traffic across intracellular and extracellular membranes.

In previous work, we have shown that robust, multidirectional, and simultaneous control of colloidal particles that differ in, e.g. their magnetic properties can be achieved with topological protection^{37,38}. As illustrated in Fig. 1a, paramagnetic particles are placed above a

¹Theoretische Physik II, Physikalisches Institut, Universität Bayreuth, D-95440 Bayreuth, Germany. ²Experimentalphysik X, Physikalisches Institut, Universität Bayreuth, D-95440 Bayreuth, Germany. ³Institute of Molecular Physics, Polish Academy of Sciences, 60-179 Poznań, Poland. ⁴Institute of Physics and Center for Interdisciplinary Nanostructure Science and Technology (CINSaT), University of Kassel, D-34132 Kassel, Germany.

✉ e-mail: delasheras.daniel@gmail.com

periodic magnetic pattern made of regions of positive and negative magnetizations normal to the pattern. A uniform external magnetic field of varying orientation drives the motion. The particles are transported following the minima of the periodic magnetic potential which results from the interplay between the complex but static field of the pattern and the simple but time-dependent uniform external field. The orientation of the magnetic field varies in time-performing loops. Hence, after one loop the orientation returns to its initial value. Loops that wind around specific orientations induce the transport of the colloidal particles by one unit cell of the magnetic pattern. During the loop, minima of the magnetic potential cross from one unit cell to the adjacent. Once the loop ends, the particle is in a position equivalent to the initial one but in a different unit cell. The motion is topologically protected in the sense that the precise shape of the loop is irrelevant. Only the set of winding numbers of the modulation loop around the specific orientations (the topological invariant) determines the transport direction. The motion is therefore robust against perturbations.

The specific orientations of the external field that are relevant to control the motion depend on both the symmetry of the pattern³⁷ (e.g. square vs. hexagonal) and the particle properties. Hence, particles with different properties, e.g. paramagnetic and diamagnetic particles above hexagonal magnetic patterns³⁹ as well as micro-rods of different lengths³⁸, can be transported in different directions independently and simultaneously using periodic patterns. However, the use of periodic patterns imposes several limitations on the transport. All particles that belong to the same topological class (e.g. identical paramagnetic particles or rods of the same length) are transported along the same direction, independently of their absolute position above the pattern as schematically represented in Fig. 1a. In addition, the location of the particles above the pattern is unknown a priori and it must be determined externally via, e.g. direct visualization via microscopy.

These limitations are overcome here using inhomogeneous (non-periodic) patterns. We make either the symmetry, Fig. 1b, or the global orientation, Fig. 1c, of the magnetic pattern dependent on the absolute position above the pattern. As a result, the specific orientations of the

external field that control the motion depend also on the space coordinate. The direction of the transport can then be locally controlled by the modulation loop of the external field and also via the local symmetry of the inhomogeneous magnetic pattern. We can imprint the complexity of the transport mainly to the pattern, and then use simple loops to generate complex transport as illustrated in Fig. 1b. Following this idea we create non-periodic patterns that transport the particles to a desired position by just repeating simple modulation loops. We also create patterns in which the colloidal particles follow arbitrarily complex trajectories driven by a simple time-periodic modulation loop. Additionally, we create simple patterns and encode the complexity of the transport in the modulation loops as sketched in Fig. 1c. This allows us to simultaneously and independently control the transport of identical colloidal particles located at different positions above the pattern. We design for example a complex modulation loop that controls the transport of 18 identical colloidal particles individually and simultaneously. Beyond its fundamental interest, our work opens a new route to control the transport in colloidal systems with potential applications in reconfigurable self-assembly^{40–43}.

Results

The plane in which the particles move (action space) splits into allowed and forbidden regions. In the allowed (forbidden) regions the stationary points of the magnetic potential are minima (saddle points). The boundaries between allowed and forbidden regions in action space are the fences. The position of the fences in control space \mathcal{C} (a sphere that represents all possible orientations of the external field) depends on the symmetry of the pattern and it determines the loops that induce colloidal transport (see Fig. 1). An extended summary of the transport in periodic patterns³⁷ is provided in Supplementary Note 1 and Supplementary Figs. 1 and 2.

Here we focus on transport in inhomogeneous patterns. Sophisticated transport modes can be achieved by adding complexity to either the patterns, the loops, or to both of them. We see examples of each type in the following sections. Details about the experiments and computer simulations are given in the “Methods” section.

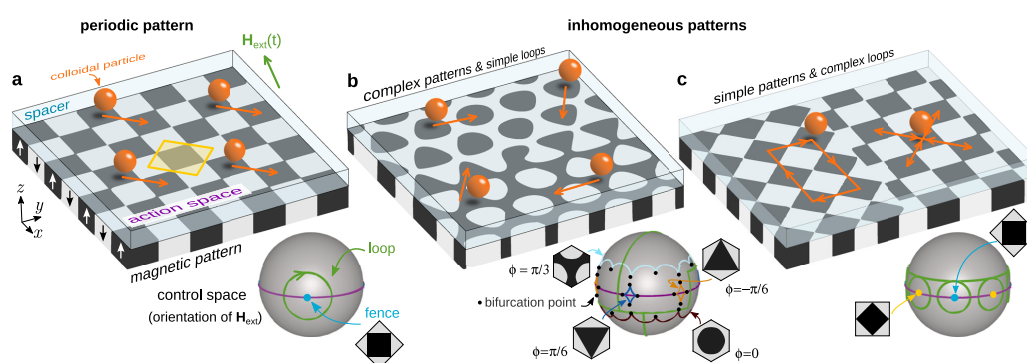


Fig. 1 | Periodic vs inhomogeneous patterns. **a** Periodic square pattern (a unit cell is highlighted in yellow), **b** hexagonal pattern in which the symmetry phase ϕ varies in space, and **c** a pattern made of two square patterns rotated by an angle of 45° . The patterns are made of regions with positive (black) and negative (white) magnetization normal to the pattern, see vertical arrows in (a). A polymer coating protects the patterns and acts as a spacer for the paramagnetic colloidal particles (orange) that are suspended in a solvent and move in a plane parallel to the pattern (action space). The motion is driven by a uniform external field (green arrow). The control space \mathcal{C} (gray spheres) represents all possible orientations of the external field. The orientation of the external field varies in time performing a loop (green curves). Loops that wind around special orientations induce particle transport. These special orientations are determined by the position of the fences and

bifurcation points in control space which depend on the local symmetry of the pattern. Shown are the fences of square patterns for one (a) and two (c) different orientations, as well as those of four hexagonal patterns with different symmetry phases ϕ (b). We also indicate the bifurcation points (black circles) in (b) which are those points where two fence segments meet. Next to the fences, we show the corresponding unit cell of the pattern. In periodic patterns (a) all the particles move in the same direction (orange arrows), independently of their position above the pattern. In inhomogeneous patterns, a single modulation loop can induce transport in different directions depending on the position of the particle above the pattern. Complex particle trajectories can be generated using complex patterns and simple loops (b) or simple patterns and complex loops (c).

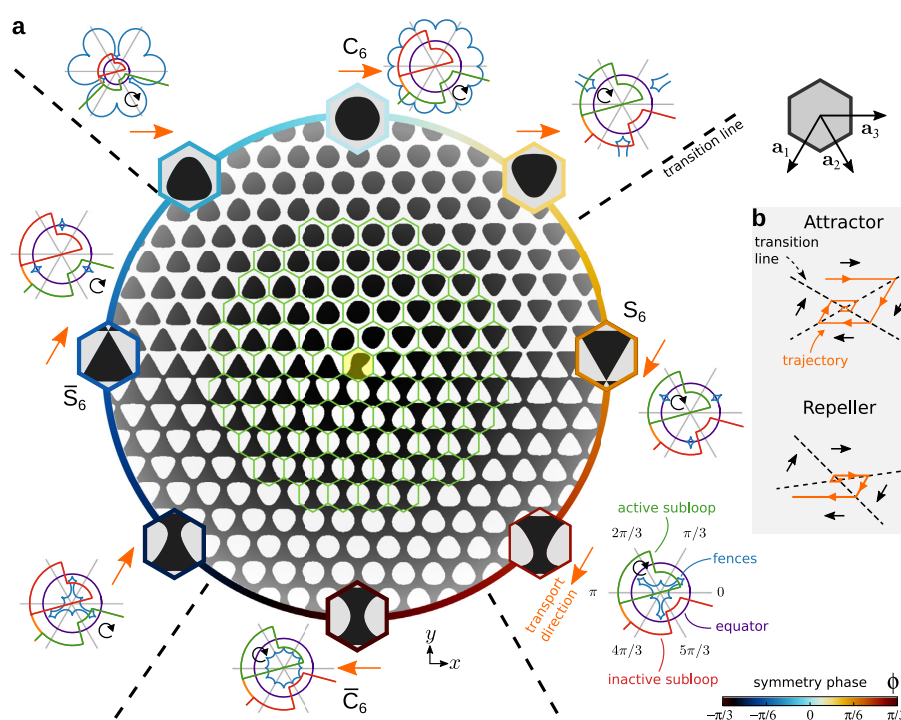


Fig. 2 | Pattern with a topological defect. **a** Magnetic pattern with a topological defect in the symmetry phase ϕ . The pattern is dissected into hexagonal cells (green hexagons). The central cell (yellow) contains the defect. Enlarged Wigner–Seitz cells of selected periodic hexagonal lattices with symmetry phase ϕ (see color bar) corresponding to their position in the pattern are shown. Next to each enlarged cell, we plot a stereographic projection of the corresponding control space and the modulation loop that attracts the particles toward the defect. Shown are the fences (blue), the equator (violet), and both the active (green) and the

inactive (red) subloops. The loop winds as indicated by the circular black arrow. The two apparently open segments of the loop are actually joined at the south pole of the control space (not visible due to the projection). The transport direction (orange arrows) changes at the transition lines (black-dashed lines). **b** Illustrative configurations of the position of transition lines (black-dashed lines) that give rise to particle trajectories moving towards the defect (attractor) or away from it (repeller). The particle trajectories are illustrated in orange.

Complex patterns and simple loops

There is a full family of periodic hexagonal patterns characterized by the value of the symmetry phase ϕ (see the “Methods” section) and illustrative examples in Fig. 1b. We render the symmetry phase a continuous function of the position, which creates an inhomogeneous symmetry phase modulated pattern such as the example in Fig. 1b. For slow enough spatial changes of the symmetry phase, the cells of the modulated pattern deviate only weakly from the Wigner–Seitz cells of corresponding periodic patterns with fixed values of the symmetry phase. Hence, knowing how to control the transport in periodic patterns is enough to control the transport in inhomogeneous situations.

We focus first on complex inhomogeneous patterns designed to achieve locally different transport for a single specific task. Most of the complexity of the transport is embedded in the pattern and therefore the modulation loops of the external field are simple.

Topological defect in the symmetry phase

We show in Fig. 2 a symmetry phase modulated hexagonal pattern. The details to generate the pattern are given in the “Methods” section. Each time we wind around the center of the pattern we go through the full family of hexagonal patterns exactly once (including the inverse patterns with opposite magnetization) and return to the initial symmetry phase. This introduces a topological defect at the center of the pattern where the symmetry phase is not well defined.

The symmetry phase is constant along radial directions and the modulation is weak everywhere except near the defect. To illustrate this, we have dissected the pattern into hexagonal cells in Fig. 2a. We also show enlarged Wigner–Seitz cells of periodic patterns with a symmetry phase corresponding to that of the radial ray of the inhomogeneous pattern. The Wigner–Seitz cells of the periodic patterns resemble closely the cells of the inhomogeneous pattern, even in the proximity of the central defect. It is therefore expected that the transport in the inhomogeneous pattern can be understood in terms of the transport in periodic patterns.

The location of the fences in the control space varies substantially as we wind around the defect in the action space. (See the stereographic projections of control space for selected values of the symmetry phase in Fig. 2a and Supplementary Fig. 1.) Hence, it is possible to transport the microparticles into different directions depending on the sector of the pattern. In particular, we can construct modulation loops that use the central defect of the pattern as either an attractor or a repeller of colloidal particles.

A stereographic projection of the modulation loop that attracts the particles towards the defect is shown in Fig. 2a next to each enlarged Wigner–Seitz cell. The loop is made of two subloops. Only one of the subloops is active (green) for each value of the symmetry phase ϕ . The subloop is active in the sense that it induces net transport for those particles located in sectors of the pattern with

that value of ϕ . The other subloop is inactive (red) in the sense that after one complete subloop, the particle returns to its position and hence there is no net transport. Using two subloops we control simultaneously the transport direction in sectors of the pattern with opposite magnetization (different values of the symmetry phase). Note for example how the active subloop in regions with C_6 symmetry ($\phi = 0$) becomes the inactive subloop in those regions with an inverse pattern \overline{C}_6 ($\phi = \pm \pi/3$) and vice versa (see Fig. 2a). To induce transport a subloop must wind around at least three bifurcation points of the fences in control space \mathcal{C} , as explained in the Supplementary Note 1. Recall that control space is simply the surface of a sphere in which each point corresponds to one orientation of the external magnetic field. The bifurcation points are the points in which two segments of the fences meet in \mathcal{C} , see examples in Supplementary Fig. 2.

The complete attractor loop, made of two subloops, induces four different transport directions (along $\pm \mathbf{a}_1$ and along $\pm \mathbf{a}_3$) depending on the value of the symmetry phase (see Fig. 2a). Here, \mathbf{a}_i , $i = 1, 2, 3$ are three lattice vectors of the periodic hexagonal pattern (see Fig. 2 and the “Methods” section). The transition between the different transport directions, e.g. from $+\mathbf{a}_3$ to $-\mathbf{a}_1$, occurs at specific values of the symmetry phase that can be adjusted with the loop. See the transition lines (dashed-black lines) in Fig. 2a.

By controlling the location of the transition lines we fix whether the defect acts as an attractor or a repeller of particles (see Fig. 2b). In both cases, the particles wind clockwise around the defect. Instead of changing the position of the transition lines, we could also control whether the defect attracts or repels microparticles by reversing the direction of the transport. However, this requires a complete redesign of the modulation loop. Simply reversing the direction of the modulation loop does not reverse in general the transport direction in the whole pattern due to the occurrence of non-time reversal ratchets in hexagonal patterns^{37,39}.

In Fig. 3a, b we show the trajectories of a colloidal particle located above the defect pattern according to Brownian dynamics simulations. The particle is randomly initialized above the pattern and then subjected to several repetitions of the attractor loop shown in Fig. 2. We also show the trajectory followed by the particle under the repetition of the repeller loop, depicted in Fig. 3c. The repeller and the attractor loops have similar shapes since they differ only in the values of ϕ at which the transport direction changes. The corresponding experimental trajectories are shown in Fig. 3d. In the experiments, there are several colloidal particles that are initially located above the pattern in random positions. If the attractor loop is repeated enough times, one colloidal particle will have reached the defect with almost certainty. Once a particle reaches the defect it stays there. In the experiments, further colloidal particles that try to enter the defect are repelled by the particle already occupying the center via dipolar repulsion. We can thus use the attractor loop to initialize one microparticle in the defect center. Whereas the location prior to the action of the attractor loop was unknown, it is known after the repeated application of the loop. The topological initialization is robust to thermal fluctuations. Brownian dynamics simulations of colloidal particles at higher temperatures still initialize the location of the defect. We briefly discuss the effect of finite temperature in the “Methods” section and Supplementary Fig. 4.

Encoding complex trajectories in the pattern

Patterns with spatial modulation of the symmetry phase can be used to encode arbitrarily complex particle trajectories. The patterns are designed to induce the desired trajectory when the particles are subjected to the repetition of a simple modulation loop of the orientation of the external field. The modulation loop transports particles along all possible directions in hexagonal patterns, i.e. along $\pm \mathbf{a}_i$ with $i = 1, 2, 3$, but in a way that only one direction is active for a given value of the symmetry phase. For example, particles on top of regions with C_6 symmetry are transported towards $-\mathbf{a}_3$. The transport direction

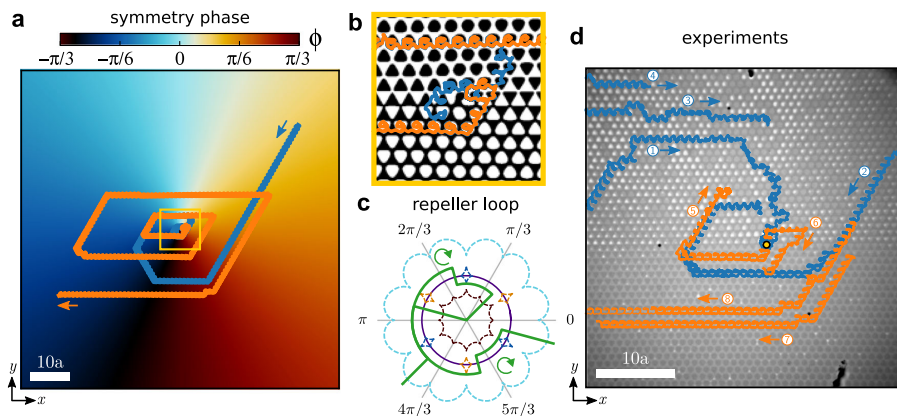


Fig. 3 | Attractor and repeller of particles. **a** Trajectory of a colloidal particle (randomly initialized) obtained with Brownian dynamics simulations above a pattern with a central topological defect in the symmetry phase. The blue (orange) trajectory is generated by the repetition of the attractor (repeller) modulation loop that moves particles towards (away from) the defect. The pattern is colored according to the value of the symmetry phase (color bar). The scale bar is $10a$. **b** Close-up of the region indicated by a yellow square in (a) and the trajectories around the central defect. The background shows the local magnetization of the pattern. **c** Stereographic projection of the repeller loop (green) in \mathcal{C} . The equator (violet circle) and the fences of the C_6 and S_6 patterns as well as their inverse patterns, \overline{C}_6 and \overline{S}_6 , (dashed curves) are also depicted as a reference. The fences are colored according to the value of the symmetry phase. The two apparently open

segments of the loop are actually joined at the south pole of the control space (not visible due to the projection). The loop is made of two subloops winding clockwise, as indicated by the circular arrows. **d** Experimental trajectories of several colloidal particles (labeled with a numbered circle) above the same pattern with a topological defect (yellow circle). The trajectories induced by the attractor (repeller) loop are colored in blue (orange). Blue and orange trajectories correspond to different experiments and have been superimposed in the figure. Note that under the microscope regions with negative magnetization appear darker than regions with positive magnetization, i.e. the opposite of our color choice in e.g. (b). The scale bar is $10a$ and the lattice constant of one cell is approx. $14 \mu\text{m}$. Movies of the simulated and the experimental motion are provided in Supplementary Movie 1.

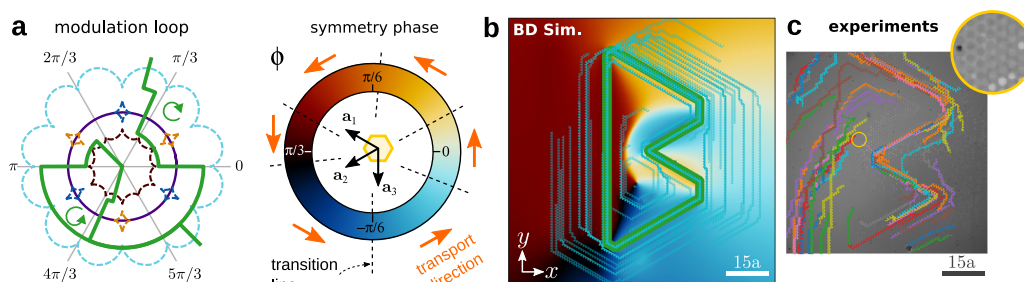


Fig. 4 | Symmetry phase modulated pattern. **a** Stereographic projection of control space showing the equator (violet circle), the closed modulation loop (green-solid curve), and the fences of patterns with C_6 , S_6 , \overline{C}_6 and \overline{S}_6 symmetries (dashed curves). The two apparently open segments of the loop are actually joined at the south pole of the control space (not visible due to the projection). The fences are colored according to the value of the symmetry phase (see the annular color bar). The transport directions induced by the loop (orange arrows) change at specific values of the symmetry phase ϕ as indicated by the transition lines (black-dashed lines). **b** Symmetry phase modulated pattern (the color indicates the value of the symmetry phase). A global rotation, $\psi = \pi/2$ in Eq. (6), makes one transport direction (lattice vector \mathbf{a}_3) parallel to the vertical axis. Particles above the pattern and subjected to the repetition of the modulation loop in (a) write the letter "B".

Thin cyan lines show simulated particle trajectories for randomly initialized particles above the pattern. After several repetitions of the modulation loop, most particles enter the stable trajectory, highlighted with a thick green-solid line. **c** Experimental trajectories of colloidal particles above the pattern depicted in (b) and subjected to the modulation loop shown in (a). The region shown in the experiments (c) is smaller than that in simulations (b) due to the field of view of the microscope. The inset in (c) is a close view of the region indicated with a yellow circle in which we have altered the contrast of the image to better visualize the magnetization. Under the microscope regions with negative magnetization appear darker than those with positive magnetization. A colloidal particle (black dot) is also visible in the inset. A movie of the motion in simulations and experiments is provided in Supplementary Movie 2.

changes at specific values of the symmetry phase determined by the modulation loop. In Fig. 4a we show the modulation loop together with the representative fences and the resulting transport direction for each value of the symmetry phase.

The detailed procedure to generate the patterns is described in the "Methods" section and Supplementary Fig. 3. In essence, we first draw the trajectories that the particles should follow by hand. Then, at each position along the trajectory, we encode the transport direction using the value of the symmetry phase. Finally, the value of the symmetry phase at each point in the complete pattern is calculated as a spatially resolved weighted average of the symmetry phase along the trajectory. As a result, the symmetry phase varies smoothly across the pattern except for the occurrence of string-like topological defects in the symmetry phase.

Figure 4b shows a symmetry phase modulated pattern together with the corresponding simulated particle trajectories. The value of the symmetry phase is color-coded (see color bar). The pattern is designed to transport the particles along one stable trajectory that forms a closed loop resembling the letter "B". In Fig. 4b we have highlighted the stable trajectory with a thick green line. Most particles above the pattern either enter the stable trajectory or leave the pattern. Occasionally one particle gets stuck in specific regions of the pattern. This can potentially be avoided by the introduction of random fluctuations in the modulation loop. In the presence of strong Brownian motion, the stable trajectories broaden to a width of a few unit cells, and additional stable trajectories might occur.

Corresponding experimental trajectories are shown in Fig. 4c. Even though the agreement is not perfect, the experimental trajectories follow closely the prescribed letter "B", demonstrating, therefore, the potential of the method. Small variations in the position of the fences due to the imperfections of the pattern are likely the reason behind the deviations shown in the experiments. Fine-tuning the modulation loop and the height of the particles above the pattern would likely improve the results.

Simple patterns and complex loops

We follow now the opposite approach by encoding the complexity in the modulation loop. We create simple inhomogeneous patterns by

concatenating large patches of periodic square patterns. The patches differ in the global orientation of the lattice vectors given by a global phase ψ (see the "Methods" section). Each (simple) patch allows for a rich variety of transport tasks. The task in each patch can be controlled individually and simultaneously using rather complex modulation loops in control space.

The fences of the C_4 square pattern are four equidistant points on the equator (see Supplementary Note 1). The four fence points in C correspond to external fields pointing along the positive and negative directions of the lattice vectors^{37,44}, i.e. along $\pm\mathbf{a}_1$ and $\pm\mathbf{a}_2$. Therefore, rotating the lattice vectors also rotates the position of the fences in control space. Thus, it is possible to construct loops that wind around different fences in C , and hence induce different transport directions, depending on the orientation of the pattern ψ . An illustration is shown in Fig. 5a.

Since the fences are points in C it is in principle possible to concatenate an arbitrarily large number of patches with different orientations and control the motion in each of them independently. In practice, limiting factors might appear due to e.g. imperfections in the patterns that effectively make the fences in C extended regions, the angular resolution with which the orientation of the external field can be controlled, and the presence of Brownian motion. Due to the limiting factors, two patterns can be resolved independently if they are rotated by an angle of at least $\Delta\psi$. Hence, the maximum number of patches that can be controlled independently is $(\pi/2)/\Delta\psi$ since after a rotation of $\pi/2$ a C_4 pattern repeats itself (and so do the fences).

With a resolution $\Delta\psi = 5^\circ$ it is then possible to control the motion in up to 18 patches independently. As an example we program a single loop in C that writes the first eighteen letters of the alphabet simultaneously, (see Fig. 5b and Supplementary Movie 3). Note that the letters are rotated by an angle ψ . For simplicity, we have designed an algorithm to write custom trajectories in a square pattern with global orientation $\psi = 0$. Next, we apply a global rotation to the modulation loop to control the transport in patterns with a generic orientation ψ . As a result, the trajectories are also rotated.

The loop that writes the first 18 letters of the alphabet contains 2086 simple commands. Each command is a small closed subloop that

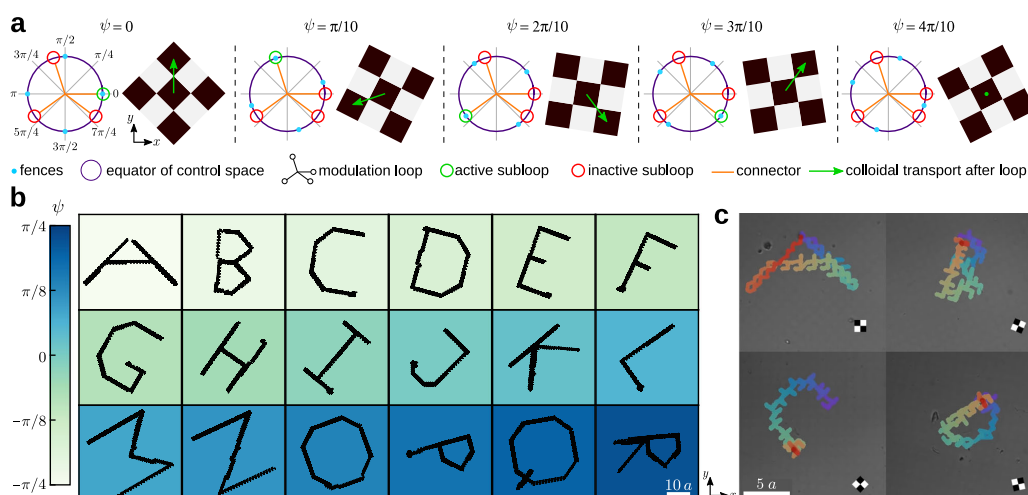


Fig. 5 | Simple patterns and complex loops. **a** Five square magnetic patterns (and their corresponding control spaces) with a different value of the global orientation ψ , as indicated. The fences in **C** (blue circles) are four points located on the equator (violet circle). The position of the fences depends on the value of ψ . The modulation loop consists of four interconnected subloops that wind counterclockwise. A subloop is active (green) if it winds around a fence point (blue circles) and inactive (red) otherwise. The orange segments of the modulation loop simply connect the different subloops. Depending on the value of ψ , the modulation loop induces different transport directions (green arrows) or no transport at all. **b** A pattern made of 18 patches with square symmetry and different global orientation ψ (color bar). A modulation loop controls the trajectories of particles above each patch

simultaneously and independently. The particle trajectories (black) write the first 18 letters of the alphabet. The length of the scale bar is $10a$. A movie can be found in Supplementary Movie 3. **c** Experimental trajectories of colloidal particles above four square patches rotated with respect to each other. A schematic unit cell illustrating the global orientation is depicted in each patch. The length of the scale bar is $5a$ and in this case, we use patterns with $a = 7 \mu\text{m}$. A unique modulation loop transports the four colloidal particles simultaneously. The trajectories are colored according to the time evolution from blue (initial time) to red (final time). A movie showing the whole time evolution and a one-to-one comparison with computer simulations is available in Supplementary Movie 4.

either transports a particle in one unit cell along the four possible directions of the square lattice or leaves the particle in the same position, similar to the loops in Fig. 5a. Even though an angular resolution of $\Delta\psi = 5^\circ$ is achievable experimentally, the number of commands required by the complete loop exceeds our current experimental capabilities. Nevertheless, we show in Fig. 5c, the experimental trajectories of a simplified loop that writes low-resolution versions of the first four letters of the alphabet. The loop is made of 96 simple commands. The agreement with computer simulations is essentially perfect, as we demonstrate in a one-to-one comparison in Supplementary Movie 4.

The simultaneous control of the transport in several patches of rotated square patterns is particularly simple due to the simplicity of the fences in **C**. However, the same ideas apply to patterns with other symmetry classes.

Here, we have initialized the particles in the desired positions within their respective patches. As we discuss now, it is possible to automatize this process by combining the patches with complex patterns.

Complex patterns and complex loops

Complete control over the colloidal transport is achieved by combining complex patterns and complex loops. In Fig. 6 we combine three C_4 patches that differ in their global orientation ψ and three hexagonal patterns with a topological defect in the symmetry phase. The transition between both patterns occurs smoothly within a region of length equivalent to approximately five unit cells of the square patterns.

We first make use of the patterns with a topological defect to move randomly placed particles toward the defects. We simply repeat the attractor modulation loop shown in Fig. 2 several times such that the particles move and stay at the defects, see the blue trajectories of

the particles in Fig. 6. Once this initialization stage is finished we know the precise position of the particles and can control them independently. Using two simple loops we transport the particles downwards from the defects to the square patches. We use one loop to move the particles in the defect pattern (orange trajectories) and another loop to move the particles in the transition region and the square patches (green trajectories). Then, a relatively complex loop controls the motion of the three particles independently. Each particle follows a complex trajectory drawing either a square, a triangle, or a cross depending on the value of the global orientation ψ (red trajectories). Experimentally we tested each part of the loop separately, as shown in the insets of Fig. 6. Again, the agreement between simulations and experiments is excellent. The small errors that occur in the experimental trajectories, likely due to imperfections in the pattern, do not affect the global shape of the trajectories. A movie of the whole process is shown in Supplementary Movie 5.

Discussion

We have shown that the combination of a complex static magnetic field with a simple time-dependent uniform external field of varying orientation allows us to control the motion of several identical microparticles independently and simultaneously. The transport complexity can be broken down to a finite set of special orientations of the external field. A modulation loop that winds around one of those orientations induces transport along a known direction in a known region of the pattern. The motion is topologically protected since only the winding numbers of the modulation loop around the special orientations (topological invariant) are important. Hence, it is relatively simple to generate loops and patterns that induce arbitrarily complex trajectories. Our ideas might be transferable to other systems

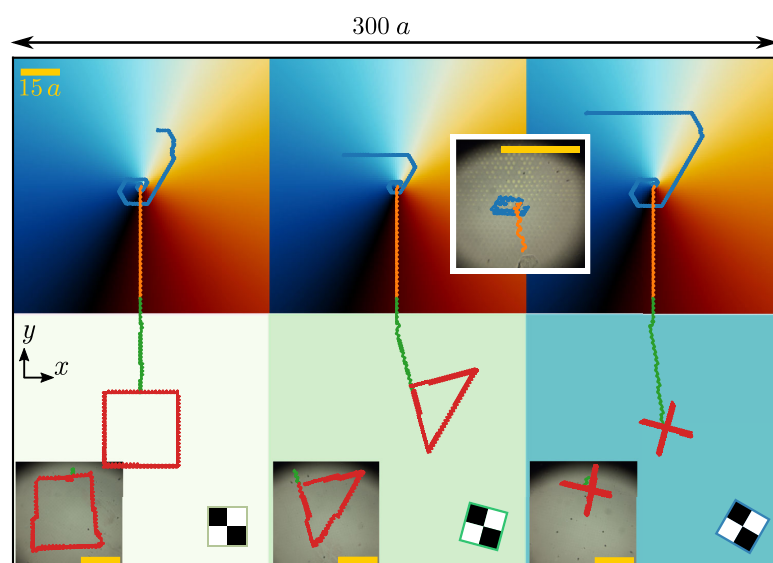


Fig. 6 | Complex patterns and complex loops. Brownian dynamics simulations of the transport of colloidal particles above a complex pattern made of three patches, each one with a topological defect in the symmetry phase (top) connected to three patches with square symmetry (down) rotated with respect to each other. The color of the patches with topological defects indicates the value of the symmetry phase ϕ . The color of the square patches indicates the global rotation ψ , illustrated with a sketch of the magnetization. A unique complex modulation loop made of four parts drives the transport in the whole system. In the first part, the repetition of the

attractor loop moves the particles toward the defects (blue trajectories) and lets them wait there. The second part of the loop moves the particles downwards through the patterns with defects (orange trajectories). The third part of the loop moves the particles downwards in the square patterns (green trajectories). The last part of the loop writes a custom trajectory (square, triangle, and cross) depending on the global orientation ψ of the pattern (red trajectories). Insets show the corresponding experimental trajectories. The length of the scale bars (yellow) is $15a$.

in which the transport is also based on topological protection. These include, solitons⁴⁵, nano-machines^{46,47}, sound waves^{48,49}, photons^{50,51}, and quantum mechanical excitations⁵².

The complexity of the transport is encoded in the magnetic potential which varies in space and in time via the magnetic patterns and the modulation loops, respectively. An alternative approach that encodes the transport in the particle shape has appeared recently⁵³. There, Sobolev et al. find the shape of the rigid body that traces the desired trajectory when rolling down a slope. We have restricted our study to identical isotropic paramagnetic particles. However, as discussed in the “Introduction” section, colloidal particles with different characteristics (e.g. diamagnetic and paramagnetic particles or particles with different shapes) might belong to different topological classes. The fences of particles belonging to different topological classes are located in different regions in C . Above non-periodic patterns, the control space of particles belonging to different topological classes will also depend on the space coordinate. A precise control over the transport depending not only on the position but also on the particle characteristics is then possible. Therefore, beyond offering the possibility to control the transport of identical microparticles simultaneously, our work also opens a new route towards dynamical self-assembly in colloidal science. As an example, we have created a colloidal rod factory⁵⁴ in which identical isotropic particles are transported toward a reaction site in which they self-assemble. Only when they reach the desired aspect ratio, do the rods leave the polymerization site following the desired trajectory. The use of patchy colloids^{55–58} with, e.g. hybridization of complementary DNA strands^{59–61} and other shape-anisotropic particles^{62,63} would offer more versatility to create complex functional structures.

We have considered transport above patterns made of identical patches rotated with respect to each other. It is also possible to combine patches of patterns with different symmetries provided that their respective fences do not overlap in control space. Moreover, a combination of both, i.e. a pattern made of patches with different symmetries, e.g. C_4 and C_6 , that in addition are rotated with respect to each other would substantially increase the number of tasks that can be done simultaneously since their respective fences in control space do not overlap.

In the experiments, the Brownian motion of the colloidal particles is negligible but it might play a role in other systems with smaller colloids and/or at higher temperatures. Since the transport is topologically protected, it is robust against perturbations such as the presence of Brownian motion¹⁴. If we make Brownian motion more prominent (e.g. by increasing the temperature or reducing the particle size) the particles start to deviate from the expected trajectories but overall the transport is robust. An example of Brownian dynamics simulations at different temperatures is shown in Supplementary Fig. 4. The topological protection will disappear due to Brownian motion at sufficiently high temperatures and for small enough particles. A possible solution would then be to increase the magnitude of either the pattern field or the external magnetic field such that the magnetic forces dominate again the transport.

Our systems are very dilute and therefore direct interparticle interactions and hydrodynamic interactions do not play any role. However, it would be interesting to look at the effect of both super-adiabatic forces⁶⁴ and long-range hydrodynamic interactions⁶⁵ in denser systems.

Methods

System setup and computer simulations

Identical paramagnetic colloidal particles immersed in a solvent are located above a magnetic pattern and are restricted to move in a plane parallel to the pattern (xy -plane), which we call action space \mathcal{A} (Fig. 1a). The pattern contains regions of positive, $+m_p$, and negative, $-m_p$, uniform magnetization along the z -direction (normal to the pattern). The width of the domain walls between oppositely magnetized regions is negligible. The particles are driven by a time- and space-dependent external magnetic potential $V_{\text{mag}}(\mathbf{r}_A, t)$. The potential is generated by the static but space-dependent magnetic field of the pattern $\mathbf{H}_p(\mathbf{r}_A)$ and a time-dependent but spatially homogeneous external magnetic field $\mathbf{H}_{\text{ext}}(t)$. Here \mathbf{r}_A is the space coordinate in action space and t denotes the time. The magnitude of the external field (constant) is much larger than that of the pattern field, i.e. $H_{\text{ext}} \gg H_p(\mathbf{r}_A)$ for any position in \mathcal{A} . Hence, the magnetic potential, which is proportional to the square of the total magnetic field $V_{\text{mag}} \propto -(\mathbf{H}_{\text{ext}} + \mathbf{H}_p) \cdot (\mathbf{H}_{\text{ext}} + \mathbf{H}_p)$, is dominated by the coupling between the external and the pattern fields:

$$V_{\text{mag}}(\mathbf{r}_A, t) \approx -\nu_0 \chi \mu_0 \mathbf{H}_p(\mathbf{r}_A) \cdot \mathbf{H}_{\text{ext}}(t). \quad (1)$$

Here μ_0 is the vacuum permeability, χ is the magnetic susceptibility of the colloidal particle, and ν_0 is the particle volume³⁷. We have omitted the term proportional to $\mathbf{H}_{\text{ext}} \cdot \mathbf{H}_{\text{ext}}$ in V_{mag} since it is just a constant and therefore it does not affect the motion.

In the overdamped limit, the equation of motion of one particle reads

$$\gamma \dot{\mathbf{r}}_A = -\nabla_A V_{\text{mag}} + \boldsymbol{\eta}, \quad (2)$$

where γ is the friction coefficient against the implicit solvent, the overdamped time derivative, ∇_A is the derivative with respect to \mathbf{r}_A , and $\boldsymbol{\eta}$ is a delta-correlated Gaussian random force with zero mean that models the effect of the collisions between the molecules of the solvent and the colloidal particle (Brownian motion). We define our energy scale ε as the absolute value of the average external energy that a particle would have when the external magnetic field points normal to the pattern. Hence, absolute temperature T is given in reduced units $k_B T / \varepsilon$ where k_B is the Boltzmann's constant. We use the magnitude of a lattice vector of the periodic pattern a as the length scale. The timescale is hence given by $\tau = \gamma a^2 / \varepsilon$. We use adaptive Brownian dynamics⁶⁶ to efficiently integrate the equation of motion. In the experiments, the magnetic forces strongly dominate over the random forces. Hence, random forces do not play any role. We use Brownian dynamics simulations due to the overdamped character of the motion in the viscous aqueous solvent. The code to simulate the colloidal motion and to generate the modulation loops is available via Zenodo⁶⁷.

As the external magnetic field is homogeneous in space, it can be solely described by its orientation. The set of all possible orientations of \mathbf{H}_{ext} forms a spherical surface that we call control space \mathcal{C} . A point in \mathcal{C} indicates an orientation of \mathbf{H}_{ext} . We drive the colloidal motion by performing closed loops of the orientation of \mathbf{H}_{ext} in \mathcal{C} . Loops that wind around specific points in \mathcal{C} induce colloidal motion. That is, once the loop returns to its initial position, the colloidal particle has moved to a different unit cell of the pattern. The transport is topologically protected since the precise form of the loop is irrelevant. Only the winding numbers of the loop around the specific points in \mathcal{C} (which are the topological invariants) determine the transport.

Experiments

The magnetic films with the desired patterns imprinted are thin Co/Au multilayers with perpendicular magnetic anisotropy⁶⁸ lithographically patterned via a home-built⁶⁹ keV-He-ion bombardment⁷⁰. Further details about the fabrication process can be found in refs. 37,71–73.

The patterns have lattice vectors of magnitude $14 \mu\text{m}$ if not stated otherwise.

To reduce the influence of lateral magnetic field fluctuations due to the fabrication procedure (which increases near the substrate) we coat the magnetic pattern with a photo-resist film (thickness $1.6 \mu\text{m}$). The coating layer serves other two purposes: it protects the patterns and it acts as a spacer between the colloidal particles and the pattern (see Fig. 1), in order to secure the condition $|\mathbf{H}_{\text{ext}}| \gg |\mathbf{H}_p|$. We then place paramagnetic colloids of diameter $2.8 \mu\text{m}$ immersed in deionized water on top of the pattern. The microparticles sediment and are suspended roughly the Debye length above the negatively charged coating layer on the pattern. The motion above the pattern is effectively two-dimensional.

The uniform external magnetic field is generated with three coils arranged around the pattern and controlled with a computer. The magnitude of the external field is approximately $4 \times 10^3 \text{ A/m}$. Standard reflection microscopy techniques are used to visualize both the colloids and the pattern.

Square and hexagonal periodic patterns

Consider magnetic periodic N -fold symmetric patterns with either $N=2$ (square patterns) or $N=3$ (hexagonal patterns). Examples of both types are shown in Supplementary Fig. 1. In the limit of an infinitely thin pattern located at $z=0$, the magnetization is

$$\mathbf{M}(\mathbf{r}) = M(\mathbf{r}_\perp) \delta(z) \hat{\mathbf{e}}_z, \quad (3)$$

with $\delta(\cdot)$ the Dirac distribution, $\hat{\mathbf{e}}_z$ the unit vector normal to the pattern, $\mathbf{r}_\perp = (x, y)$, and

$$M(\mathbf{r}_\perp) = m_p \text{sign} \left(\sum_{i=1}^N \cos(\mathbf{q}_i \cdot (\mathbf{r}_\perp - \mathbf{b}) - \phi) + m_0(\phi) \right), \quad (4)$$

where m_p is the saturation magnetization of the domains. The wave vectors \mathbf{q}_i in the square patterns are

$$\mathbf{q}_i = q_0 \begin{pmatrix} -\sin(\pi i/2 - \psi) \\ \cos(\pi i/2 - \psi) \end{pmatrix}, \quad i=1,2 \quad (5)$$

with magnitude $q_0 = 2\pi/a$ and a being the magnitude of a lattice vector, which in square patterns can be defined with the wave vectors being the reciprocal lattice vectors. That is, $\mathbf{a}_i \cdot \mathbf{q}_j = 2\pi \delta_{ij}$ (see Supplementary Fig. 1b). The global phase ψ sets the orientation of the lattice vectors with respect to a fixed laboratory frame.

In the hexagonal patterns, the wave vectors are

$$\mathbf{q}_i = q_0 \begin{pmatrix} -\sin(2\pi i/3 - \psi) \\ \cos(2\pi i/3 - \psi) \end{pmatrix}, \quad i=1,2,3 \quad (6)$$

with magnitude $q_0 = 4\pi/(a\sqrt{3})$. Here, the three wave vectors can be related to three (linearly dependent) lattice vectors via $\mathbf{q}_i \cdot \mathbf{a}_j = 2\pi \delta_{ij}$ for $i=1,2$ and $\mathbf{a}_3 \cdot \mathbf{q}_3 = 0$ (see Supplementary Fig. 1b).

In both square and hexagonal patterns, the wave vectors point into the N different symmetry directions. The translational vector \mathbf{b} in Eq. (4) plays a relevant role only in inhomogeneous patterns. In periodic patterns, we usually set $\mathbf{b} = \mathbf{0}$.

In square patterns, the symmetry phase ϕ in the magnetization (see Eq. (4)), simply causes a trivial shift of all Wigner–Seitz cells with respect to the origin of the pattern. Hence, for simplicity, we set it to zero. In hexagonal patterns however, the symmetry phase ϕ has a non-trivial effect since it determines the point symmetry of the pattern (see Supplementary Fig. 1c), and therefore the modulation loops required to transport the colloidal particles³⁷. The Wigner–Seitz cell of a hexagonal pattern contains in general three symmetry points with C_3 symmetry (rotation through an angle $2\pi/3$ about the symmetry axis). For special values of the symmetry phase, one of the three-fold

symmetric points acquires a higher symmetry; either six-fold hexagonal C_6 symmetry (for $\phi = 0$ and $\phi = \pm \pi/3$) or S_6 symmetry, i.e. a C_6 followed by a perpendicular reflection (for $\phi = \pm \pi/6$).

Finally, the parameter m_0 in Eq. (4), which is actually a function of the symmetry phase ϕ , alters the area ratio between up-magnetized and down-magnetized domains. Following Loehr et al.³⁷, we use here $m_0(\phi) = \frac{1}{2} \cos(3\phi) \delta_{N,3}$ (therefore in square patterns $m_0 = 0$) to ensure that the average magnetization in hexagonal patterns is very small, i.e.

$$\int M(\mathbf{r}_\perp) d\mathbf{r}_\perp \approx 0. \quad (7)$$

Magnetic field of the pattern

To numerically compute the magnetic field of the pattern, $\mathbf{H}_p(\mathbf{r})$, at the desired position in action space we first discretize the pattern in a square grid with resolution $0.03a$ and compute the magnetization at the grid points via Eq. (4). Next, we compute the magnetic field at the grid points by convolution of the magnetization with the Green's function of the system:

$$\mathbf{H}_p(\mathbf{r}) = \mathbf{H}_p(\mathbf{r}_\perp, z) = \frac{1}{4\pi} \int d\mathbf{r}'_\perp \frac{\mathbf{r}_\perp - \mathbf{r}'_\perp + z\hat{\mathbf{e}}_z}{|\mathbf{r}_\perp - \mathbf{r}'_\perp + z\hat{\mathbf{e}}_z|^3} M(\mathbf{r}'_\perp). \quad (8)$$

Here $\mathbf{r}_\perp = (x, y)$ is the position coordinate in a plane parallel to the pattern. We calculate the magnetic field at an elevation above the pattern $z = 0.5a$, which is comparable to the experimental value. As usual, we perform the convolution in Fourier space.

To calculate the magnetic field at a generic, off-grid, position we simply interpolate the magnetic field using bicubic splines.

Pattern with a topological defect

For the pattern with a topological defect shown in Fig. 2, the symmetry phase varies with the position \mathbf{r}_\perp as

$$\phi(\mathbf{r}_\perp) = \frac{1}{3} \left(\frac{\pi}{2} - \arctan(\mathbf{q}_3 \cdot \mathbf{r}_\perp \hat{\mathbf{e}}_z \cdot (\mathbf{r}_\perp \times \mathbf{q}_3)) \right), \quad (9)$$

and the global orientational phase is set to $\psi = 0$ in Eq. (6). For our choice of wave vectors (see Eq. (6) and Supplementary Fig. 1b), the symmetry phase modulation is simply $\phi(\mathbf{r}_\perp) = (\pi/2 - \arctan(x, y))/3$. Here $\arctan(y, x)$ returns the four-quadrant inverse tangent of y/x . The symmetry phase varies therefore between $\phi = -\pi/3$ and $\pi/3$ as we wind once around the origin. The topological charge of the defect located at the center of the pattern ($\mathbf{r}_\perp = 0$) is $q = \Delta\phi/(2\pi/p) = 1$. Here $\Delta\phi = 2\pi/3$ is the angle that the director rotates if we wind once counter-clockwise around the defect, and $p = 3$ is the p -atic symmetry of the director field⁷⁴. (The symmetry phase can be described with a 3-atic director field for which the local orientations are defined modulo $\pi/3$.) Varying the symmetry phase between $-\pi/3$ and $\pi/3$ also introduces a shift of the unit cell, cf. the unit cells for $\phi = \pi/3$ and $-\pi/3$ in Supplementary Fig. 1c. To rectify this shift and avoid therefore discontinuities in the magnetization of the pattern, we need to use a local shift vector in Eq. (4) given by

$$\mathbf{b}(\mathbf{r}_\perp) = -(\mathbf{a}_1 + \mathbf{a}_2) \frac{\phi(\mathbf{r}_\perp)}{2\pi}. \quad (10)$$

The shift vector can be understood as a Burgers vector since it corrects for the spatial distortion of the pattern around the defect.

Symmetry phase modulated patterns

To encode in the pattern the desired particle trajectories, we use the drawing software Krita⁷⁵. We prescribe the stable trajectory on a square image with a side-length of 1000 pixels. In Krita, we draw the desired

trajectory with a brush (thickness 1 pixel) that encodes the drawing direction in the hue of the colored pixels. The drawing direction directly translates into the transport direction that the particles will follow above the pattern. This procedure results in an image that is essentially empty except for the trajectory lines. We then map from hue to the symmetry phase ϕ . An example of the pattern at this stage is shown in Supplementary Fig. 3a. The mapping from hue to ϕ is simply a linear transformation.

Next, we give a value to the symmetry phase everywhere in the pattern. To calculate the phase at a generic position $\mathbf{r}_\perp = (x, y)$ we average over all the prescribed phases along the trajectories. Each phase along the trajectory is weighted with a weight function proportional to $1/r_d^2$, with r_d the distance between \mathbf{r}_\perp and a point on the trajectory. Special care needs to be taken due to the periodicity of the symmetry phase⁷⁶. We first transform the phases along the trajectories into unit vectors, next we average the vectors, and then transform back the averaged vector into a value of the symmetry phase. An illustration of the pattern after this stage is shown in Supplementary Fig. 3b. Finally, we use the value of the symmetry phase in the whole pattern to calculate the magnetization via Eq. (4) (see Supplementary Fig. 3c).

Data availability

The code to simulate the system and to generate the modulation loops is available at Zenodo⁶⁷. All other data supporting the findings are available from the corresponding author upon request.

Code availability

A code to perform the adaptive Brownian Dynamics simulations of the colloidal particles as well as to generate the modulation loops is available at Zenodo⁶⁷.

References

- Royall, C. P., Dzubiella, J., Schmidt, M. & van Blaaderen, A. Nonequilibrium sedimentation of colloids on the particle scale. *Phys. Rev. Lett.* **98**, 188304 (2007).
- Yang, L. & Alexandridis, P. Physicochemical aspects of drug delivery and release from polymer-based colloids. *Curr. Opin. Colloid Interface Sci.* **5**, 132–143 (2000).
- Boyd, B. J. Past and future evolution in colloidal drug delivery systems. *Expert Opin. Drug Deliv.* **5**, 69–85 (2007).
- Beija, M., Salvayre, R., de Viguier, N. L. & Marty, J.-D. Colloidal systems for drug delivery: from design to therapy. *Trends Biotechnol.* **30**, 485–496 (2012).
- McGorty, R., Fung, J., Kaz, D. & Manoharan, V. N. Colloidal self-assembly at an interface. *Mater. Today* **13**, 34–42 (2010).
- Mallory, S. A., Valeriani, C. & Cacciuto, A. An active approach to colloidal self-assembly. *Annu. Rev. Phys. Chem.* **69**, 59–79 (2018).
- Dijkstra, M. & Luijten, E. From predictive modelling to machine learning and reverse engineering of colloidal self-assembly. *Nat. Mater.* **20**, 762–773 (2021).
- Terray, A., Oakey, J. & Marr, D. W. M. Microfluidic control using colloidal devices. *Science* **296**, 1841–1844 (2002).
- Holzinger, D., Lengemann, D., Göllner, F., Engel, D. & Ehresmann, A. Controlled movement of superparamagnetic bead rows for microfluid mixing. *Appl. Phys. Lett.* **100**, 153504 (2012).
- Lim, B. et al. Magnetophoretic circuits for digital control of single particles and cells. *Nat. Commun.* **5**, 3846 (2014).
- Wang, L. & Wang, J. Self-assembly of colloids based on microfluidics. *Nanoscale* **11**, 16708–16722 (2019).
- Shin, S. Diffusiophoretic separation of colloids in microfluidic flows. *Phys. Fluids* **32**, 101302 (2020).
- Abedini-Nassab, R., Sadeghdelouei, N. & Shields IV, C. W. Magnetophoretic circuits: a review of device designs and implementation for precise single-cell manipulation. *Anal. Chim. Acta* **1272**, 341425 (2023).

14. Koumakis, N., Maggi, C. & Leonardo, R. D. Directed transport of active particles over asymmetric energy barriers. *Soft Matter* **10**, 5695–5701 (2014).
15. Schakenraad, K. et al. Topotaxis of active Brownian particles. *Phys. Rev. E* **101**, 032602 (2020).
16. Martinez, R., Alarcon, F., Aragonés, J. L. & Valeriani, C. Trapping flocking particles with asymmetric obstacles. *Soft Matter* **16**, 4739–4745 (2020).
17. Löwen, H. Colloidal soft matter under external control. *J. Phys.: Condens. Matter* **13**, R415–R432 (2001).
18. Erbe, A., Zientara, M., Baraban, L., Kreidler, C. & Leiderer, P. Various driving mechanisms for generating motion of colloidal particles. *J. Phys.: Condens. Matter* **20**, 404215 (2008).
19. Reichhardt, C. & Reichhardt, C. J. O. Depinning and nonequilibrium dynamic phases of particle assemblies driven over random and ordered substrates: a review. *Rep. Prog. Phys.* **80**, 026501 (2016).
20. Köppl, M., Henseler, P., Erbe, A., Nielaba, P. & Leiderer, P. Layer reduction in driven 2D-colloidal systems through microchannels. *Phys. Rev. Lett.* **97**, 208302 (2006).
21. Vissers, T. et al. Lane formation in driven mixtures of oppositely charged colloids. *Soft Matter* **7**, 2352–2356 (2011).
22. Li, P., Kilinc, D., Ran, Y.-F. & Lee, G. U. Flow enhanced non-linear magnetophoretic separation of beads based on magnetic susceptibility. *Lab Chip* **13**, 4400–4408 (2013).
23. Holzinger, D., Koch, I., Burgard, S. & Ehresmann, A. Directed magnetic particle transport above artificial magnetic domains due to dynamic magnetic potential energy landscape transformation. *ACS Nano* **9**, 7323–7331 (2015).
24. Tierno, P., Golestanian, R., Pagonabarraga, I. & Sagués, F. Controlled swimming in confined fluids of magnetically actuated colloidal rotors. *Phys. Rev. Lett.* **101**, 218304 (2008).
25. Ashkin, A., Dziedzic, J. M., Bjorkholm, J. E. & Chu, S. Observation of a single-beam gradient force optical trap for dielectric particles. *Opt. Lett.* **11**, 288–290 (1986).
26. Magnasco, M. O. Forced thermal ratchets. *Phys. Rev. Lett.* **71**, 1477–1481 (1993).
27. Faucheux, L. P., Bourdieu, L. S., Kaplan, P. D. & Libchaber, A. J. Optical thermal ratchet. *Phys. Rev. Lett.* **74**, 1504–1507 (1995).
28. Hänggi, P. & Marchesoni, F. Artificial Brownian motors: controlling transport on the nanoscale. *Rev. Mod. Phys.* **81**, 387–442 (2009).
29. Matthias, S. & Müller, F. Asymmetric pores in a silicon membrane acting as massively parallel Brownian ratchets. *Nature* **424**, 53–57 (2003).
30. Lee, S.-H., Ladavac, K., Polin, M. & Grier, D. G. Observation of flux reversal in a symmetric optical thermal ratchet. *Phys. Rev. Lett.* **94**, 110601 (2005).
31. Skaug, M. J., Schwemmer, C., Fringes, S., Rawlings, C. D. & Knoll, A. W. Nanofluidic rocking Brownian motors. *Science* **359**, 1505–1508 (2018).
32. Anderluh, A., Hemmelmayr, V. C. & Nolz, P. C. Synchronizing vans and cargo bikes in a city distribution network. *Cent. Eur. J. Oper. Res.* **25**, 345–376 (2016).
33. Korda, P. T., Taylor, M. B. & Grier, D. G. Kinetically locked-in colloidal transport in an array of optical tweezers. *Phys. Rev. Lett.* **89**, 128301 (2002).
34. MacDonald, M. P., Spalding, G. C. & Dholakia, K. Microfluidic sorting in an optical lattice. *Nature* **426**, 421–424 (2003).
35. Ladavac, K., Kasza, K. & Grier, D. G. Sorting mesoscopic objects with periodic potential landscapes: optical fractionation. *Phys. Rev. E* **70**, 010901 (2004).
36. Lacasta, A. M., Sancho, J. M., Romero, A. H. & Lindenberg, K. Sorting on periodic surfaces. *Phys. Rev. Lett.* **94**, 160601 (2005).
37. Loehr, J. et al. Lattice symmetries and the topologically protected transport of colloidal particles. *Soft Matter* **13**, 5044–5075 (2017).
38. Mirzaee-Kakhki, M. et al. Simultaneous polydirectional transport of colloidal bipeds. *Nat. Commun.* **11**, 4670 (2020).
39. Loehr, J., Loenne, M., Ernst, A., de las Heras, D. & Fischer, T. M. Topological protection of multiparticle dissipative transport. *Nat. Commun.* **7**, 11745 (2016).
40. Phillips, C. L. et al. Digital colloids: reconfigurable clusters as high information density elements. *Soft Matter* **10**, 7468–7479 (2014).
41. Chakraborty, I. et al. Self-assembly dynamics of reconfigurable colloidal molecules. *ACS Nano* **16**, 2471–2480 (2022).
42. Solomon, M. J. Tools and functions of reconfigurable colloidal assembly. *Langmuir* **34**, 11205–11219 (2018).
43. Hendley, R. S., Zhang, L. & Bevan, M. A. Multistate dynamic pathways for anisotropic colloidal assembly and reconfiguration. *ACS Nano* **17**, 20512–20524 (2023).
44. de las Heras, D., Loehr, J., Loenne, M. & Fischer, T. M. Topologically protected colloidal transport above a square magnetic lattice. *New J. Phys.* **18**, 105009 (2016).
45. Chen, B. G., Upadhyaya, N. & Vitelli, V. Nonlinear conduction via solitons in a topological mechanical insulator. *Proc. Natl. Acad. Sci. USA* **111**, 13004–13009 (2014).
46. Porto, M., Urbakh, M. & Klafter, J. Atomic scale engines: cars and wheels. *Phys. Rev. Lett.* **84**, 6058–6061 (2000).
47. Popov, V. L. Nanomachines: methods to induce a directed motion at nanoscale. *Phys. Rev. E* **68**, 026608 (2003).
48. Nash, L. M. et al. Topological mechanics of gyroscopic metamaterials. *Proc. Natl. Acad. Sci. USA* **112**, 14495–14500 (2015).
49. Yang, Z. et al. Topological acoustics. *Phys. Rev. Lett.* **114**, 114301 (2015).
50. Mittal, S. et al. Topologically robust transport of photons in a synthetic gauge field. *Phys. Rev. Lett.* **113**, 087403 (2014).
51. Ningyuan, J., Owens, C., Sommer, A., Schuster, D. & Simon, J. Time- and site-resolved dynamics in a topological circuit. *Phys. Rev. X* **5**, 021031 (2015).
52. Hasan, M. Z. & Kane, C. L. Colloquium: topological insulators. *Rev. Mod. Phys.* **82**, 3045–3067 (2010).
53. Sobolev, Y. I. et al. Solid-body trajectories shaped to roll along desired pathways. *Nature* **620**, 310–315 (2023).
54. Elschner, J. et al. Topologically controlled synthesis of active colloidal bipeds (2023) (in preparation).
55. Michele, C. D., Gabrielli, S., Tartaglia, P. & Sciortino, F. Dynamics in the presence of attractive patchy interactions. *J. Phys. Chem. B* **110**, 8064–8079 (2006).
56. Bianchi, E., Blaak, R. & Likos, C. N. Patchy colloids: state of the art and perspectives. *Phys. Chem. Chem. Phys.* **13**, 6397–6410 (2011).
57. Yi, G.-R., Pine, D. J. & Sacanna, S. Recent progress on patchy colloids and their self-assembly. *J. Phys.: Condens. Matter* **25**, 193101 (2013).
58. Kim, Y.-J., Moon, J.-B., Hwang, H., Kim, Y. S. & Yi, G.-R. Advances in colloidal building blocks: toward patchy colloidal clusters. *Adv. Mater.* **35**, 2203045 (2022).
59. Geerts, N. & Eiser, E. DNA-functionalized colloids: physical properties and applications. *Soft Matter* **6**, 4647–4660 (2010).
60. Michele, L. D. et al. Multistep kinetic self-assembly of DNA-coated colloids. *Nat. Commun.* **4**, 2007 (2013).
61. Shelke, Y. et al. Flexible colloidal molecules with directional bonds and controlled flexibility. *ACS Nano* **17**, 12234–12246 (2023).
62. Hernandez, C. J. & Mason, T. G. Colloidal alphabet soup: monodisperse dispersions of shape-designed LithoParticles. *J. Phys. Chem. C* **111**, 4477–4480 (2007).
63. Sacanna, S., Pine, D. J. & Yi, G.-R. Engineering shape: the novel geometries of colloidal self-assembly. *Soft Matter* **9**, 8096–8106 (2013).
64. de las Heras, D., Zimmermann, T., Sammler, F., Hermann, S. & Schmidt, M. Perspective: how to overcome dynamical density functional theory. *J. Phys.: Condens. Matter* **35**, 271501 (2023).

65. Leyva, S. G., Stoop, R. L., Pagonabarraga, I. & Tierno, P. Hydrodynamic synchronization and clustering in ratcheting colloidal matter. *Sci. Adv.* **8**, eabo4546 (2022).
66. Sammüller, F. & Schmidt, M. Adaptive Brownian dynamics. *J. Chem. Phys.* **155**, 134107 (2021).
67. Stuhlmüller, N. C. X. Drawing with colloids. *Zenodo* <https://doi.org/10.5281/zenodo.8413928> (2023).
68. Kuświk, P. et al. Colloidal domain lithography in multilayers with perpendicular anisotropy: an experimental study and micromagnetic simulations. *Nanotechnology* **23**, 475303 (2012).
69. Lengemann, D., Engel, D. & Ehresmann, A. Plasma ion source for in situ ion bombardment in a soft x-ray magnetic scattering diffractometer. *Rev. Sci. Instrum.* **83**, 053303 (2012).
70. Chappert, C. et al. Planar patterned magnetic media obtained by ion irradiation. *Science* **280**, 1919–1922 (1998).
71. Urbaniak, M. et al. Domain-wall movement control in Co/Au multilayers by he⁺-ion-bombardment-induced lateral coercivity gradients. *Phys. Rev. Lett.* **105**, 067202 (2010).
72. Kuświk, P. et al. Colloidal domain lithography for regularly arranged artificial magnetic out-of-plane monodomains in Au/Co/Au layers. *Nanotechnology* **22**, 095302 (2011).
73. Jarosz, A., Holzinger, D., Urbaniak, M., Ehresmann, A. & Stobiecki, F. Manipulation of superparamagnetic beads on patterned Au/Co/Au multilayers with perpendicular magnetic anisotropy. *J. Appl. Phys.* **120**, 084506 (2016).
74. Bowick, M. J. & Giomi, L. Two-dimensional matter: order, curvature and defects. *Adv. Phys.* **58**, 449–563 (2009).
75. Krita (Krita foundation, accessed June 2023) <https://krita.org/>.
76. Olson, E. On computing the average orientation of vectors and lines. In *2011 IEEE International Conference on Robotics and Automation*, 3869–3874 (IEEE, Shanghai, China, 2011). <https://doi.org/10.1109/ICRA.2011.5979562>.

Acknowledgements

We thank Adrian Ernst for helping us to transfer the loops from the simulations to the experiment. We acknowledge funding by the Deutsche Forschungsgemeinschaft (DFG, German Research Foundation) under project numbers 440764520 (T.M.F. and D.d.l.H.) and 531559581 (D.d.l.H. and T.M.F.).

Author contributions

N.C.X.S. designed the modulation loops and performed the computer simulations. F.F. performed the experiments. N.C.X.S., F.F., T.M.F., and D.d.l.H. conceptualized the research. P.K., F.S., and M.U. produced the magnetic film. S.A. and Ar.E. performed the fabrication of the

micromagnetic domain patterns within the magnetic thin film. N.C.X.S., T.M.F., and D.d.l.H. designed the patterns and wrote the manuscript. All authors contributed to the different revision stages of the manuscript.

Funding

Open Access funding enabled and organized by Projekt DEAL.

Competing interests

The authors declare no competing interests.

Additional information

Supplementary information The online version contains supplementary material available at <https://doi.org/10.1038/s41467-023-43390-0>.

Correspondence and requests for materials should be addressed to Daniel de las Heras.

Peer review information *Nature Communications* thanks Pietro Tierno and the other anonymous reviewer(s) for their contribution to the peer review of this work. A peer review file is available.

Reprints and permissions information is available at <http://www.nature.com/reprints>

Publisher's note Springer Nature remains neutral with regard to jurisdictional claims in published maps and institutional affiliations.

Open Access This article is licensed under a Creative Commons Attribution 4.0 International License, which permits use, sharing, adaptation, distribution and reproduction in any medium or format, as long as you give appropriate credit to the original author(s) and the source, provide a link to the Creative Commons license, and indicate if changes were made. The images or other third party material in this article are included in the article's Creative Commons license, unless indicated otherwise in a credit line to the material. If material is not included in the article's Creative Commons license and your intended use is not permitted by statutory regulation or exceeds the permitted use, you will need to obtain permission directly from the copyright holder. To view a copy of this license, visit <http://creativecommons.org/licenses/by/4.0/>.

© The Author(s) 2023

Supplementary Information

Simultaneous and independent topological control of identical microparticles in non-periodic energy landscapes

Nico C. X. Stuhlmüller,¹ Farzaneh Farrokhzad,² Piotr Kuświk,³ Feliks Stobiecki,³ Maciej Urbaniak,³ Sapida Akhundzada,⁴ Arno Ehresmann,⁴ Thomas M. Fischer,² and Daniel de las Heras^{1,*}

¹*Theoretische Physik II, Physikalisches Institut, Universität Bayreuth, D-95440 Bayreuth, Germany*

²*Experimentalphysik X, Physikalisches Institut, Universität Bayreuth, D-95440 Bayreuth, Germany*

³*Institute of Molecular Physics, Polish Academy of Sciences, 60-179 Poznań, Poland*

⁴*Institute of Physics and Center for Interdisciplinary Nanostructure Science and Technology (CINSaT), University of Kassel, D-34132 Kassel, Germany*

(Dated: November 7, 2023)

SUPPLEMENTARY NOTE 1 SIMPLE PATTERNS AND SIMPLE LOOPS

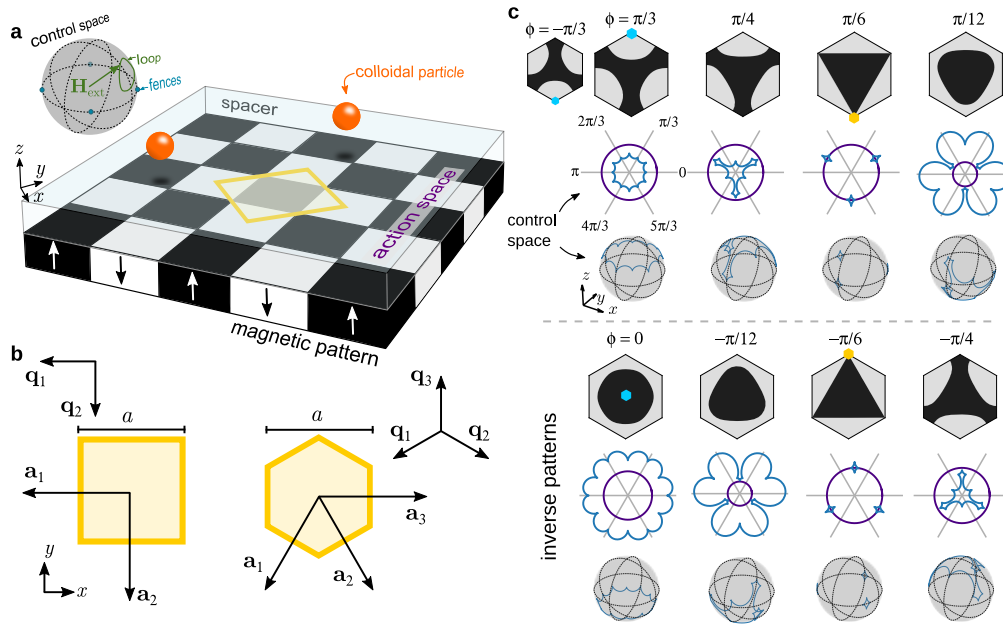
We summarize here the topological transport control of isotropic magnetic colloidal particles above periodic magnetic patterns. A sketch of the system and the different types of periodic patterns is shown in Supplemental Fig. 1. Detailed theoretical and experimental studies can be found in Refs. [1–3]. For a given orientation of the external magnetic field, there is in general at least one minimum of the magnetic potential per Wigner-Seitz cell. During a modulation loop, the changes in the orientation of \mathbf{H}_{ext} are slow enough such that the colloidal particles can follow a minimum of the magnetic potential at every time. In this sense the colloidal motion is adiabatic except if the minimum that transports a particles disappears (e.g. due to the annihilation with a saddle point). In such cases, the colloidal particle performs a ratchet motion towards a minimum nearby.

To control the colloidal transport we therefore need to understand the stationary points of the magnetic potential. The position of the minima in action space depends on the orientation of \mathbf{H}_{ext} and on the symmetry of the pattern. By analysing the eigenvectors and the eigenvalues of the Hessian matrix of the magnetic potential, it turns out [1–3] that action space can be split into allowed and forbidden regions for the colloidal particles, see Supplemental Fig. 2. For each space point in an allowed region it is always possible to find an orientation of \mathbf{H}_{ext} such that the magnetic potential is a minimum. Note also that a minimum of V_{mag} can be transformed into a maximum by simply inverting the external field since $V_{\text{mag}} \propto \mathbf{H}_{\text{p}} \cdot \mathbf{H}_{\text{ext}}$. Hence both minima and maxima of V_{mag} can be found in the allowed regions. For each space point in a forbidden region, there is an orientation of \mathbf{H}_{ext} such that the magnetic potential is a saddle point, but never a minimum.

The boundary between the allowed and the forbidden regions are the fences. The location of the fences in both action space and control space depend on the symmetry of the pattern. In a square pattern, the fences in \mathcal{C} are four equidistant points on the equator, see Supplemental Fig. 1(a). In hexagonal patterns however the fences are curves, the shape and the position of which vary with the symmetry phase ϕ , Supplemental Fig. 1(c). Crucially, in hexagonal patterns the fences of a given pattern and its corresponding inverse pattern (opposite magnetization) do not coincide in control space, cf. the top and the bottom patterns in Supplemental Fig. 1(c). As we discuss now, this means that the transport in a given pattern and its inverse pattern can be independently controlled with a single modulation loop.

The position of the fences is relevant to control the colloidal motion, which in action space occurs through the allowed regions. Two adjacent allowed regions are connected via points that we refer to as the gates, see Supplemental Fig. 2. To adiabatically transport a particle from one allowed region to an adjacent allowed region, we need to modulate \mathbf{H}_{ext} in \mathcal{C} such that a minimum of the potential crosses the gate that connects both regions. To induce transport between two consecutive Wigner-Seitz cells using closed modulation loops in \mathcal{C} , the loop in \mathcal{C} needs to be such that the particle crosses two different gates once the loop returns to its initial position. In square patterns such loops are those that wind around the fence points [2, 3] in \mathcal{C} , see an example in Supplemental Fig. 2(a). In hexagonal patterns, the fences in \mathcal{C} are curves made of twelve segments. Two fence segments in \mathcal{C} meet at a bifurcation point. The loops that induce transport in hexagonal patterns are those that wind around at least three consecutive bifurcation points of the fences [1, 3] (enclosing therefore at least two consecutive fence segments). The bifurcation points are indicated

* delasheras.daniel@gmail.com; www.danieldelasheras.com



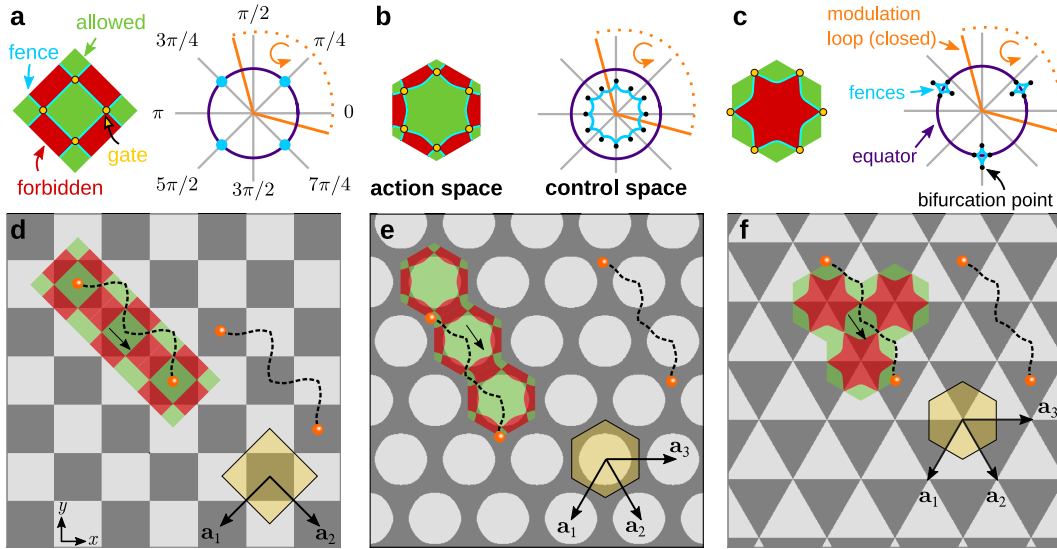
Supplementary Fig. 1. **Setup and magnetic patterns.** (a) Sketch of the system: a square magnetic pattern with domains of positive (black) and negative (white) magnetization parallel to the normal of the pattern. A Wigner-Seitz cell is highlighted in yellow. Identical colloidal particles are located above the pattern. A spacer restricts the particle motion to action space \mathcal{A} , a plane parallel to the pattern. An external magnetic field \mathbf{H}_{ext} spatially uniform (green arrow) drives the motion via closed loops (green loop) of its orientation in control space \mathcal{C} (sphere). The fences in \mathcal{C} are represented in blue. (b) Wigner-Seitz cells in square and hexagonal patterns. The lattice vectors \mathbf{a}_i and the wave vectors \mathbf{q}_i are also shown. The magnitude of the lattice vectors is a . In the experiments $a = 14 \mu\text{m}$. (c) Magnetization of Wigner-Seitz cells and corresponding control spaces in a family of hexagonal patterns with varying symmetry phase ϕ , as indicated. The fences are represented in blue. The control space is represented via a sphere and also using a stereographic projection in which the equator is represented as a violet circle. The patterns in the bottom row have the inverse magnetization than those in the upper row and the unit cell is also shifted. The yellow and the blue hexagons indicate the position of points with S_6 and C_6 symmetry, respectively.

in Supplemental Fig. 2(b) and Supplemental Fig. 2(c) for patterns with C_6 and S_6 symmetries, respectively, together with illustrative examples of loops that induce transport.

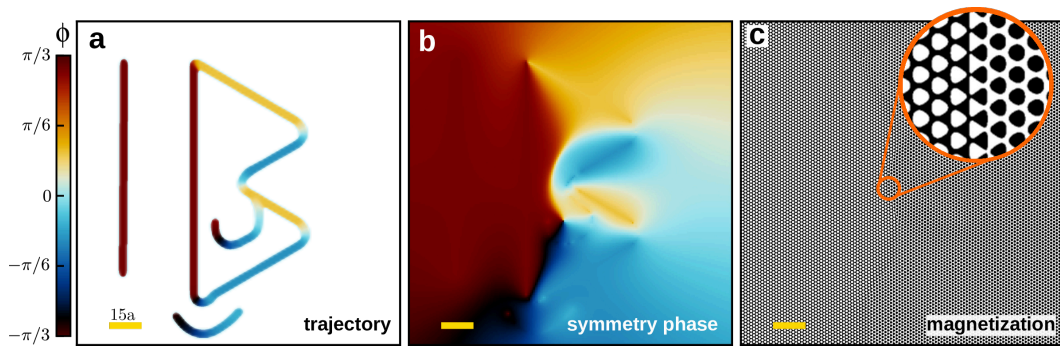
The simplest but non-trivial modulation loops that induce net motion are those that transport the particles along the symmetry directions of the pattern. These are given by lattice vectors $\pm \mathbf{a}_i$ with $i = 1, \dots, N$ and $N = 2$ ($N = 3$) in square (hexagonal) patterns, see Supplemental Fig. 1. Illustrative examples of such modulation loops are shown in Supplemental Fig. 2.

The transport in square patterns is always adiabatic, and reversing the modulation loop reverses also the direction of transport [2]. In contrast, in hexagonal patterns the transport can be either adiabatic or ratchet-like [1, 3]. In the latter case, reversing the loop does not always reverse the direction of the transport. However, the direction of the transport is in all cases deterministic and topologically protected.

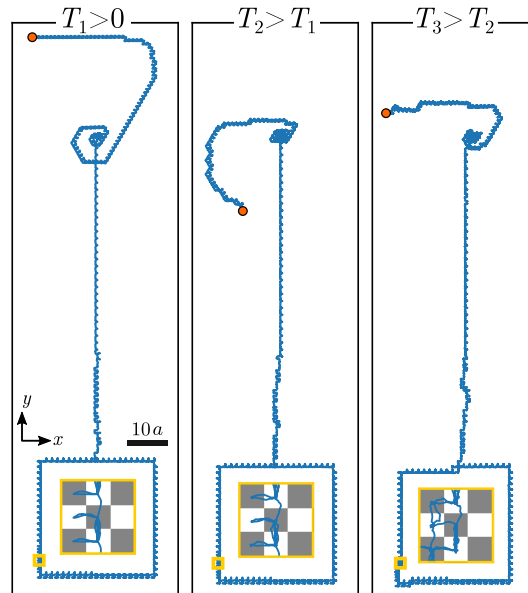
The set of winding numbers of the modulation loop around the fences (square patterns) and around the bifurcation points (hexagonal patterns) is the topological invariant that protects the motion. Any two loops with the same set of winding numbers (topological invariant) will transport a particle in the same direction, even though the detailed trajectories depend of course on the particular shapes of the loops.



Supplementary Fig. 2. **Simple patterns and simple loops.** Action space and control space in square patterns (a) and hexagonal patterns with C_6 (b) and S_6 (c) symmetries. A unit cell illustrating the allowed (green) and forbidden (red) regions of action space, as well as the fences (blue lines) and the gates (yellow circles) is represented in each case. The control spaces (stereographic projections) show the equator (violet circle), the fences (blue), and a modulation loop (orange). The twelve bifurcation points in \mathcal{C} of the fences of C_6 and S_6 patterns are also indicated with black circles. The modulation loop is the same in all cases and it is made of two segments of constant azimuthal angle joined at the north and the south poles of control space. The connection at the south pole (not visible due to the stereographic projection) is illustrated with a dotted orange segment. The loops wind anticlockwise, as indicated by the circular orange arrows. Magnetization in patterns with square (d), C_6 (e), and S_6 (f) symmetries. Black (white) regions are up (down) magnetized. The global phase is set to $\psi = \pi/4$ (d), $\psi = \pi/3$ (e), and $\psi = \pi/6$ (f). Black dashed lines are Brownian dynamics simulations of the trajectories of colloidal particles (orange circles) subjected to two consecutive modulation loops. The transport direction is indicated with black arrows. The trajectories go along the allowed regions only. A unit cell of each pattern with corresponding lattice vectors \mathbf{a}_i is highlighted in yellow. For visualization purposes we have shifted the unit cells of the C_6 and the S_6 patterns with respect to those represented in Supplemental Fig. 1.



Supplementary Fig. 3. **Generation of symmetry phase modulated patterns.** (a) Trajectory drawn in Krita and colored according to the desired symmetry phase (color bar). The actual line is 1 pixel thick. Here we have made the trajectory thicker for visualization purposes. (b) Symmetry phase in the whole pattern calculated using the value of the symmetry phase along the trajectory. (c) Final magnetization of the pattern. The magnetization is positive in the black regions and negative in the white regions. The inset is a close view of a small region of the pattern, as indicated. Approximately the same region of the experimental pattern is highlighted in Fig. 4(c) of the main text. The length of the scale bars (yellow) is $15a$.



Supplementary Fig. 4. **Finite temperature effects.** Brownian dynamics simulations of colloidal particles moving above an inhomogeneous pattern at three different finite temperatures: $k_B T_1 / \epsilon \approx 3 \cdot 10^{-3}$, $k_B T_2 / \epsilon \approx 1 \cdot 10^{-2}$, and $k_B T_3 / \epsilon \approx 2 \cdot 10^{-2}$. The energy scale ϵ is the absolute value of the average external energy that a particle has when the external field points normal to the pattern. The particle trajectories are represented in blue (the starting point is indicated with an orange circle). The scale bar is $10a$. The pattern is made of two subpatterns: a top subpattern with a topological defect in the symmetry phase and a bottom subpattern with square symmetry. The insets are closed views of a small region (indicated by a yellow square) showing the trajectory (blue) and the magnetization of the pattern.

SUPPLEMENTARY REFERENCES

- [1] J. Loehr, M. Loenne, A. Ernst, D. de las Heras, and T. M. Fischer, Topological protection of multiparticle dissipative transport, *Nat. Commun.* **7**, 11745 (2016).
- [2] D. de las Heras, J. Loehr, M. Loenne, and T. M. Fischer, Topologically protected colloidal transport above a square magnetic lattice, *New. J. Phys.* **18**, 105009 (2016).
- [3] J. Loehr, D. de las Heras, M. Loenne, J. Bugase, A. Jarosz, M. Urbaniak, F. Stobiecki, A. Tomita, R. Huhnstock, I. Koch, A. Ehresmann, D. Holzinger, and T. M. Fischer, Lattice symmetries and the topologically protected transport of colloidal particles, *Soft Matter* **13**, 5044 (2017).

2.7 Summary and outlook

In this thesis we have investigated the transport of colloidal particles through inhomogeneous energy landscapes. We have explored the transport of paramagnetic particles above [4] and between magnetic patterns [1, 3] and have also looked into the transport properties of colloidal particles in arrays of optical tweezers. In publications 1 and 2 we have investigated how colloidal particles move when positioned between two identical but rotated and shifted patterns and pushed by a small drift force. We have shown that there exist magic angles at which the mobility of the particles massively increases. This can be seen as a classical implementation of twisted bilayer graphene and its superconducting state at the magic angle. In future works one might investigate the effects of dynamically changing the twist angle on the transport properties of the colloidal particles. This might allow us to build a dynamical sorting machine for particles with different friction coefficients against the solvent.

In publication 3 we have added topological transport to colloidal particles sandwiched between twisted patterns and have explored the commensuration effects of both transport modes, topological- and drift-transport. We have seen new effects that resemble the quantum hall effect, i.e. that the average velocity when measured in multiples of half the length of the lattice vector of the supercells per loop, increases in integer steps for drift forces larger than the critical force. The two transport types can also completely cancel any macroscopic transport when they oppose each other. In a future project one might investigate more complex loops that transport dia- and paramagnets in different directions, while the drift force points in the same direction for both. Then the interaction of the particles with each other and the competition of the external forces might lead to novel phenomena.

We have also investigated the transport of particles above single inhomogeneous patterns driven by loops of an external magnetic field. When doing so, we combined multiple simple periodic patterns to more interesting superpatterns. In publication 4 we have exploited, that one can continuously morph a hexagonal pattern through a whole class of patterns by changing its symmetry phase. When doing this we can control the motion of particles in different regions of the patterns independently. The path along which the symmetry of the pattern changes can be chosen as any closed curve. There exist then loops of the external magnetic field, that make particles follow this prescribed curve. Patterns with such closed curves have at least one

topological defect inside the closed curve where the symmetry phase is not well defined. As a future project one might investigate the effects of multiple of these defects on the transport of particles. Another possibility for the combination of simple patterns with each other is to combine patterns of different symmetry classes.

To conclude, we have developed novel ways to control the motion of colloidal particles. In future studies it would be interesting to investigate how the transport properties of the discussed systems change when multiple particles that interact with each other are considered. We expect a transition from topological transport to geometric transport in the system of publication 4, as was already seen by Rossi et al. [52]. In the twisted systems, particle interactions might allow for easier transport, even in channels that do not allow for macroscopic transport for single particles. Behavior similar to that has been observed by Antonov et. al. [89]. Interactions like these and others might be a possibility to experimentally measure superadiabatic forces [90–92].

3 Topologically cloaked transport

In this section we show how conformal deformations of the magnetization of square patterns can be used to construct a cloaked region in the pattern. The system investigated shares similarities with the inhomogeneous patterns of publication 4. Here, we also use inhomogeneous magnetic patterns magnetized normal to the plane of the pattern. Paramagnetic colloidal particles are suspended above the pattern and driven solely by loops in the orientation of an external magnetic field. The inhomogeneity of the pattern is achieved by deforming the magnetization with conformal mappings. We show the process of constructing the patterns below. As the transport of the colloidal particles is robust under small deformations in the magnetic pattern, we can locally rotate a square pattern from -45° up to 45° and still move the particles along the co-rotated unit-vectors. If we rotated unit-cells more than $\pm 45^\circ$, the fence points corresponding to different unit-cells would pass by each other, and particles would move along undesired directions. Restricting the local rotation of the unit-cells to $\pm 45^\circ$ allows us to guide the particles around the cloaked region by letting particles move left and right around the cloaked region. After the particles have passed around the cloaked regions, their trajectories are indistinguishable from trajectories above a simple square pattern without a cloaked region. Next we show how to generate the cloaked patterns, and afterwards present illustrative particle trajectories.

3.1 Generating cloaked patterns

We map complex numbers $U \subset \mathbb{C}$ to locations above the pattern using a conformal map $\mathbf{r}(z) = (\Re r(z), \Im r(z))$ and to a magnetization at position \mathbf{r} via a proxy function $\mathbf{M}(z; u(z))$. We use $u(z) = z + R^2/z$, with R being a

measure for the size¹ of the cloak and

$$\mathbf{M}(z; u(z)) \propto \text{sign} [\cos(2\pi\Re u(z)) + \cos(2\pi\Im u(z))] \mathbf{n}, \quad (3.1)$$

where \mathbf{n} is the vector normal to the pattern.

We restrict the conformal map $r(z)$ to three cases, that together with $u(z)$, form a circular, a square or a boat shaped cloak.

$$r_{\circ}(z) = z, \quad (3.2)$$

$$r_{\diamond}(z) = z \left(1 + \left(\frac{2R}{\pi z} \right)^4 \right)^{3/4}, \quad (3.3)$$

$$r_{\circlearrowleft}(z) = z \sqrt{1 - R^2/(2z^2)} + \frac{R^2}{2z \sqrt{1 - R^2/(2z^2)}}. \quad (3.4)$$

The resulting magnetizations together with the cloaked regions for r_{\circ} , r_{\diamond} and r_{\circlearrowleft} are shown in figure 3.1 (a-c) respectively. The square and boat shaped

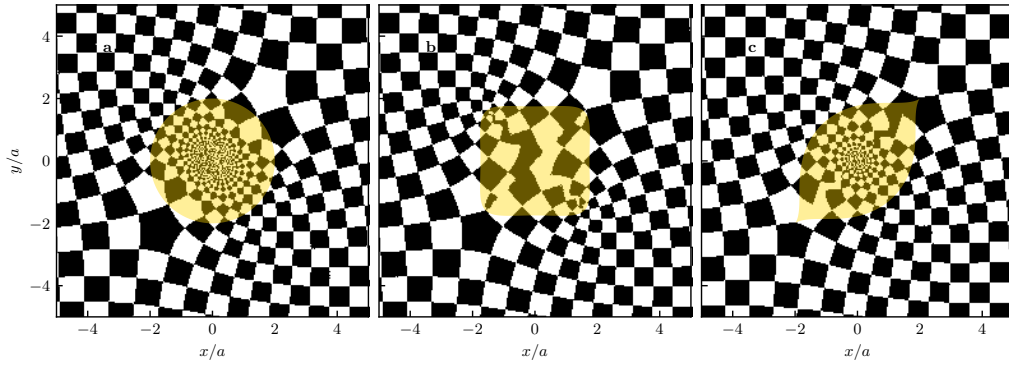


Figure 3.1: Magnetization of cloaked patterns. (a) circular cloak, (b) square cloak, (c) boat shaped cloak. Cloaked regions are highlighted in yellow. Black (white) regions indicate a positive (negative) magnetization normal to pattern. R is set to $2e^{i\pi/4}$.

cloaks map the complex plane onto itself multiple times. This results in different z , with in principle different magnetizations, being located at the same position \mathbf{r} . To circumvent this we need to restrict U such that $r(z)$ maps to the complex plane exactly once. Note that for $|z| \gg |R|$, $r(z) \approx z$

¹ $|R|$ is the radius of the cloak if $r(z)$ is the identity, however, we also choose non trivial functions for $r(z)$, in which case $|R|$ is only an approximate measure for the size of the cloak

for all cloaks investigated. Therefore, we only need to take precautions when $|z|$ is comparable to, or smaller than $|R|$. To separate the two preimages (sometimes also called inverse images) of the complex plane under $r(z)$, we find the points z_b for which $\Im r(z_b) = 0$. These points form a boundary that separates the preimages. Then all points outside of the boundary map to the complex plane exactly once, which means if we set U to the set of these points, we can calculate a unique magnetization.

However, given a point \mathbf{r} in action space we can not calculate the magnetization there directly. We can only translate a complex number z to a position in action space, but not the other way round. If we wanted to start from a given position in action space, we would need to invert the conformal maps $r(z)$. Although this is in principle possible since the maps are conformal, it is in practice quite hard, because $r_\diamond(z)$ and $r_\emptyset(z)$ are not easily invertible analytically. Not being able to get the magnetization at a desired position is a problem, because we want to know \mathbf{M} on a rectangular grid such that it is numerically convenient to compute the magnetic field \mathbf{H}_p from \mathbf{M} (as explained in section 4.2), which we need to calculate the forces acting on the particles. To compute \mathbf{M} on a rectangular grid, we calculate \mathbf{M} and the corresponding positions \mathbf{r} from a fine polar mesh of U . In order to then find the magnetization at the desired position \mathbf{r}_d on the rectangular grid we find the four closest points in $\mathbf{r}(U)$ that form a convex quadrilateral around \mathbf{r}_d . We use these four points to interpolate bilinearly the value of \mathbf{M} at \mathbf{r}_d . This method restricts the interpolated magnetization at position \mathbf{r}_d to be bounded by the magnetization at the four surrounding points. If we had just used the four closest points, they might form a concave quadrilateral next to \mathbf{r}_d . A bilinear interpolation of the magnetization to \mathbf{r}_d would then not be bounded by the magnetization of the four quadrilateral points and would additionally not always result in the right magnetization at \mathbf{r}_d . In order to find the closest points to \mathbf{r}_d in a reasonable time we use k-d trees [93].

3.2 Simulation results

In figure 3.2 (a-c) we show that paramagnetic colloidal particles can be moved around the cloaked regions by loops of the orientation of the external magnetic field. In simulation we find that there exists a maximal height z_m for which the particles follow the path around the cloaked region. This maximal height depends on the magnitude of R and the shape of the cloak.

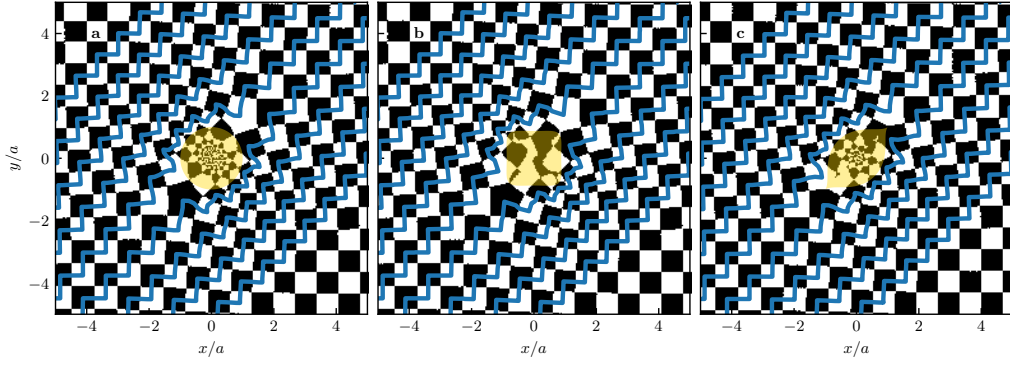


Figure 3.2: Trajectories (blue) above cloaked patterns (black and white background). Black (white) regions have a positive (negative) magnetization normal to pattern. R is set to $e^{i\pi/4}$. The particles move in a height $z = 0.3 a$ for the circular (a), $z = 0.06 a$ for the square (b) and $z = 0.26 a$ for the boat-shaped (c) cloak respectively.

Table 3.1: Maximal height z_m for the three differently shaped cloak (vertical axis) as a function of $|R|$ (horizontal axis). The maximal height and $|R|$ are give in multiples of a . Empty entries mean that we did not find a value of z_m for which the region in the center is cloaked.

	0.5	1.0	2.0	3.0	3.5	4.0
circular	0.80	0.37				
square	0.30	0.06				
boat	0.34	0.29	0.33	0.37	0.30	0.26

We present a table of z_m for the different shapes of the cloak and different absolute values of R in table 3.1. We find that only the boat shaped cloak allows for cloaked areas much larger than a unit-cell. Therefore experiments should focus on the boat shaped cloak.

4 Methods

4.1 Integrating the equation of motion

In this thesis we have performed computer simulations of physical systems. These simulations have been carried out by numerically integrating the equation of motion, i.e. equation (1.2). One has to choose an integration method in order to do so. Often the Euler-Maruyama method is chosen for its simplicity, even though it requires a very small time-step, the size of which is in principle not known to the simulator a priori [87]. With an adaptive integration method this guessing of an appropriate time step can be circumvented [94]. In order for the time-step to be adjusted one needs two integration methods of different order, such that the error of the integration methods can be estimated. When the error exceeds a predefined tolerance, the trial move of the integrator has to be rejected and the time-step needs to be adjusted. This however is not trivial, because if one naively rejects the time-step together with the Brownian noise, one alters the distribution of the noise [87]. Therefore, one has to retain the information of the noise. One can however not simply keep the random numbers drawn for the noise, as the standard deviation of the random numbers is linked to the time-step, which we want to adjust. Sammüller and Schmidt [87] used the Brownian bridge theorem to overcome this problem in the integration scheme known as “adaptive Brownian Dynamics”. The algorithm features adaptive time stepping and is of second order. Due to the advantages of this algorithm we used it in all our works after its publication, i.e. from publication 2 onward. It allowed us to speed up the simulations and to have a proper estimate for the error of the simulations.

4.2 Calculating the magnetic field from the pattern magnetization

The magnetic field at a height z above the pattern can be calculated from the magnetization $\mathbf{M}(\mathbf{r})$ of the pattern via a convolution with the Green's function of the 3D Poisson equation. In our systems, we can approximate the magnetization of the pattern to be concentrated on its surface and to be normal to it. That is $\mathbf{M}(\mathbf{r}) = M_s(\mathbf{r}_A)\delta(z)\mathbf{e}_z$, where $\mathbf{r} = \mathbf{r}_A + z\mathbf{e}_z$, with the first two components of \mathbf{r} and \mathbf{r}_A lying in \mathcal{A} , and the third component of \mathbf{r} given by $z\mathbf{e}_z$, where \mathbf{e}_z is the unit vector normal to the pattern. This simplifies the expression for the magnetic field at position \mathbf{r} to

$$\mathbf{H}_p(\mathbf{r}) = \mathbf{H}_p(\mathbf{r}_A, z) = \frac{1}{4\pi} \int_{\mathcal{A}} \frac{\mathbf{r}_A - \mathbf{r}'_A + z\mathbf{e}_z}{|\mathbf{r}_A - \mathbf{r}'_A + z\mathbf{e}_z|^3} M_s(\mathbf{r}_A) d^2\mathbf{r}'_A, \quad (4.1)$$

where the integral runs over the complete action space. In the case of simple patterns and linear combinations of them we can analytically calculate the magnetic field \mathbf{H}_p from the magnetization in the limit of the elevation z being far greater than the absolute value of a lattice vector [54–56]. When the magnetization is however more intricate than a simple periodic structure, an analytic calculation becomes exceedingly hard. We then resort to numerical methods. We perform the convolution in equation (4.1) in Fourier-space to speed up the calculation. In figure 4.1 the magnetization, panel (a), and the resulting magnetic field, panels (b-d), for a simple square pattern are shown. Since the Fourier transform is only bijective when all modes are kept we do not discard any modes.

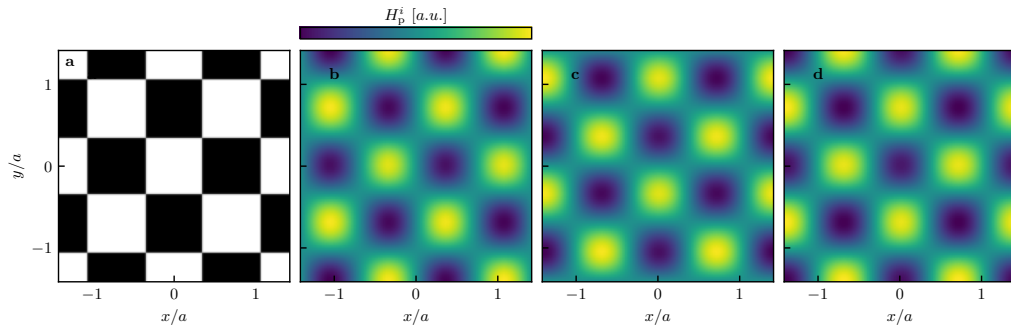


Figure 4.1: Illustrative magnetization (a) and components of the resulting magnetic field (b-d). Black (white) regions in (a) have a positive (negative) magnetization normal to the pattern. (b-d) show the x , y , z -component of \mathbf{H}_p respectively.

Bibliography

1. N. C. X. Stuhlmüller, T. M. Fischer, and D. de las Heras. Enhanced colloidal transport in twisted magnetic patterns. *Commun. Phys.* **5**, 48 (2022).
2. N. C. X. Stuhlmüller, T. M. Fischer, and D. de las Heras. Colloidal transport in twisted lattices of optical tweezers. *Phys. Rev. E* **106**, 034601 (2022).
3. N. C. X. Stuhlmüller, T. M. Fischer, and D. de las Heras. Competition between drift and topological transport of colloidal particles in twisted magnetic patterns. under review in *New J. Phys.* (2023).
4. N. C. X. Stuhlmüller, F. Farrokhzad, P. Kuświk, F. Stobiecki, M. Urbaniak, S. Akhundzada, A. Ehresmann, T. M. Fischer, and D. de las Heras. Simultaneous and independent topological control of identical microparticles in non-periodic energy landscapes. *Nat. Commun.* **14**, 7517 (2023).
5. A. M. E. B. Rossi, N. C. X. Stuhlmüller, P. Kuświk, F. Stobiecki, M. Urbaniak, S. Akhundzada, A. Ehresmann, D. de las Heras, and T. M. Fischer. Topological cloaked magnetic colloidal transport. in preparation (2023).
6. J. R. Rumble. *CRC Handbook of Chemistry and Physics* (Taylor & Francis Group, 2022).
7. A. S. Lyon, W. B. Peeples, and M. K. Rosen. A framework for understanding the functions of biomolecular condensates across scales. *Nat. Rev. Mol. Cell Bio.* **22**, 215 (2020).
8. F. Castiglione, F. Pappalardo, C. Bianca, G. Russo, and S. Motta. Modeling Biology Spanning Different Scales: An Open Challenge. *BioMed Res. Int.* **2014**, 1 (2014).
9. A. Stradner and P. Schurtenberger. Potential and limits of a colloid approach to protein solutions. *Soft Matter* **16**, 307 (2020).

10. A. J. Maheshwari, A. M. Sunol, E. Gonzalez, D. Endy, and R. N. Zia. Colloidal hydrodynamics of biological cells: A frontier spanning two fields. *Phys. Rev. Fluids* **4**, 110506 (2019).
11. R. G. Jones, E. S. Wilks, W. V. Metanowski, J. Kahovec, M. Hess, R. Stepto, and T. Kitayama. *Compendium of Polymer Terminology and Nomenclature: IUPAC Recommendations 2008* (The Royal Society of Chemistry, 2009).
12. F. Li, W. C. Yoo, M. B. Beernink, and A. Stein. Site-Specific Functionalization of Anisotropic Nanoparticles: From Colloidal Atoms to Colloidal Molecules. *J. Am. Chem. Soc.* **131**, 18548 (2009).
13. J. Zhuang, H. Wu, Y. Yang, and Y. C. Cao. Supercrystalline Colloidal Particles from Artificial Atoms. *J. Am. Chem. Soc.* **129**, 14166 (2007).
14. W. Poon. Colloids as Big Atoms. *Science* **304**, 830 (2004).
15. M. González-Pinto, F. Borondo, Y. Martínez-Ratón, and E. Velasco. Clustering in vibrated monolayers of granular rods. *Soft Matter* **13**, 2571 (2017).
16. L. Kong, J. Guan, and M. Pumera. Micro- and nanorobots based sensing and biosensing. *Curr. Opin. Electrochem.* **10**, 174 (2018).
17. O. Gröbner. Vacuum system for LHC. *Vacuum* **46**, 797 (1995).
18. E. J. Eichten, K. D. Lane, and M. E. Peskin. New Tests for Quark and Lepton Substructure. *Phys. Rev. Lett.* **50**, 811 (1983).
19. P. Magarshack and P. G. Paulin. *System-on-chip beyond the nanometer wall* in *Proceedings of the 40th annual Design Automation Conference* (ACM, 2003).
20. I. Ali, S. H. Althakfi, M. Suhail, M. Locatelli, M.-F. Hsieh, M. Alsehli, and A. M. Hameed. Advances in Polymeric Colloids for Cancer Treatment. *Polymers* **14**, 5445 (2022).
21. G. Yang, R. Yuan, and Y.-Q. Chai. A high-sensitive amperometric hydrogen peroxide biosensor based on the immobilization of hemoglobin on gold colloid/l-cysteine/gold colloid/nanoparticles Pt–chitosan composite film-modified platinum disk electrode. *Colloids Surf., B* **61**, 93 (2008).
22. G. Candiano, M. Bruschi, L. Musante, L. Santucci, G. M. Ghiggeri, B. Carnemolla, P. Orecchia, L. Zardi, and P. G. Righetti. Blue silver: A very sensitive colloidal Coomassie G-250 staining for proteome analysis. *Electrophoresis* **25**, 1327 (2004).

23. N. Zhang, B. Liu, X. Cui, Y. Li, J. Tang, H. Wang, D. Zhang, and Z. Li. Recent advances in aptasensors for mycotoxin detection: On the surface and in the colloid. *Talanta* **223**, 121729 (2021).
24. C. Farcau, H. Moreira, B. Viallet, J. Grisolia, D. Ciuculescu-Pradines, C. Amiens, and L. Ressler. Monolayered Wires of Gold Colloidal Nanoparticles for High-Sensitivity Strain Sensing. *J. Phys. Chem. C* **115**, 14494 (2011).
25. R. Sliz, M. Lejay, J. Z. Fan, M.-J. Choi, S. Kinge, S. Hoogland, T. Fabritius, F. P. G. de Arquer, and E. H. Sargent. Stable Colloidal Quantum Dot Inks Enable Inkjet-Printed High-Sensitivity Infrared Photodetectors. *ACS Nano* **13**, 11988 (2019).
26. P. E. Watson, I. D. Watson, and R. D. Batt. Total body water volumes for adult males and females estimated from simple anthropometric measurements. *Am. J. Clin. Nutr.* **33**, 27 (1980).
27. J.-P. Hansen and I. R. McDonald. *Theory of Simple Liquids* (Elsevier, 2013).
28. A. Einstein. Über die von der molekularkinetischen Theorie der Wärme geforderte Bewegung von in ruhenden Flüssigkeiten suspendierten Teilchen. *Ann. Phys. (Berl.)* **322**, 549 (1905).
29. A. Daddi-Moussa-Ider and S. Gekle. Brownian motion near an elastic cell membrane: A theoretical study. *Eur. Phys. J. E* **41** (2018).
30. A. Ashkin, J. M. Dziedzic, J. E. Bjorkholm, and S. Chu. Observation of a single-beam gradient force optical trap for dielectric particles. *Opt. Lett.* **11**, 288 (1986).
31. A. Ashkin and J. M. Dziedzic. Optical Trapping and Manipulation of Viruses and Bacteria. *Science* **235**, 1517 (1987).
32. A. Würger. Thermal non-equilibrium transport in colloids. *Rep. Prog. Phys.* **73**, 126601 (2010).
33. T. Eckert, M. Schmidt, and D. de las Heras. Sedimentation path theory for mass-polydisperse colloidal systems. *J. Chem. Phys.* **157**, 234901 (2022).
34. T. Eckert, M. Schmidt, and D. de las Heras. Gravity-induced phase phenomena in plate-rod colloidal mixtures. *Commun. Phys.* **4**, 202 (2021).
35. J. Renner, M. Schmidt, and D. de las Heras. Custom flow in molecular dynamics. *Phys. Rev. Res.* **3**, 013281 (2021).

36. D. de las Heras, J. Renner, and M. Schmidt. Custom flow in overdamped Brownian dynamics. *Phys. Rev. E* **99**, 023306 (2019).
37. J. Deng, H. Dong, C. Zhang, Y. Wu, J. Yuan, X. Zhu, F. Jin, H. Li, Z. Wang, H. Cai, C. Song, H. Wang, J. Q. You, and D.-W. Wang. Observing the quantum topology of light. *Science* **378**, 966 (2022).
38. R. F. W. Bader, S. G. Anderson, and A. J. Duke. Quantum topology of molecular charge distributions. 1. *J. Am. Chem. Soc.* **101**, 1389 (1979).
39. Q. Niu, D. J. Thouless, and Y.-S. Wu. Quantized Hall conductance as a topological invariant. *Phys. Rev. B* **31**, 3372 (1985).
40. E. Orlandini and C. Micheletti. Topological and physical links in soft matter systems. *J. Phys.: Condens. Matter* **34**, 013002 (2021).
41. V. Vitelli. Topological soft matter: Kagome lattices with a twist. *Proc. Natl. Acad. Sci.* **109**, 12266 (2012).
42. J. Smrek, J. Garamella, R. Robertson-Anderson, and D. Michieletto. Topological tuning of DNA mobility in entangled solutions of supercoiled plasmids. *Sci. Adv.* **7** (2021).
43. J.-P. Luminet. The Status of Cosmic Topology after Planck Data. *Universe* **2**, 1 (2016).
44. M. Lachièze-Rey and J.-P. Luminet. Cosmic topology. *Phys. Rep.* **254**, 135 (1995).
45. J. Levin, E. Scannapieco, and J. Silk. The topology of the universe: the biggest manifold of them all. *Class. Quantum Gravity* **15**, 2689 (1998).
46. H. Hopf. Über die Abbildungen der dreidimensionalen Sphäre auf die Kugelfläche. *Math. Ann.* **104**, 637 (1931).
47. T. Lachner, D. de las Heras, and T. M. Fischer. Braiding with magnetic octupoles. *Phys. Rev. Res.* **3**, 013043 (2021).
48. M. Mirzaee-Kakhki, A. Ernst, D. de las Heras, M. Urbaniak, F. Stobiecki, A. Tomita, R. Huhnstock, I. Koch, A. Ehresmann, D. Holzinger, and T. M. Fischer. Gauge invariant and gauge dependent aspects of topological walking colloidal bipeds. *Soft Matter* **17**, 1663 (2021).
49. M. Mirzaee-Kakhki, A. Ernst, D. de las Heras, M. Urbaniak, F. Stobiecki, J. Gördes, M. Reginka, A. Ehresmann, and T. M. Fischer. Simultaneous polydirectional transport of colloidal bipeds. *Nat. Commun.* **11**, 4670 (2020).

50. M. Mirzaee-Kakhki, A. Ernst, D. de las Heras, M. Urbaniak, F. Stobiecki, A. Tomita, R. Huhnstock, I. Koch, J. Gördes, A. Ehresmann, D. Holzinger, M. Reginka, and T. M. Fischer. Colloidal trains. *Soft Matter* **16**, 1594 (2020).
51. H. Massana-Cid, A. Ernst, D. de las Heras, A. Jarosz, M. Urbaniak, F. Stobiecki, A. Tomita, R. Huhnstock, I. Koch, A. Ehresmann, D. Holzinger, and T. M. Fischer. Edge transport at the boundary between topologically equivalent lattices. *Soft Matter* **15**, 1539 (2019).
52. A. M. E. B. Rossi, J. Bugase, T. Lachner, A. Ernst, D. de las Heras, and T. M. Fischer. Hard topological versus soft geometrical magnetic particle transport. *Soft Matter* **15**, 8543 (2019).
53. J. Loehr, D. de las Heras, A. Jarosz, M. Urbaniak, F. Stobiecki, A. Tomita, R. Huhnstock, I. Koch, A. Ehresmann, D. Holzinger, and T. M. Fischer. Colloidal topological insulators. *Commun. Phys.* **1** (2018).
54. J. Loehr, D. de las Heras, M. Loenne, J. Bugase, A. Jarosz, M. Urbaniak, F. Stobiecki, A. Tomita, R. Huhnstock, I. Koch, A. Ehresmann, D. Holzinger, and T. M. Fischer. Lattice symmetries and the topologically protected transport of colloidal particles. *Soft Matter* **13**, 5044 (2017).
55. J. Loehr, M. Loenne, A. Ernst, D. de las Heras, and T. M. Fischer. Topological protection of multiparticle dissipative transport. *Nat. Commun.* **7**, 11745 (2016).
56. D. de las Heras, J. Loehr, M. Loenne, and T. M. Fischer. Topologically protected colloidal transport above a square magnetic lattice. *New. J. Phys.* **18**, 105009 (2016).
57. J. Gomm, P. Browne, R. Coope, Q. Liu, L. Buluwela, and R. Coombes. Isolation of Pure Populations of Epithelial and Myoepithelial Cells from the Normal Human Mammary Gland Using Immunomagnetic Separation with Dynabeads. *Anal. Biochem.* **226**, 91 (1995).
58. S. L. Thein and J. Hinton. A simple and rapid method of direct sequencing using Dynabeads. *Br. J. Haematol.* **79**, 113 (1991).
59. C. J. Jackson, P. K. Garbett, B. Nissen, and L. Schrieber. Binding of human endothelium to Ulex europaeus l-coated Dynabeads: application to the isolation of microvascular endothelium. *J. Cell Sci.* **96**, 257 (1990).
60. J. L. Aragonés, J. P. Steimel, and A. Alexander-Katz. Elasticity-induced force reversal between active spinning particles in dense passive media. *Nat. Commun.* **7**, 11325 (2016).

61. J. L. Aragones, J. P. Steimel, and A. Alexander-Katz. Aggregation dynamics of active rotating particles in dense passive media. *Soft Matter* **15**, 3929 (2019).
62. J. P. Steimel, J. L. Aragones, H. Hu, N. Qureshi, and A. Alexander-Katz. Emergent ultra-long-range interactions between active particles in hybrid active-inactive systems. *Proc. Natl. Acad. Sci.* **113**, 4652 (2016).
63. *CC BY 3.0* <https://creativecommons.org/licenses/by/3.0/>. last retrieved 24.07.2023.
64. B. D. Sharma. Crystallographic and Spectroscopic Symmetry Notations. *J. Chem. Educ.* **59**, 554 (1982).
65. *CC BY 4.0* <https://creativecommons.org/licenses/by/4.0/>. last retrieved 24.07.2023.
66. A. K. Geim and K. S. Novoselov. The rise of graphene. *Nat. Mater.* **6**, 183 (2007).
67. K. S. Novoselov, A. K. Geim, S. V. Morozov, D. Jiang, Y. Zhang, S. V. Dubonos, I. V. Grigorieva, and A. A. Firsov. Electric Field Effect in Atomically Thin Carbon Films. *Science* **306**, 666 (2004).
68. E. Y. Andrei and A. H. MacDonald. Graphene bilayers with a twist. *Nat. Mater.* **19**, 1265 (2020).
69. S. Lisi *et al.* Observation of flat bands in twisted bilayer graphene. *Nat. Phys.* **17**, 189 (2020).
70. G. Tarnopolsky, A. J. Kruchkov, and A. Vishwanath. Origin of Magic Angles in Twisted Bilayer Graphene. *Phys. Rev. Lett.* **122**, 106405 (2019).
71. M. Yankowitz, S. Chen, H. Polshyn, Y. Zhang, K. Watanabe, T. Taniguchi, D. Graf, A. F. Young, and C. R. Dean. Tuning superconductivity in twisted bilayer graphene. *Science* **363**, 1059 (2019).
72. H. Polshyn, M. Yankowitz, S. Chen, Y. Zhang, K. Watanabe, T. Taniguchi, C. R. Dean, and A. F. Young. Large linear-in-temperature resistivity in twisted bilayer graphene. *Nat. Phys.* **15**, 1011 (2019).
73. Y. Cao, V. Fatemi, S. Fang, K. Watanabe, T. Taniguchi, E. Kaxiras, and P. Jarillo-Herrero. Unconventional superconductivity in magic-angle graphene superlattices. *Nature* **556**, 43 (2018).
74. P. Moon and M. Koshino. Optical absorption in twisted bilayer graphene. *Phys. Rev. B* **87**, 205404 (2013).

75. A. I. Cocemasov, D. L. Nika, and A. A. Balandin. Phonons in twisted bilayer graphene. *Phys. Rev. B* **88**, 035428 (2013).
76. A. K. Geim. Graphene: Status and Prospects. *Science* **324**, 1530 (2009).
77. S. M. Gardezi, H. Pirie, S. Carr, W. Dorrell, and J. E. Hoffman. Simulating twistrionics in acoustic metamaterials. *2D Mater.* **8**, 031002 (2021).
78. W. Li, C. J. O. Reichhardt, B. Jankó, and C. Reichhardt. Vortex dynamics, pinning, and angle-dependent motion on moiré patterns. *Phys. Rev. B* **104**, 024504 (2021).
79. J. R. Moffitt, Y. R. Chemla, S. B. Smith, and C. Bustamante. Recent Advances in Optical Tweezers. *Annu. Rev. Biochem.* **77**, 205 (2008).
80. A. M. Lacasta, J. M. Sancho, A. H. Romero, and K. Lindenberg. Sorting on Periodic Surfaces. *Phys. Rev. Lett.* **94**, 160601 (2005).
81. M. P. MacDonald, G. C. Spalding, and K. Dholakia. Microfluidic sorting in an optical lattice. *Nature* **426**, 421 (2003).
82. M. Bartelmann. Gravitational lensing. *Class. Quantum Gravity* **27**, 233001 (2010).
83. S. Chatrchyan *et al.* Observation of a new boson at a mass of 125 GeV with the CMS experiment at the LHC. *Phys. Lett. B* **716**, 30 (2012).
84. M. Fridman, A. Farsi, Y. Okawachi, and A. L. Gaeta. Demonstration of temporal cloaking. *Nature* **481**, 62 (2012).
85. P. Alitalo and S. Tretyakov. Electromagnetic cloaking with metamaterials. *Mater. Today* **12**, 22 (2009).
86. S. A. Cummer and D. Schurig. One path to acoustic cloaking. *New J. Phys.* **9**, 45 (2007).
87. F. Sammüller and M. Schmidt. Adaptive Brownian Dynamics. *J. Chem. Phys.* **155**, 134107 (2021).
88. N. C. X. Stuhlmüller. *Drawing with Colloids v1.0.0* Zenodo. <https://doi.org/10.5281/zenodo.8413928>. 2023.
89. A. P. Antonov, A. Ryabov, and P. Maass. Solitons in Overdamped Brownian Dynamics. *Phys. Rev. Lett.* **129**, 080601 (2022).
90. M. Schmidt. Power functional theory for many-body dynamics. *Rev. Mod. Phys.* **94**, 015007 (2022).
91. N. C. X. Stuhlmüller, T. Eckert, D. de las Heras, and M. Schmidt. Structural Nonequilibrium Forces in Driven Colloidal Systems. *Phys. Rev. Lett.* **121**, 098002 (2018).

92. D. de las Heras, T. Zimmermann, F. Sammüller, S. Hermann, and M. Schmidt. Perspective: How to overcome dynamical density functional theory. *J. Phys.: Condens. Matter* **35**, 271501 (2023).
93. J. L. Bentley. Multidimensional binary search trees used for associative searching. *Commun. ACM* **18**, 509 (1975).
94. W. H. Press, S. A. Teukolsky, W. T. Vetterling, and B. P. Flannery. *Numerical Recipes 3rd Edition. The Art of Scientific Computing* (Cambridge University Press, 2007).

Eidesstattliche Versicherung

Hiermit versichere ich an Eides statt, dass ich die vorliegende Arbeit selbstständig verfasst und keine anderen als die von mir angegebenen Quellen und Hilfsmittel verwendet habe.

Weiterhin erkläre ich, dass ich die Hilfe von gewerblichen Promotionsberatern bzw. -vermittlern oder ähnlichen Dienstleistern weder bisher in Anspruch genommen habe, noch künftig in Anspruch nehmen werde.

Zusätzlich erkläre ich hiermit, dass ich keinerlei frühere Promotionsversuche unternommen habe.

Bayreuth, den 26. Oktober 2023

Nico Christian Xaver Stuhlmüller